CONTROLLING MORPHOLOGY OF CONJUGATED POLYMERS AND THE IMPACT ON CHARGE TRANSPORT IN FLEXIBLE ORGANIC FIELD-EFFECT TRANSISTORS

A Dissertation
Presented to
The Academic Faculty

by

Ping-Hsun Chu

In Partial Fulfillment
of the Requirements for the Degree
Doctor of Philosophy in the
School of Chemical and Biomolecular Engineering

Georgia Institute of Technology
May 2017

CONTROLLING MORPHOLOGY OF CONJUGATED POLYMERS AND THE IMPACT ON CHARGE TRANSPORT IN FLEXIBLE ORGANIC FIELD-EFFECT TRANSISTORS

Approved by:

Dr. Elsa Reichmanis, Advisor
School of Chemical and Biomolecular Engineering
Georgia Institute of Technology

Dr. J. Carson Meredith
School of Chemical and Biomolecular Engineering
Georgia Institute of Technology

Dr. Mohan Srinivasarao, Advisor
School of Materials Science and Engineering
Georgia Institute of Technology

Dr. Sven Holger Behrens
School of Chemical and Biomolecular Engineering
Georgia Institute of Technology

Dr. William J. Koros
School of Chemical and Biomolecular Engineering
Georgia Institute of Technology

Date Approved: March 09, 2017

This thesis is dedicated to my parents, grandparents, sister and girlfriend.

ACKNOWLEDGEMENTS

First and foremost, I would like to express my sincerest gratitude to my advisor, Prof. Elsa Reichmanis, for her continuous support, guidance and encouragement during my entire Ph.D. study and research. My sincere thanks also goes to my co-advisor, Prof, Mohan Srinivasarao, for his valuable advice, understanding and patience. Besides my advisor, I would like to thank the rest of my thesis committee, Prof. William Koros, Prof. Carson Meredith and Prof. Sven Behrens, for their kindness and insightful comments.

I would also like to thank my labmates, coworkers and friends, Dr. Boyi Fu, Dr. Nabil Kleinhenz, Dr. Mincheol Chang, Dr. Dalsu Choi, Dr. Gang Wang, Michael McBride, Nils Persson, Bailey Risteen, Dr. Guoyan Zhang, Ji-Hwan Kang, Zhibo Yuan, Jeff Hernandez, Rui Chang, Yo Han Kwon, Krysten Minnici, Brian Khau, Giovanni DeLuca and many others who have always been willing to help, advise and share enlightening ideas with me. I am proud to be associated with such innovative and dynamic people and feel very fortunate to be part of Reichmanis group. Additionally, my special gratitude goes to all of my friends in Georgia Tech, for the friendship and assistance in overcoming numerous obstacles I have been facing over the past few years.

Last but not the least, I would like to express my profound gratitude to my parents, grandparents, sister, girlfriend and all of my friends in Taiwan, for providing me everlasting support, continuous encouragement and endless love throughout my life.

TABLE OF CONTENTS

LIST OF FIGURES

SUMMARY

The discovery of organic semiconductors has opened new possibilities for the development of large-scale, lightweight and flexible electronic devices that can be fabricated under ambient conditions at low cost. Organic semiconductors have been targeted as active materials for transistors, photovoltaics, displays, sensors, light-emitting diodes and health monitoring devices owing to their chemical tunability and functionality for specific applications. Although significant progress has been achieved, organic semiconductors typically exhibit low charge carrier mobilities, poor environmental stability and short operational lifetime when compared to their inorganic counterparts. Thus, the flexible, stretchable and wearable organic electronic devices still persist at an early stage of development, and many key challenges remain to be addressed. Herein, this thesis focuses on fundamental investigations of the correlations between morphology and charge transport properties into every aspect of a model conjugated polymer, poly(3-hexylthiophene) (P3HT), from intra/inter-molecular interactions to micro/macro-scale thin film structure in order to explore the potential of this conjugated polymer for field-effect transistor applications, continuous roll-to-roll printing device production and flexible device fabrication.

First, an improved organic field-effect transistor is demonstrated through a polymer-oligomer semiconductor blend approach. The incorporation of an air-stable oligomer into oxygen sensitive P3HT effectively reduced the oxidative doping effect even when the device fabrication was carried out under ambient conditions, resulting in a substantial decrease in threshold voltage and off-current. Additionally, the charges

trapped in grain boundaries were minimized since the isolated oligomer crystalline domains were interconnected by long polymer chains. This facile blend approach provides an alternative avenue to combine the advantageous properties of conjugated polymers and oligomers for OFET fabrication, which required no pre- and/or post treatments.

In addition to controlling the morphology of the semicrystalline polymer-oligomer thin film structure, the impact of P3HT crystal orientation on charge transport was systematically investigated. Long-range ordering and highly aligned P3HT thin films can be obtained by preprocessing the polymer solution with ultraviolet irradiation/solution aging and then depositing via the blade coating method, which is compatible with roll-to-roll printing processes. The surface morphologies and optical anisotropy of deposited films revealed that the degree of chain alignment was greatly improved with increased levels of polymer assembly that can be precisely controlled by solution-aging time. This highly anisotropic crystalline thin film structure provides a useful platform to explore the intra- and intermolecular charge transport properties of P3HT in OFETs.

Finally, we take a further step to develop a fully-flexible OFET device on a plastic substrate by using ultraviolet irradiated regioregular and regiorandom P3HT blend thin films as the device active layer. The transistors not only provide prominent charge carrier mobility but also exhibit impressive mechanical flexibility upon application of high external bending strain. Hence, the insights gained here are expected to facilitate the identification of processing parameters and materials design that will help future breakthroughs in organic electronic device performance.

CHAPTER 1. INTRODUCTION

1.1 Organic Semiconductors

1.1.1 History and Background

Since the invention of the first transistor by John Bardeen, Walter Brattain and William Shockley in 1947 at Bell Laboratories (Figure 1.1a),[1] semiconductor devices have become ubiquitous, supporting almost every aspect of human daily life, from consumer electronics to advanced scientific research. To reduce the production costs and meet the growing demand for semiconductor electronics, many efforts have been made to improve device performance and increase the number of transistors in each single integrated circuit. Recently, a new category of devices, macroelectronics, has generated much interest with the aim of large-scale and continuous production rather than reducing the feature size or increasing the device density on processor chips.[2, 3] The most successful application of macroelectronics is flat-panel displays, which appear far lighter, thinner and more economical than traditional cathode-ray tubes, and have thus rapidly dominated the desktop-monitor and digital television market.[4] The other visible examples include radio-frequency identification tags (RFIDs), solar cells and thin film transistors, which can be fabricated by low-cost and high throughput printing techniques (Figure 1.1b).

Over the past few decades, the electronics industry has been dominated by inorganic semiconductors, especially silicon, until the discovery of the conductive polymer, polyacetylene, which when doped with iodine, can lead to a 10^{10} times increase

in room-temperature conductivity compared with the original insulating polyacetylene.[5] The breakthrough of organic semiconductors (OSCs) was realized in 1977 by Alan J. Heeger, Hideki Shirakawa and Alan G. MacDiarmid, who were awarded the Nobel Prize in chemistry in 2000. This was quickly followed by the development of the organic field-effect transistor (OFET) by using semiconducting polymer, polythiophene, as the active layer in 1986.[6] Subsequently, OSCs have become a promising candidate for macroelectronics fabrication.

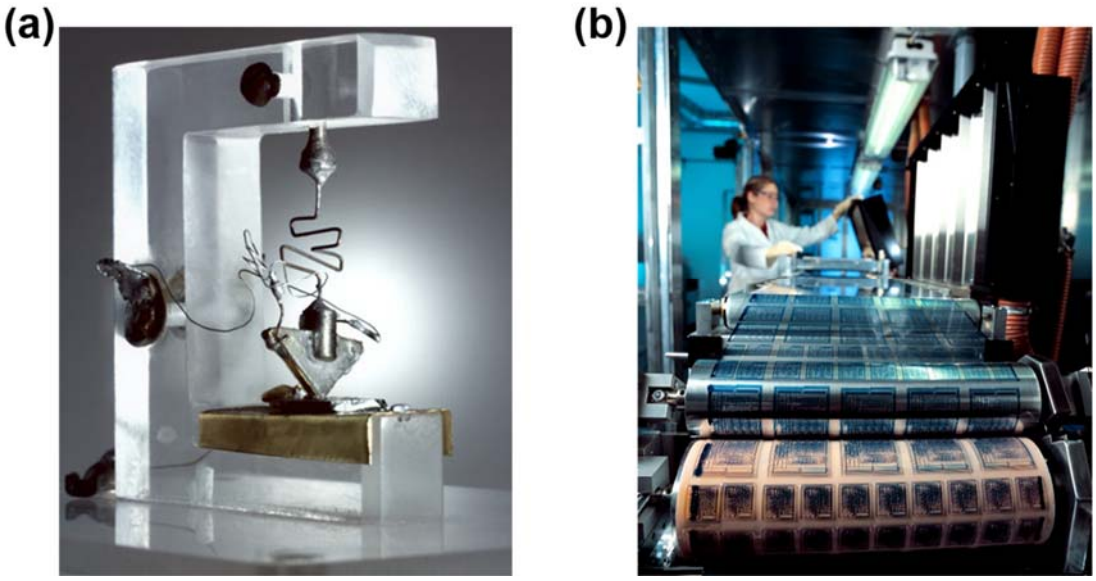

Figure 1.1 (a) The world's first transistors,[7] (b) Roll-to-roll printed electronics.[8]

In contrast to the transistors based on inorganic semiconducting materials, which generally need to be fabricated under high vacuum processing conditions where the size of the sample is typically limited by the space available in the reaction chamber, OSCs can be deposited on various of substrates such as glass, plastic and paper, in large-scale, simply by solution processing under ambient and relatively low temperature conditions. The chemical functionality of organic materials such as solubility, mechanical flexibility,

molecular weight, degree of crosslinking and thermal stability can be further tuned by molecular design and synthesis strategies to suit different applications. Moreover, a wide range of fabrication methods, including spin coating, blade coating, ink-jet printing, roll-to-roll processing, and so forth are available, allowing for the production of low-cost, lightweight and flexible macroelectronics.

The development of OSCs has brought a large number of applications across the market. In 1997, the first organic light emitting diode (OLEDs) displays for car radios fabricated with OSCs as the active materials became available for commercial use,[9] and later this introduction was followed by the expansion of OLED technology from mobile phones to HDTV and even next-generation rollable displays as shown in Figure 1.2a-b.[10] The advanced applications of OSCs can also be found in organic photovoltaics (OPV), RFID tags and OFETs. Recently, OSCs have attracted considerable attention for the development of electronic-skin (e-skin) owing to their stretchability,[11, 12] biocompatibility[13] and biodegradability.[14, 15] These bio-inspired e-skins, which exhibit highly thermal and tactile sensing properties have provided many additional applications including wearable devices, health monitoring and smart robots (Figure 1.2c-d).[16-19]

Although significant and substantial progress has been made, further advances are still necessary in order to improve device performance, device-to-device uniformity and environmental stability. The transistors based on solution processed OSCs show charge carrier mobilities in a range of $10^{-2} - 1$ $cm^2 V^{-1} s^{-1}$ (though some rare cases demonstrate that the device mobility can be increased over 30 $cm^2 V^{-1} s^{-1}$ with particular treatments),[20, 21] which is generally still relatively lower than the mobilities obtained from inorganic semiconductors such as polycrystalline silicon,[22, 23] MoS_2,[24] and metal oxide[25-28] (exhibit

the mobilities in a range of 1 − 100 $cm^2V^{-1}s^{-1}$). This is mainly attributed to their poor thin film crystallinity,[29, 30] unfavorable crystal orientation[31, 32] and large number of grain boundaries[33, 34] that limit efficient charge transport in OSC films. The sensitivity of molecular packing structure to the fabrication parameters, such as solvent evaporation rate,[35-37] solubility[38-40] and substrate temperature[41-44] can also lead to a decrease in thin film uniformity when OSCs are deposited over large-area substrates. The other major issue related to poor environmental stability may further restrict the development and application of OSCs in the semiconductor industry.[45-48]

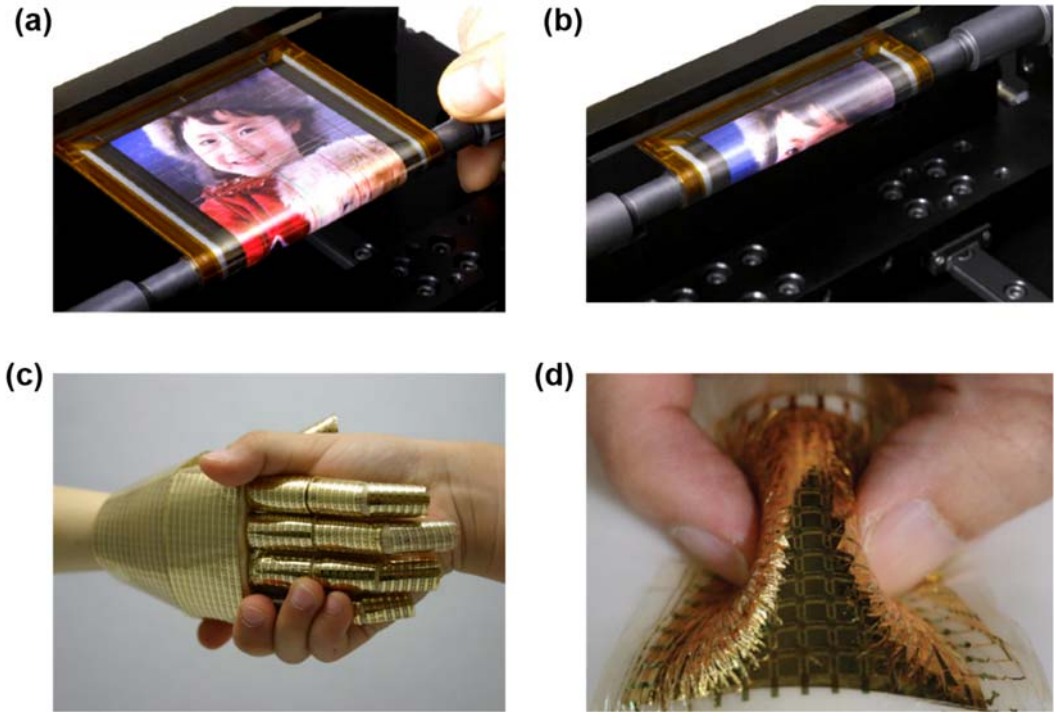

Figure 1.2 Rollable OTFT-driven OLED display[10] in (a) flat condition and (b) rolled-up condition. (c) Electronic artificial skin[49] and (d) pressure sensor integration with an organic transistor driven active matrix.[50]

1.1.2 Small Molecule and Polymer Semiconductors

Semiconductors are those materials whose electrical conductivity lies between conductors and insulators. The relatively small energy band gap of semiconducting materials allows some electrons to shift from the valance band to the conduction band by gaining a certain amount of thermal energy at room temperature. An increase in temperature improves the conductivity of semiconductors since more electrons can reach the conduction band. In contrast to inorganic semiconducting materials such as silicon, germanium, arsenide or III-V compounds, OSCs are mainly made up of carbon and hydrogen atoms. Generally, these OSCs can be further divided into two main categories: small molecule and polymer semiconductors. (Figure 1.3)

Small molecule semiconductors such as pentacene[51, 52] and rubrene[53] with charge carrier mobilities over 1 $cm^2\ V^{-1}\ s^{-1}$ have been achieved. This charge transport performance is comparable to, or even surpasses amorphous silicon based transistors.[54] The electrical properties of small molecule semiconductors keep improving through a better understanding of the molecular structure implications, materials processing, chemical design and device optimization. For example, Takimiya et al. successfully synthesized the air-stable OSC materials 2,7-diphenyl[1]benzothieno[3,2-b][1]benzothiophene (DPh-BTBT)[55] and dinaphtho[2,3-b:20,30-f]thieno[3,2-b]thiophene (DNTT),[56] which show impressive charge carrier mobilities of ~2.0 and ~3.0 $cm^2\ V^{-1}\ s^{-1}$, respectively. The molecular structures of DPh-BTBT and DNTT are shown in Figure 1.3. Although these small molecule semiconductors exhibit superior charge transport properties, their insolubility in most organic solvents and requirement for high vacuum deposition techniques still make them impractical for commercial production. Anthony et

al.[57] recently reported that the introduction of functional groups into the molecular structure has a positive impact on solution processability, molecular packing structure, thin film morphology and thereby device performance. For example, 6,13-bis(triisopropylsilylethynyl)pentacene (TIPS-Pentacene) exhibits an improved solubility, greater π-orbital overlap and reduced interplanar spacing than unsubstituted pentacene.[58] Similar work, reported by Takeya et al.[59] suggested that the introduction of alkyl substituents into DNTT small molecules allows these materials to be processed with solution printing techniques, and the average mobility of these transistors reaches approximately 7 $cm^2 V^{-1} s^{-1}$.

In contrast to small molecules, which exhibit molecular weight (MW) less than 1 kD, the MW of polymer semiconductors is typically greater than 3 kD. Because of their solubilizing alkyl side chain, polymer semiconductors are readily dissolved in a wide range of organic solvents. The high polymeric solution viscosity ensures excellent thin film uniformity and reproducibility after the solution coating process. Moreover, the mechanical properties of polymer semiconductors can be fine-tuned via molecular design, such as MW, regioregularity,[60] presence of fused or isolated rings in the main chains[61] and the chemical structure of the pendant group.[62] For instance, Lipomi and co-workers[62] demonstrated that the tensile modulus of regioregular poly(3-alkylthiphenes) (P3ATs) can be significantly reduced with increasing length of the alkyl side-chain, leading to improved mechanical compliance. Dauskardt et al.[63] further reported that increased MW of P3ATs can lead to greater mechanical internal cohesion and thus increased the thin film plasticity, which helps dissipate the applied strain energy. These results suggest that polymer semiconductors are promising materials for flexible and

stretchable electronic applications in comparison to inorganic and organic small molecule semiconductors.

However, polymer semiconductors still face several challenges associated with (1) chain entanglement, chain folding and broad polydispersity which lead to a decrease in crystallinity and charge carrier mobility; (2) randomly oriented crystalline domains, which is not beneficial for unidirectional charge transport in transistors; (3) weak oxidative stability and rapid deterioration when unencapsulated devices are operated under ambient condition; (4) generation of low short-circuit currents within OPVs because of a relatively large bandgap that restricts sunlight absorption. To deal with these issues, further efforts, including chemical synthesis, development of processing strategies and device structure design are needed for the establishment of vital knowledge with respect to how molecular structure and processing approaches impact the inter/intramolecular interactions, surface morphology and thin film crystallinity, and how these ultimately affect OFET charge transport performance, device stability and mechanical flexibility.

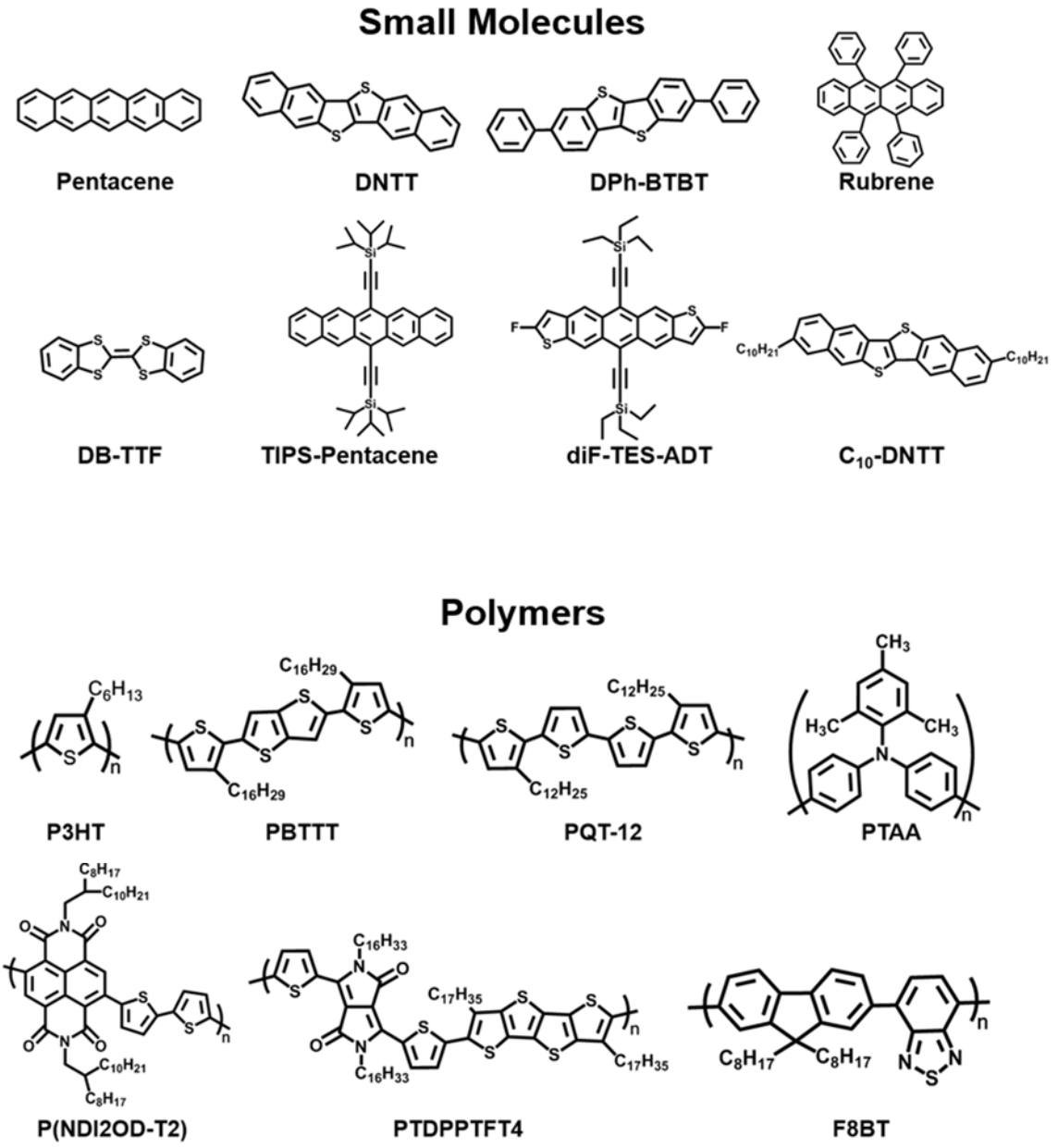

Figure 1.3 Molecular Structure of small molecule and polymer semiconductors.

1.2 Charge Transport in Organic Semiconductors

1.2.1 Conjugated System

Organic polymers have been considered for a long time as insulators due to their saturated chemical structure. Polyethylene (PE), one of the most common polymers, is comprised of a long chain of monomeric repeat units $–(CH_2–CH_2)_n–$. As shown in Figure 1.4a,[64] each carbon atom is sp^3 hybridized and binds to the other four adjacent atoms by sigma (σ) bonds, resulting in an excellent insulating property. However, the traditional idea that organic polymers are insulators was shattered since the accidental discovery of high electrical conductivity in oxidized iodine-doped polyacetylene in 1977.[65]

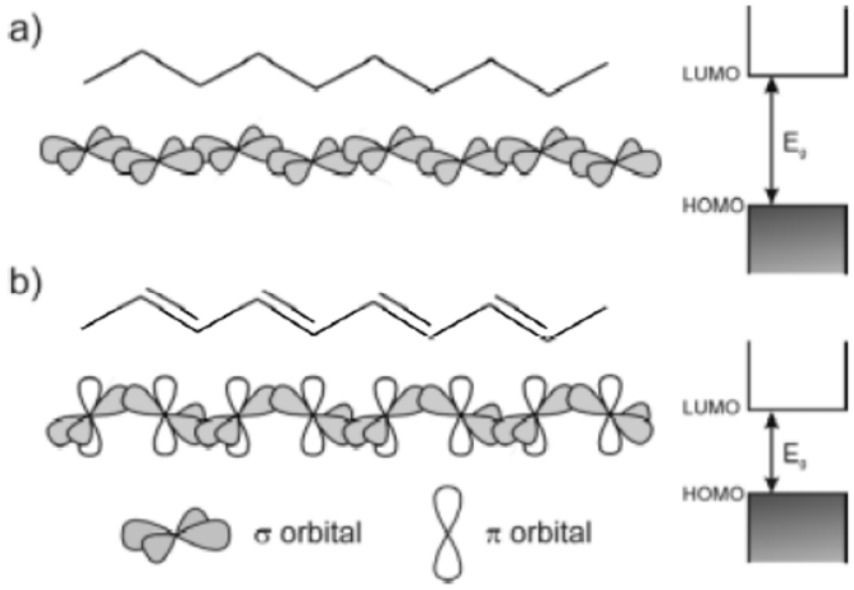

Figure 1.4 The chemical structure (left) and energy diagram (right) of (a) polyethylene, (b) polyacetylene.[64]

This different class of polymer consists of a unique polymer backbone with alternating single and double bonds called a π-conjugated polymer, which covers the

whole insulator-semiconductor-metal region of electrical properties. The hybrid orbitals between adjacent carbon atoms lead to the formation of strong localized σ bonds, which are responsible for the mechanical properties. The overlap of remaining p_z orbitals between successive carbon atoms allows the unpaired electrons to be delocalized along the polymer backbone, affording the charge carrier mobility. (Figure 1.4b[64]) Accordingly, the electrical and optical properties of conjugated polymers are determined by the number of atoms and the degree of effective conjugation.

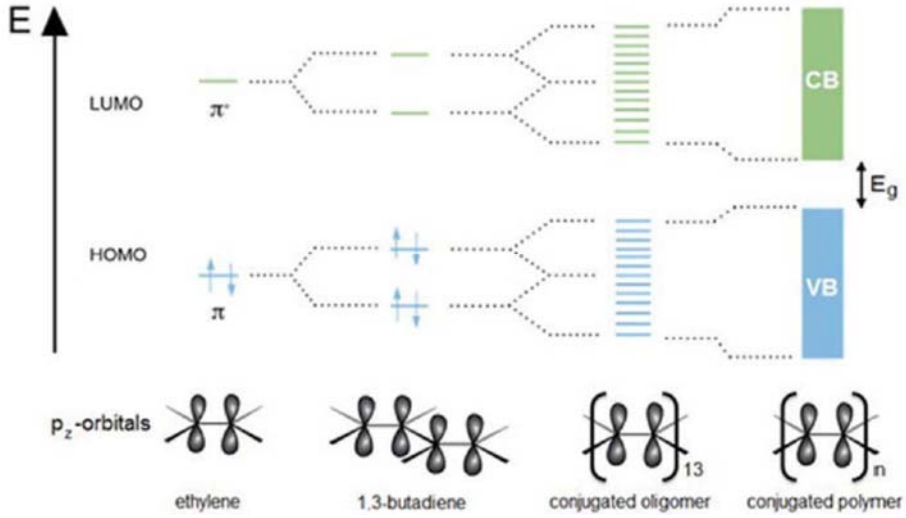

Figure 1.5 The formation of π and π* energy bands with increased number of monomeric repeat unit.[66]

As shown in Figure 1.5, the number of discrete energy levels is proportional to the number of monomeric repeat units. In the case of long conjugated polymer chains, the innumerable discrete energy levels become very closely spaced, and thus they can be regarded as continuous energy bands. The filled π-band and empty π*-band are referred to as the valence and conduction band, respectively. In addition, the top of the valence band is called the highest occupied molecular orbital (HOMO); and the bottom of the

conduction band is called the lowest unoccupied molecular orbital (LUMO). The energy difference between the LUMO and HOMO defines the energy band gap (E_g). As the number of carbon atoms and conjugation is increased, the additional splitting of the π and π* levels, which elevate the HOMO and lower the LUMO energy level give rise to a further reduced energy band gap, which is in the range of 1 to 4 eV, and thus rendering conjugated polymers with semiconducting properties.

1.2.2 Charge Transport Models

The conjugated materials have been widely explored as active layers for multiple electronic applications owing to their unique semiconducting properties. Before getting into the details of these devices, it is crucial to understand the fundamental theory of charge transport in OSCs. In inorganic semiconductors such as silicon or germanium, the three dimensional covalently bonded lattices lead to well-established valance and conduction bands, which allow charge carriers to be delocalized over the entire molecule or system, so called band transport. To achieve this coherent transport regime, a strong coupling between constituent atoms and highly crystalline structure is required. Typically, the charge transport in this band regime is highly temperature dependent since increased temperature causes enhanced molecular vibration, which can act as scattering centers for the charge carriers, resulting in a decrease in mobility. However, the band model is unable to well describe the charge transport behavior in OSCs due to their relatively weak electronic coupling between adjacent molecules and the polarization effect.[67]

Figure 1.6. shows an example of polarization in an organic solid. The hexagons represent the fixed benzene rings, while the circles indicate the delocalized π-electrons. The appearance of positive charge on the central molecule in a conjugated material tends to polarize its neighboring region, and the magnitude of polarization becomes stronger when the molecule is closer to the center. As a result, the positive charge in conjugated organic solids is addressed by the polarization cloud, and the species formed are called polarons; this is very different from the conventional free charges found in crystalline inorganic semiconductors. The stability of the polaron in an organic solid can be determined by (1) the average residence time of charge on a molecule, τ_{res}; and (2) the required time to form the electronic polarization cloud around the charge, τ_{el}. The magnitude of both characteristic times can be further estimated by the following Equation 1.1.[68]

$$\tau \lessapprox \frac{\hbar}{\Delta E} \tag{1.1}$$

where ħ is the Planck's constant divided by 2π and ΔE is a characteristic energy.

For the charge carrier residence time, the pertinent energy is the bandwidth, which is associated with the electronic coupling between adjacent molecules. In general, OSCs exhibit a relatively small bandwidth (~0.1 eV) in comparison to their inorganic counterparts, which show a value of 10 eV, and these bandwidths give rise to a distinct residence time of 10^{-14} s for the former and 10^{-16} s for the latter. As for the polarization time, the energy is directly related to the energy gap (~1 eV), therefore the time is 10^{-15} s for both materials. In short, the characteristic time follows the sequence of $\tau_{res,\ inorganic} < \tau_{el} < \tau_{res,\ organic}$.[67] For inorganic semiconductors, the charge carriers move too fast that

polarization could does not have enough time to form, resulting in band-like transport. On the other hand, the electronic polaron has sufficient time to form within organic materials since the residence time of charge carriers on the molecule is 10 times longer than the time it takes to form a polarization cloud around the charges. As a result, the motion of the charge carriers in OSCs takes place by hopping between localized states, so called hopping transport.

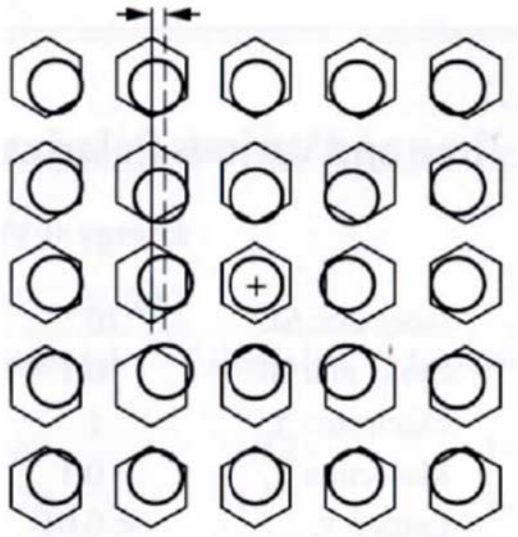

Figure 1.6 The formation of polaron when a positive charge is placed on a conjugated molecule.[67]

According to Marcus's electron transfer theory,[69] the hopping process is the electron transfer from an electron donor to an electron acceptor. Figure 1.7 illustrates that when a charge hops from an ionized molecule to a neutral molecule, the formerly ionized molecule relaxes back to the neutral state. Meanwhile, the latter molecule turns into an ionized state by gaining an electron. This self-exchange electron transfer reaction, without making or breaking bonds, involves geometry relaxations when the molecule moves from the neutral state to the ionized state and vice versa. The total reorganization energy is the sum of these two relaxations.

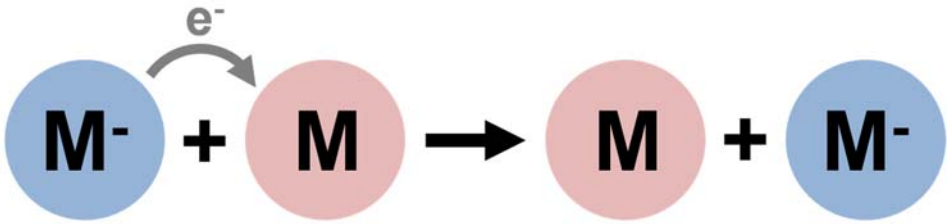

Figure 1.7 The self-exchange electron-transfer reaction between two molecules.

The electron hopping rate (k_{ET}) from site *i* to *j* across the distance R_{ij} can be predicted by the following Equation 1.2.[70]

$$k_{ET} = \frac{2\pi}{\hbar}\frac{t^2}{\sqrt{4\pi\lambda_{reorg}k_BT}}\exp\left[-\frac{\left(\lambda_{reorg}+\Delta E\right)^2}{4\lambda_{reorg}k_BT}\right] \quad (1.2)$$

where t the transfer integral, ħ is the Planck's constant divided by 2π, k_B is Boltzmann's constant, T is temperature, ΔE is the energy difference of two chosen sites (*i*, *j*) and λ_{reorg} is the reorganization energy. The higher the electron hopping rate, the faster will be the charge carrier transport in OSCs, and higher corresponding mobility. It is evident in equation 1.2, the electron hopping rate can be enhanced by maximizing the transfer integral and minimizing the reorganization energy. As shown in Figure 1.8, the magnitude of the transfer integral, which strongly depends on the strength of interaction, or rather electronic coupling between two adjacent molecules, are observed to enhance exponentially with reduced intermolecular distance in the case of perfectly cofacial tetracene dimer. This result indicates that the improvement of molecular π-π stacking, which corresponds to the increase in wavefunction overlap between the molecules, has a positive impact on charge carrier mobility in OSCs.[68] The further details associated with

the relationship between molecular packing structure and charge transport performance will be elaborated in the following sections.

As for the reorganization energy, the value decreases with the increase in π-conjugation since the effective charge carriers delocalization is able to reduce the structural deformation during charge transport.[71, 72] For example, the reorganization energies of oligoacene and thienoacene families monotonically decrease with a larger number of aromatic conjugated rings as shown in Figure 1.9.[73] Accordingly, for a set of similar compounds, more extended π-conjugation is more favorable for charge hopping, and hence better charge transport properties.

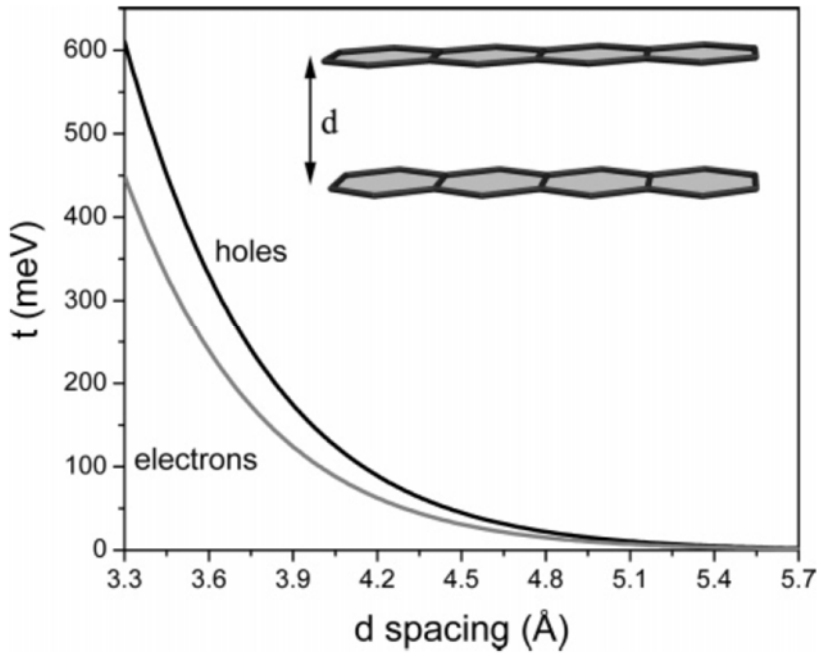

Figure 1.8 Transfer integrals (*t*) for electrons and hole transfer in perfectly cofacial tetracene dimer as a function of intermolecular distance.[68]

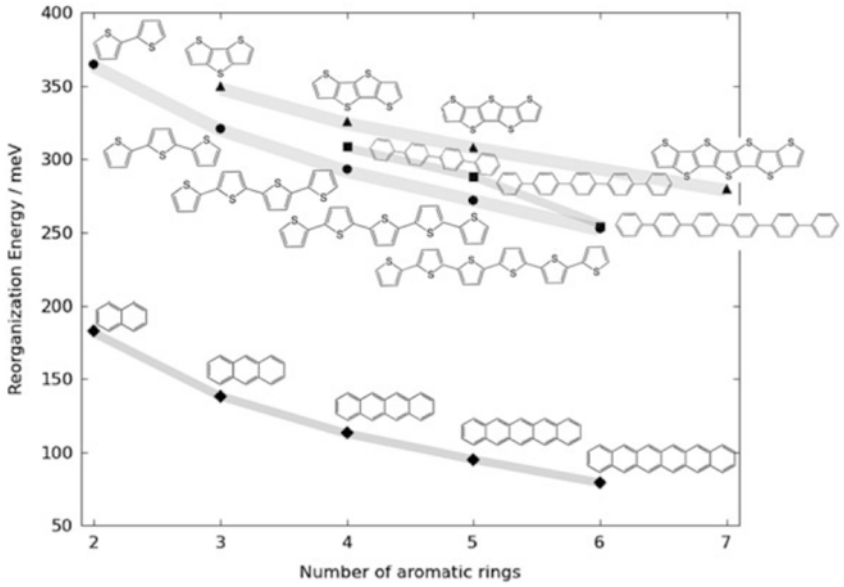

Figure 1.9 The reorganization energies of oligoacene and thienoacene families as a function of the number of aromatic rings.[73]

1.2.3 The Impact of Molecular Packing Structure on Charge Transport

The charge motions in OSCs are primarily governed by hopping transport, which is directly related to the intramolecular interactions of neighboring molecules and how these molecules pack with each other. Hence, determining the relationship between charge transport and molecular packing structure is crucial for increasing the charge carrier mobility. From the viewpoint of the molecular level, the charge carriers exhibit highly anisotropic charge transport properties in conjugated materials. As shown in Figure 1.10, intramolecular charge transport is fastest in the direction of π-conjugation since the charge carrier delocalization is mainly attributed to the electronic coupling of unhybridized p_z carbon orbitals along the backbone.[2] When multiple molecules are further closely stacked, the supramolecular ordering structure not only assists the intrachain charge transfer owing to the overlap of π-orbitals but also allows the

macroscopic intermolecular charge transport over the long-range π-π stacking direction. However, it is almost insulating along the direction of alkyl side-chain.

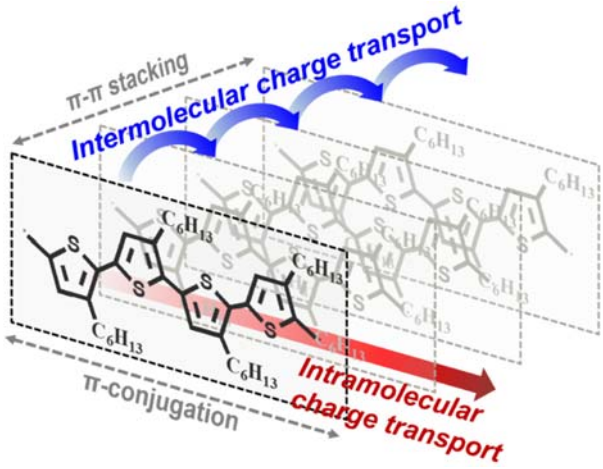

Figure 1.10 Inter- and intramolecular charge transport in crystalline polythiophene.

The orientation of the molecular packing structure also shows significant impact on the anisotropic charge transport and corresponding electronic device performance. In the case of P3HT, Sirringhaus and coworkers[74] revealed that the P3HT packing direction can adopt either a parallel or perpendicular orientation with respect to the substrate as shown in Figure 1.11. The (100) crystal planes preferentially oriented normal to the film and the (010) axis parallel to the film, referred to as "edge-on", is beneficial for in-plane charge transport in the OFETs. In contrast, the out-of-plane charge transport between the top and bottom electrodes is more efficient in OPVs, and thus the crystallites with (100) axis parallel to the film and (010) axis normal to the film, referred to as "face-on" is more desired. Recently, the "chain-on" orientation, which exhibits a long-range alignment of P3HT backbones along the out-of-plane direction has been demonstrated by nanoimprinting techniques.[75] This vertical chain alignment enables a fast and efficient charge transport in both OPVs and OLEDs.

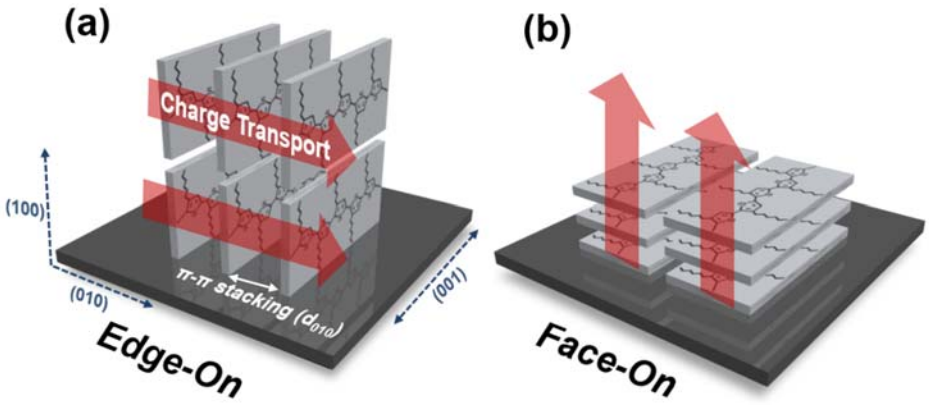

Figure 1.11 (a) Edge-on and (b) Face-on stacking orientations of P3HT crystals.

The above mentioned cases only consider an ideal crystal unit cell, however, several factors such as the number of grain boundaries and interconnectivity between the crystals have to be taken into account when the charge carriers travel throughout the films. Typically, OSCs deposited by solution coating processes exhibit a polycrystalline thin film structure, where the ordered regions are separated by amorphous matrices. In other words, the macroscopic charge carrier mobilities are determined by the combination of charge transport across the highly conductive crystalline regions and poorly conductive disordered domains. Additionally, Frisbie and coworkers[34] have demonstrated that the presence of grain boundaries, which are the interfaces between two crystals, produces a large energy barrier that increases contact resistance, hence prevents effective charge transport between the crystal grains.

The other significant factor lies in the fact that the electronic device performance is strongly dependent on the degree of crystalline anisotropy and the crystal orientation. For example, Reese and coworker[76] have shown that the charge carrier mobility in OFETs is highly anisotropic and consistent with the anisotropic nature of the crystalline structure.

Figure 1.12 illustrates the angular dependence of mobility for vapor-grown rubrene single crystals. The highest field-effect mobility appears when the direction of the source/drain channel aligns with the cofacial π-stacking direction of rubrene crystals, which results in an efficient charge transport pathway. To sum up, the above results suggest that the crystallinity is not the only factor necessary to improve device performance, however, the number of grain boundaries, interconnectivity between the crystal domains and structure anisotropy should also be considered.

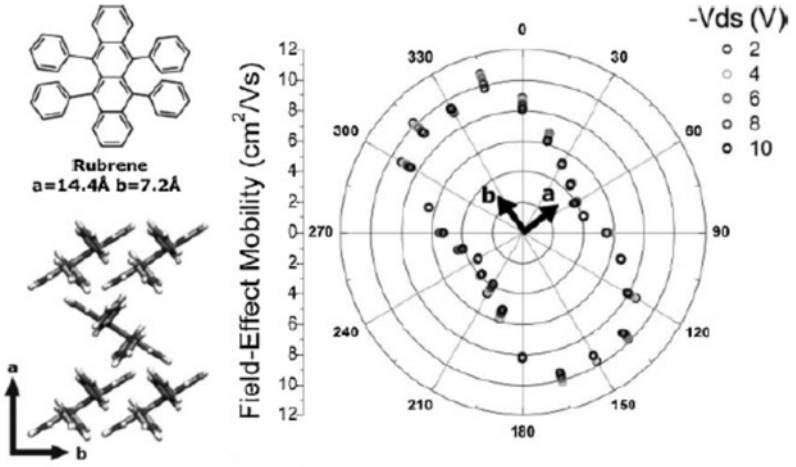

Figure 1.12 Angular dependence of mobility for vapor-grown rubrene single crystals. The molecular and crystal structures are provided on the left hand side.[76, 77]

1.3 OFETs Working Principle and Characterization

1.3.1 Charge Carrier Mobility

Charge carrier mobility refers to how fast an electron or hole can move through a material when applying an electric field. The performance of organic devices mainly depends on the mobility of charge carriers in the active materials. For instance, efficient charge transport facilitates the separation of electron-hole pairs, which are generated by the light absorption in OPVs. Similarly, the rate of charge migration determines how fast the transistors can be switched on and off.

The charge transport is purely diffusive when no external potential is applied to the system. However, the application of an external electric field can induce a drift of charge carriers across the material at a certain velocity, and thus the mobility can be defined as the ratio between the velocity of charge carriers (v) and the magnitude of electric field applied to the materials (E):[70]

$$\mu = \frac{v}{E} \tag{1.3}$$

where μ is the charge carrier mobility, which is specified in units of $cm^2\ V^{-1}\ s^{-1}$.

The charge carrier mobility can be characterized by a range of experimental techniques, including time-of-flight (TOF) measurements, the diode configuration that utilizes space-charge limited current effects to extract the mobility, pulse-radiolysis time-resolved microwave conductivity (PR-TRMC) and using a model field-effect transistor.[70, 78]

The metal-oxide-semiconductor field-effect transistors (MOSFETs) are the most widely used type of transistor in the current electronics industry for devices such as microprocessors, memory devices and integrated circuits. In contrast to MOSFETs based on inorganic materials, OFETs are a field-effect transistor using OSCs as the active layer. However, OFETs typically exhibit equivalent electronic functionality with MOSFETs. OFETs not only can provide a way to evaluate the charge carrier mobility in organic materials but also can be used for the development of next-generation flexible/stretchable electronic devices owing to the irreplaceable mechanical properties of organic materials. As a result, in this thesis, the electronic properties of the OSCs were primarily determined using an OFET configuration. The specific device geometry, working principal and characterization of OFETs will be further discussed in the next section.

1.3.2 OFETs Geometry and Operations

An organic field-effect transistor is composed of the following components (as shown in Figure 1.13a): an organic semiconducting thin film, which is separated from the gate electrode by an insulating gate dielectric; metal source and drain electrodes, which are often vapor-deposited via shadow masking and directly in contact with the semiconducting layer. The length (L) and width (W) of source-drain channel typically range from 10 to 100 μm and 100 to 2000 μm, respectively.[79] Depending on the configuration of electrodes and gate dielectric, the OFETs can be classified as bottom-gate bottom-contact (BGBC), bottom-gate top-contact (BGTC), top-gate bottom-contact (TGBC) and top-gate top-contact (TGTC). (as shown in Figure 1.13b[80]) The BGBC and

BGTC device geometries are employed in this thesis, and the detailed device fabrication processes will be described in the following Chapter.

The application of a voltage (V_G) to the gate electrode leads to polarization of the gate dielectric, and hence induces accumulation of charge carriers within a few nanometers of the semiconducting layer, near the semiconductor–dielectric interface. These accumulated charges subsequently flow from source to drain electrode by applying a voltage (V_D) to the drain electrode, which causes a potential difference between the source and drain. The source electrode is normally grounded ($V_G = 0$). Considering the materials within the active layer, p-type semiconductors exhibit hole transport properties since their HOMO levels closely match the work function of the metal electrodes, whereas n-type semiconductors provide for electron transport because their LUMO levels more closely align with the work function of metal electrodes.[79] Several particular materials may appear to have ambipolar charge transport properties, which enables both hole and electron transport.[81-83]

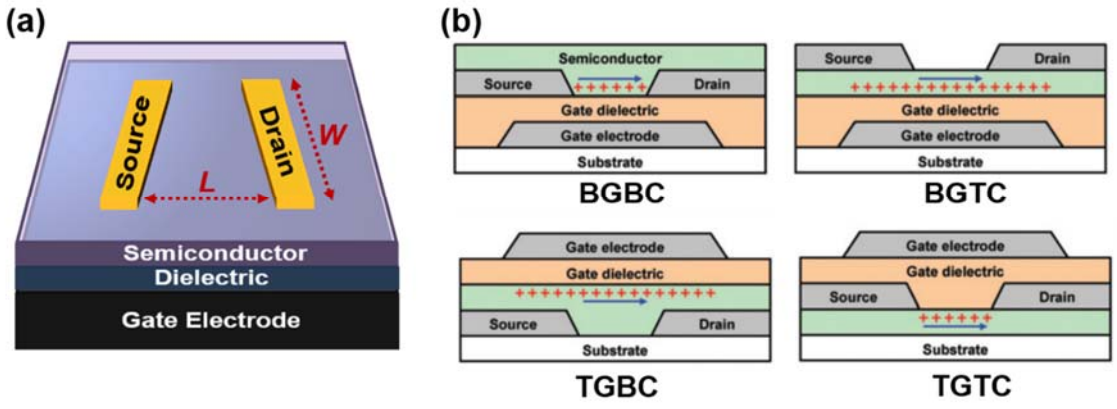

Figure 1.13 Schematic illustration of (a) OFET geometry (b) the cross-sections of the four principle OFET configurations.[80]

1.3.3 Current-Voltage Characteristics

Take p-type OFETs as an example, positive charges are accumulated in the semiconductor when negative V_G is applied to the gate electrode. Ideally, the density of mobile charges is proportional to V_G and the capacitance of the gate dielectric. However, the organic semiconducting thin films, in the real case, exhibit a certain number of charge traps that should be filled before the induced p-channel can begin to conduct. That is, V_G has to overcome a threshold voltage (V_{Th}), leading to an effective gate voltage ($V_G - V_{Th}$).[79, 82]

OFETs can be operated in the linear and saturation regions, depending on the magnitude of V_{DS} relative to ($V_G - V_{Th}$). When no V_D is applied to the drain electrode, the positive charge carrier density is uniform across the channel. The application of small V_D, which is less than the effective gate voltage ($V_D \ll (V_G - V_{Th})$) leads to a linear gradient of charge density within the channel. Hence, the density of mobile charges (Q_{mob}) can be accounted for in the following Equation 1.4:[79]

$$Q_{mob} = n(x)et = C_i(V_G - V_{Th} - V(x)) \tag{1.4}$$

where C_i is the capacitance per unit area of the gate dielectric, x is the given positon along the channel, $n(x)$ is the number density of charges, e is the elementary charge (1.6×10^{-19} C) and t is the thickness of the charged layer in the active channel. This operating regime of OFETs is defined as the linear regime (Figure 1.14a). In this regime, the average value of Q_{mob} is $C_i(V_G - V_{Th} - \frac{V_D}{2})$, which is the areal charge density at the

center of the induced channel. According to Ohm's law and the definition of conductivity ($\sigma = ne\mu$), the source–drain current (I_D) can be expressed as:

$$\frac{1}{R} = \frac{I_D}{V_D} = \sigma\frac{Wt}{L} = (ne\mu)t\frac{W}{L} = Q_{mob}\mu\frac{W}{L} \tag{1.5}$$

$$I_D = Q_{mob}\mu\frac{W}{L}V_D = \frac{W}{L}C_i\mu(V_G - V_{Th} - \frac{V_D}{2})V_D \tag{1.6}$$

$$I_D = \frac{W}{L}C_i\mu\left[(V_G - V_{Th})V_D - \frac{V_D^2}{2}\right] \tag{1.7}$$

As $V_D \ll (V_G - V_{Th})$, the Equation 1.7 is approximately correct to drop the $\frac{V_D^2}{2}$ term,

$$I_D = \frac{W}{L}C_i\mu(V_G - V_{Th})V_D \tag{1.8}$$

$$\mu_{lin} = \frac{L}{WC_iV_D}\frac{\partial I_D}{\partial V_G} \tag{1.9}$$

where R is the resistance, σ is the conductivity, W is the source–drain channel width, L is the channel length and μ is the charge carrier mobility. The Equation 1.9 is commonly used for determining the charge carrier mobility in the linear regime.

When V_D is increased up to $V_D = (V_G - V_{Th})$, the charge carriers become completely depleted near the drain electrode, the so called pinch-off point as shown in Figure 1.14b. The charge carriers are swept from this pinch-off point to the drain by the electric field in the narrow depletion zone. However, a further increase in source–drain voltage ($V_D > (V_G - V_{Th})$) can only push the pinch-off point slightly backward toward

the source electrode, and thus yield no additional current. The substitution of $V_D = (V_G - V_{Th})$ into Equation 1.6 leads to current-voltage characteristics of OFETs in the saturation regime, which is defined by the Equation 1.10:

$$I_D = \frac{W}{2L} C_i \mu (V_G - V_{Th})^2 \tag{1.10}$$

The charge carrier mobility in the saturation regime (Figure 1.14c) can be extracted by the Equation 1.11:

$$\mu_{sat} = \frac{2L}{WC_i} \left(\frac{\partial I_D^{0.5}}{\partial V_G} \right)^2 \tag{1.11}$$

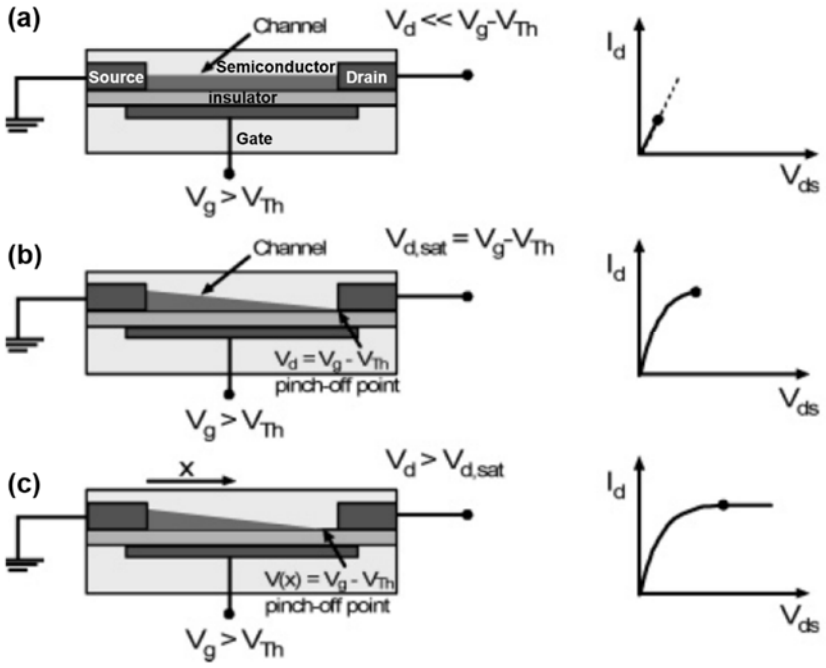

Figure 1.14 Schematic structure of OFETs (left) and the corresponding current-voltage characteristics (right) in (a) linear regime (b) pinch-off point and (c) saturation regime.[82]

Figure 1.15a illustrates the typical output characteristics, showing the development of I_D versus V_D for different constant V_G. The linear and saturation regions of OFETs can

be clearly distinguished in the output curve. Figure 1.15b and c shows the transfer characteristics of OFETs operated in the linear and saturation regimes, respectively, demonstrating the development of I_D versus V_G at constant V_D. A semilog plot (left) and a linear plot (right) are included in these transfer curves. For the semilog plot, the ratio of maximum and minimum I_D provide the value of I_{ON}/I_{OFF}, which indicates theswitching behavior of the transistor. This ratio should be as large as possible. For the linear plot, the gradients of the I_D and $I_D^{0.5}$ are directly proportional to the charge carrier mobility in the linear and saturation regimes, respectively. Hence, the charge carrier mobility can be determined by the Equation 1.9 and 1.11. Another important factor, V_{Th} can also be calculated from the transfer curves by extrapolating the linear fit of $I_D^{0.5}$ to x-axis. The charge carrier mobility (μ), threshold voltage (V_{Th}) and on-to-off current ratio (I_{ON}/I_{OFF}) obtained from the current-voltage characteristics are the three key figures of merit used for assessing the performance of OFETs.

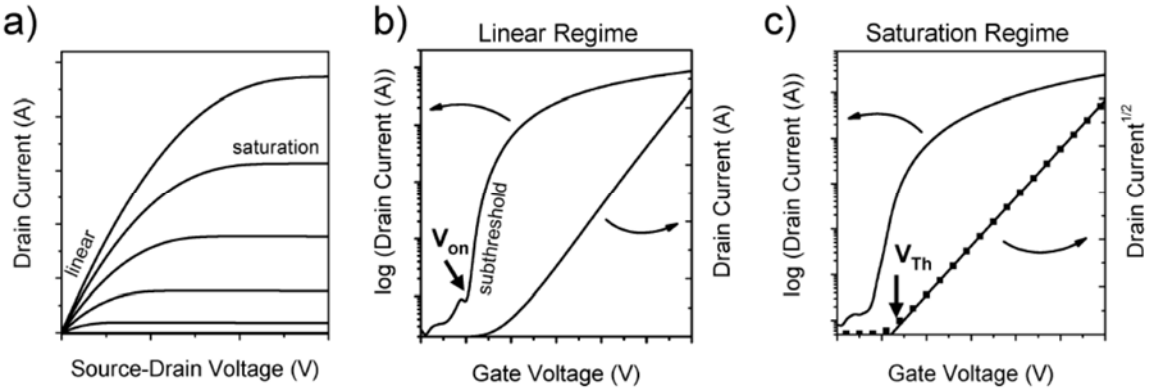

Figure 1.15 (a) output characteristics, indicating the linear and saturation regime (b) transfer characteristics in the linear regime (c) transfer characteristics in the saturation regime, indicating the threshold voltage, V_{Th}.[82]

1.4 Poly (3-hexylthiophene)

Thiophene is a planar aromatic heterocyclic compound, which can form a wide range of conjugated polymers via appropriate coupling. Typically, unsubstituted polythiophene is barely soluble in most of organic solvents, which impedes the processability and applications in electronic devices. To deal with this issue, the introduction of an alkyl side chain, which is a solubilizing substituent, into the polythiophene backbones can greatly enhance the solubility of resulting polymers. Babel and coworkers[84] further demonstrated that the poly(3-hexylthophene) (P3HT), which is laterally substituted with hexyl side chains exhibits optimum charge transport properties in comparison to the other polythiophenes with different length of alkyl side chain. To date, P3HT has become an exemplary semiconducting polymer for a variety of electronic applications because of its commercial availability, solution processability, fair charge transport performance and tunable mechanical properties.

P3HT exhibits a strong tendency to self-assemble when cast from solution phase into solid thin films, resulting in a nanofibrillar crystalline structure, which is comprised of multiple π-stacked P3HT polymer chains. The idealized P3HT packing structure is illustrated in Figure 1.16, which reveals that the length of the polythiophene repeat unit is ca. 0.38 nm, the *d*-spacing of lamellar stacking is ca. 1.6 nm and the π-π stacking spacing along the long-axis of nanofiber is ca. 0.38 nm.[85-88] As we mentioned in section 1.2, the intra- and intermolecular interactions of conjugated polymers are critical to charge transport. Herein, many significant efforts have been made in order to improve the molecular packing structure of P3HT and corresponding OFET performance. The charge

carrier mobility of P3HT ranges from 10^{-5} to approximately 0.2 $cm^2V^{-1}s^{-1}$ depending on the molecular design, processing techniques and pre/post-treatments.

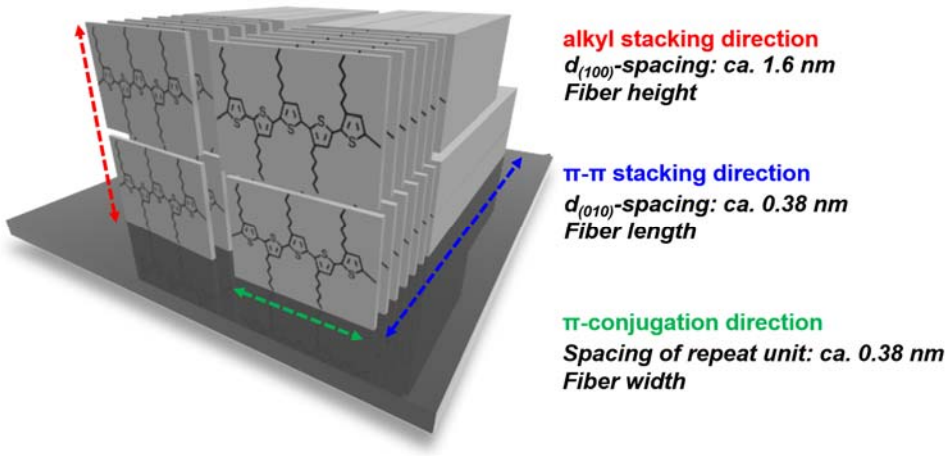

Figure 1.16 P3HT edge-on packing structure, indication the direction of alky staking, π-π stacking and π-conjugation.

In terms of the molecular design of P3HT, the molecular weight (MW)[89-92] and regioregularity[60, 74, 93-97] are both identified as key molecular parameters that control thin film microstructure and thus charge transport properties. For example, Kline and coworkers[89] presented that the charge carrier mobility is highly dependent on the MW of P3HT. As shown in Figure1.17a, the low-MW (3.2 kD) sample demonstrated rod-like crystals whereas no apparent crystalline features can be observed in high-MW films (31.1 kD). This result is consistent with XRD data (Figure 1.17b), which showed that the low MW P3HT has a more pronounced (100) diffraction peak than high MW films. One might expect that higher ordering in the thin film structure should provide better charge transport performance, however, the results are totally opposite. It was found that the decrease of MW from 33.5 to 3.2 kDa leads to significant decrease in mobility from 9.4×10^{-3} to 1.7×10^{-6} $cm^2\ V^{-1}\ s^{-1}$. In other words, the low-MW samples with high degree

of thin film crystallinity have charge carrier mobility much lower that the high-MW analogs with a relatively less ordered structure. The authors explained that a large number of grain boundaries between the rod-like crystals are mainly responsible for the poor charge carrier mobility in low-MW films. In contrast, the long polymer chains in high-MW films not only increase the opportunities for charge hopping to neighboring chains but also enhance the connection between the ordered regions via tie-chains, and therefore facilitating the charge transport throughout the films.[98]

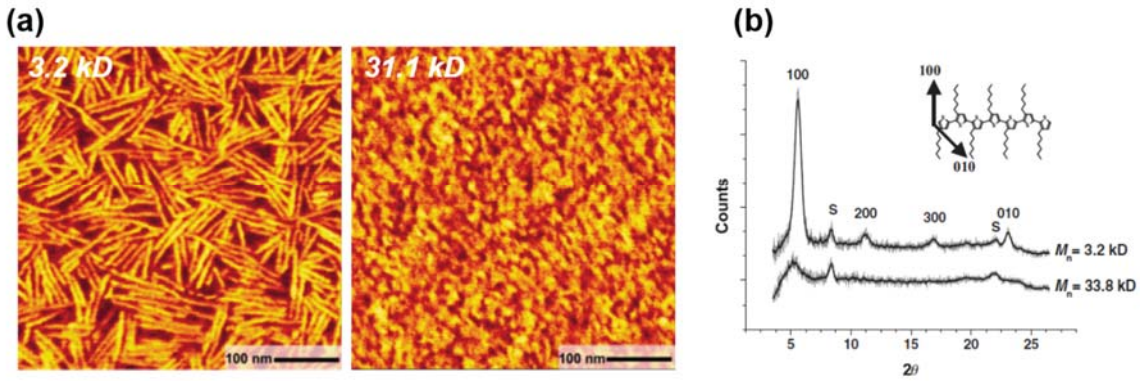

Figure 1.17 (a) AFM phase images of 3.2 and 31.1 kD P3HT films. (b) XRD of P3HT films shows a more intense (100) diffraction peak for the 3.2 kD samples in comparison to 33.8 kD analogs.[89]

The other important molecular parameter that affects the crystalline structure of P3HT is regioregularity, which is defined as the percentage of head-to-tail attachments of the hexyl side chains to the polymer backbone. Pioneering research revealed that regiorandom (RRa) P3HT possesses a high percentage of head-to-head (H-H) moieties that lead to strong steric interactions between adjacent monomers giving rise to increased torsion, which interrupts the delocalization pathway for charge carriers.[95, 99-101] In contrast to RRa-P3HT, Sirringhaus and coworkers[74] showed that highly regioregular (RR) P3HT

affords films with increased crystallinity and interchain interactions, and thus higher charge carrier mobilities. While a high percentage of H-T coupling is essential for the development of high performance semiconductors, several studies suggest that polymer molecular structures with some limited degree of disorder in the conjugated backbone prove beneficial for some applications, e.g., the thermal stability of polymer-fullerene composite solar cells.[96, 102] Recently, Kim and coworkers[60] revealed that the elongation at break of RR-64% films is an order of magnitude higher than RR-98% films by floating the corresponding films over the water surface for mechanical tests. (Figure 1.18) The reasons for this lies in the fact that highly crystalline RR-98% films are much stiffer and more brittle than the low RR P3HT films that exhibit less crystallinity.

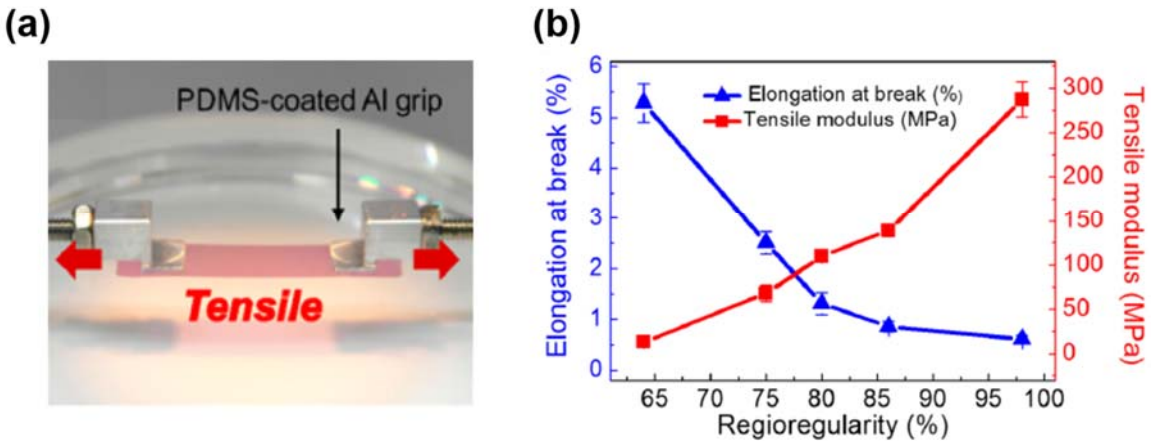

Figure 1.18 (a) P3HT thin films floating on the water surface for tensile testing. (b) Elongation at break and tensile modulus of P3HT thin films as a function of regioregularity.[60]

The above mentioned P3HT thin film properties such as crystallinity, electrical and mechanical properties can also be manipulated by a number of extrinsic process methodologies. For example, the selection of organic solvents plays a crucial role in

supramolecular assembly of polymer chains during thin film formation process since these solvents possess different solubility, polarity and boiling point.[37, 40, 103] The pre/post-deposition treatments (e.g., deposition of self-assembly monolayer,[104] thermal annealing,[105] solvent vapor annealing[106]) not only facilitate the formation of an ordered thin film structure, but also improve the contact between the semiconductor and the source/drain electrodes. Many other reported processing approaches include ultrasonication,[107, 108] blending,[109, 110] aging,[111] UV-irradiation,[112] template-assisted self-assembly,[75] etc. Further understanding and controlling the morphology of conjugated polymers is essential for the development of high performance P3HT based-OFETs.

1.5 Motivation and Outline of Thesis

This thesis mainly focuses on the study of processing–structure–property relationships associated with OSCs for the development of vital knowledge correlated with molecular packing structure and processing approaches, and how these parameters ultimately impact the thin film crystallinity, surface morphology, photophysical properties, charge transport performance and device ambient stability. Specifically, in this study, P3HT was selected as a model OSC for the investigation of intra- and intermolecular interactions in both solution and solid states. And the films were deposited as the active layer in OFETs for further electrical property characterization.

Chapter 2 unraveled the complex correlations between the microstructures of OSC thin films and their corresponding charge transport behaviors in OFETs. In addition, the device stability issues associated with the oxidative doping effect was effectively

controlled by incorporating air-stable oligomers into polymeric semiconductors. The processing can be conducted without pre-/post-treatments and stringent oxygen/moisture-limited conditions, suggesting a promising approach for industrial-scale production. As mentioned, the primary advantage of OSCs is their facile solution processability which shows the potential to reduce the production cost and hence makes them competitive and irreplaceable in the semiconductor industry. Herein, the blade coating method, which is compatible with roll-to-roll printing production was developed in Chapter 3. The combined strategy of using a solution preprocessing technique and blade coating was shown to induce a long-range ordering and macroscopic alignment of the P3HT nanofibrillar thin film structure, which also exhibits remarkable optical and charge transport anisotropy. In Chapter 4, the OSCs were further deposited on flexible plastic substrates in order to evaluate their charge transport characteristics when the devices were bent repeatedly at a certain range of external strain. Although the device performance of these OFETs might not surpass inorganic single-crystal semiconductors, their potential for flexible applications still turned a new page in the development of electronic devices. Chapter 5 will summarize the main findings in each chapter and provide suggestions for future research.

CHAPTER 2. ENHANCED MOBILITY AND EFFECTIVE CONTROL OF THRESHOLD VOLTAGE IN P3HT-BASED OFET VIA INCLUSION OF OLIGOTHIOPHENES

2.1 Introduction

Organic field-effect transistors (OFETs) have attracted considerable attention because of their facile processability, chemical tunability, potential for low-cost, high-throughput fabrication over large-area flexible plastic substrates, and compatibility with a wide range of optoelectronic devices, such as flat-panel displays, disposable sensors, radio frequency identification tags, and so forth.[113-116] P3HT is a commercially available and widely investigated hole transport conjugated polymer, which lends itself to investigation of the correlation between thin-film microstructure and charge transport performance. To date, many different processing methods have been proposed, such as poor solvent addition,[35] shear-induction,[117] and ultrasonication,[118] with the aim of increasing P3HT chain ordering and alignment, thus enhancing effective charge carrier transport within the polymer films.

Although conjugated polymer semiconductors can have certain processing and morphological advantages over their oligomer counterparts, polymers have their own issues. For instance, chain entanglement, chain folding, and broad polydispersity, which lead to a decrease in crystallinity can negatively impact charge carrier mobility.[119, 120] A straightforward approach to address these problems is to blend oligomer and polymer semiconducting materials to take advantage of the attributes of both components, while

concomitantly compensating for the disadvantages. The resultant blend thin films are expected to combine the high crystallinity of the oligomers with the morphological features and interchain connectivity associated with the polymer component.

The polymer−oligomer blend approach was first reported by Russell et al.[121] who showed that P3HT thin-film mobility can be enhanced almost 10-fold by incorporating the conjugated oligomer, dihexyl-quarterthiophene (DH4T). These devices exhibited a pronounced mobility enhancement as the DH4T concentration increased from 20 to 35 wt %. The mobility saturated (μ = 0.01 $cm^2 V^{-1} s^{-1}$) when P3HT was blended with 50 wt % DH4T. The improved charge transport performance was ascribed to the formation of oligomer crystals embedded in the polymer matrix, while effective charge transport percolation pathways formed. In another study, Orgiu et al.[122] demonstrated that charge carrier mobility of P3HT increases when the semiconducting oligomer, 5,5-bis(4-nhexylphenyl)-2,2-bithiophene (dH-PTTP), is co-deposited with the polymer. Mansouri and co-workers[123] further investigated the photosensing and electrical properties of organic thin-film transistors based on the blend of TIPS-pentacene and P3HT prepared by solution processing. Recent work by Gemayel et al.[124] proposed a new strategy to improve transistor performance and showed the potential for P3HT:graphene nanoribbon (GNR) blends.

Although the results reported to date showed that field-effect mobilities can be improved through a polymer−oligomer blend approach, a number of serious issues remain: a high threshold voltage (V_{Th}) ($|V_{Th}|$ > 10 V), or need for additional pre- or post-treatments to avoid the compromising V_{Th} and on−off current ratio (I_{ON}/I_{OFF}) are representative examples. Low V_{Th} is required for devices to be compatible with the

operating voltages of low power consumption logic circuits and portable electronic devices. However, control of V_{Th} to a value close to zero remains difficult.

Herein, the conjugated oligothiophene, BTTT (Figure 2.2a), is incorporated into P3HT thin films with the aim of improving overall semiconducting performance, not only as measured by mobility, but also by V_{Th} and I_{ON}/I_{OFF} ratio. BTTT was selected as the oligomeric small molecule component due to its planar symmetrical fused aromatic rigid frame, i.e., thieno[3,2-b]thiophene, which promotes the formation of highly ordered crystalline domains. Also, relative to the thiophene ring structure of P3HT, the thienothiophene is more stable with regards to oxidation. Blended thin films were deposited in the absence of electrode or dielectric treatment with self-assembled monolayers or post-treatments such as thermal annealing. All thin-film deposition processing was conducted under ambient conditions using a volatile, low boiling point solvent. These features are compatible with solution processing under nonstringent fabrication conditions and high-throughput processing.

2.2 Experimental Methods

2.2.1 Materials

The P3HT (MW: 60 kD, PDI: 1.9 RR: 96%) and chloroform (anhydrous grade) were purchased from Rieke Metals Inc. and Sigma-Aldrich, respectively, and used without further purification. The BTTT was synthesized according to the literature procedure.[125]

2.2.2 OFETs Fabrication and Characterization

The bottom-gate bottom-contact OFET substrates were fabricated using a heavily n-doped silicon wafer as the gate electrode. A 300 nm thick layer of thermally grown SiO_2 served as the gate dielectric. The 50 nm Au source and drain electrodes with 3 nm Cr as the adhesion layer were both deposited via standard photolithography based lift-off processing, followed by E-beam evaporation onto the SiO_2 layer. Before semiconducting layer deposition, all devices were cleaned in an ultrasound cleaning bath and sequentially rinsed with acetone, methanol and isopropanol. At the final step of the cleaning process, the devices were exposed to UV-ozone to ensure complete removal of residual photoresist and other organic contaminants.

Before the thin-film formation process, pristine P3HT (0.33 wt %) and BTTT (0.33 wt %) solutions were prepared in $CHCl_3$ at ca. 55 °C with stirring. Subsequently, the respective blend solutions were prepared by mixing the defined ratios of the well dissolved pristine P3HT and BTTT solutions as listed in Table 2-1. The fabrication of OFET devices was completed by spin-coating P3HT:BTTT blend solutions onto the precleaned substrates under ambient condition. All OFET electrical properties were tested using an Agilent 4155C semiconductor parameter analyzer. The field-effect mobilities, threshold voltage and I_{ON}/I_{OFF} were calculated in the saturation regime (V_D = −80 V) from the transfer plot of V_G versus I_D and using the following Equation 2.1:

$$I_D = \frac{W}{2L} C_i \mu (V_G - V_{Th})^2 \tag{2.1}$$

where W and L refer to the channel length (50 μm) and width (2 mm), respectively, μ represents the hole mobility, V_{Th} is the threshold voltage, and C_i is the capacitance per unit area of the SiO_2 gate dielectric (1.15×10^{-8} F cm^{-2}).

Table 2-1 List of P3HT:BTTT blend ratio and percentage by weight of BTTT in blend films

P3HT solution : BTTT solution	Percentage by weight of BTTT in blend films
100 : 0	0%
90 : 10	10%
70 : 30	30%
50 : 50	50%
30 : 70	70%
10 : 90	90%
0 : 100	100%

2.2.3 UV-vis Spectroscopy (UV-vis)

The solution and solid state UV−vis spectra were measured by using an Agilent HP 8510 UV−vis spectrophotometer. The thin films for the solid-state studies were prepared by spin coating the relevant solution onto precleaned glass slides, which had undergone the same clean procedure as indicated above for OFET devices. (Figure 2.1)

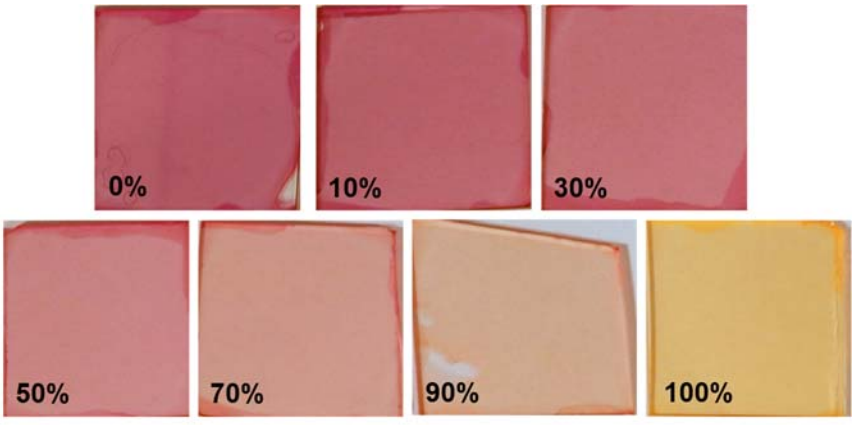

Figure 2.1 P3HT:BTTT blend thin films deposited on glass slides.

2.2.4 Grazing-Incidence X-ray Diffraction (GIXD)

Out-of-plane grazing incidence X-ray diffractograms were collected using a Panalytical X'Pert Pro system equipped with a Cu Ka X-ray irradiation source (λ = 1.541 Å), and operating at 45 kV and 40 mA. The X-ray incidence angle was fixed at 0.2° and the detector was scanned from 3 to 30°. The samples for GIXD characterization were prepared by spin coating relevant solutions onto silicon substrates, having a 300 nm silicon oxide layer.

2.2.5 Atomic Force Microscopy (AFM)

The surface morphology of the blend thin films with different blend ratios were characterized by AFM using a Bruker Dimension Icon atomic force microscopy system, operating in tapping mode with a silicon tip (TAP150, Bruker).

2.2.6 Ultraviolet Photoelectron Spectroscopy (UPS)

Ultraviolet Photoelectron Spectra were obtained on a Kratos Axis Ultra DLD XPS/UPS system, using a 21.2 eV He-ion UV light source. The UPS data were recorded at a 5 eV pass energy and 0.05 eV step size with the spot diameter set to 55 μm. The ionization potential (IP = −HOMO)

and work function (∅) were calculated by the following Equations 2.2 and 2.3:

$$IP = hv - (E_{cutoff} - \varepsilon_V^F) \tag{2.2}$$

$$\emptyset = hv - E_{cutoff} \tag{2.3}$$

where $h\nu$, E_{cutoff}, ε_V^F denote the incident photo energy (He I, 21.2 eV), the secondary electron cutoff energy value, and the lowest binding energy point, respectively.

2.3 Results and Discussions

2.3.1 Photophysical Properties

The optical absorption spectra obtained from P3HT:BTTT solution and corresponding blend thin films were measured by UV−vis spectroscopy. In solution (Figure 2.2b), pristine P3HT (0% BTTT) exhibits a single absorption maximum, λ_{max}, associated with the π−π* intraband transition at ca. 450 nm, consistent with previous reports.[126-128] For the 100% BTTT oligomer solution, λ_{max} appears at ca. 350 nm and does not overlap with the pristine P3HT absorbance. Both distinct absorption bands can be observed in the polymer-oligomer blend solutions and the peak intensities vary with the blend ratios. The P3HT absorption bands associated with vibronic structure showing a 0−0 transition at ca. 605 nm and a 0−1 vibronic sideband at ca.550 nm are absent in the solutions.[128, 129]

In contrast to the solution results, P3HT:BTTT blend thin films exhibit notably different UV−vis spectral features (Figure 2.2c). The absorption bands at ca. 550 nm and ca. 340 nm represent the P3HT and BTTT π−π* intraband transitions, respectively. The ratios of these bands are consistent with the polymer:oligomer proportions. In addition, the P3HT absorption peaks show an apparent red−shift (from ca. 450 to ca. 550 nm) with respect to the corresponding solution state spectra due to a higher degree of polymer

chain planarization in the solid state.[130, 131] To gain insight into the development of the P3HT absorption bands, we normalized the bands at ca. 550 nm, as shown in Figure 2.2d. Unlike the identical solution state P3HT spectral features with different blend ratios, the absorption bands in the solid state display a bathochromic shift as a function of additional oligomer concentration, meanwhile the weak absorption band at ca. 605 nm becomes progressively more pronounced. These features are both ascribed to enhancement of cofacial π−π stacking and/or planarization of the conjugated backbone.[128, 129]

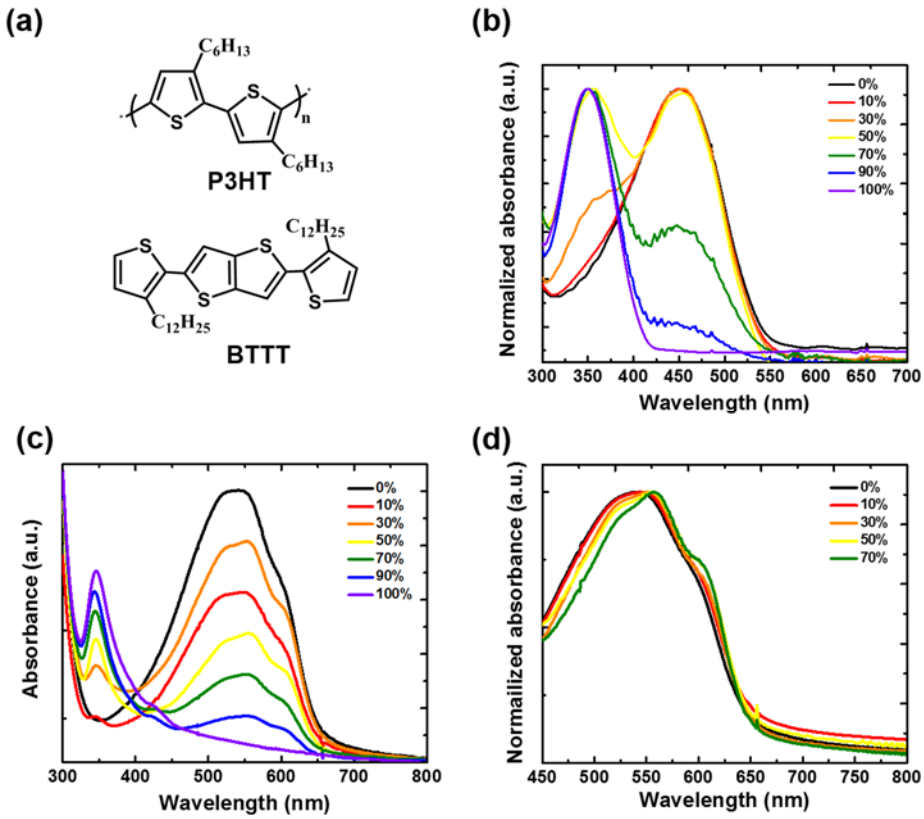

Figure 2.2 (a) Molecular structures of P3HT and BTTT. (b) Normalized UV−vis absorption spectra of P3HT:BTTT blend solutions with varying P3HT:BTTT blend ratio. (c) UV−vis absorption spectra and (d) normalized UV−vis absorption spectra of P3HT:BTTT blend thin films with different blend percentages of BTTT with respect to P3HT. (The normalized absorption bands for 90 and 100% blend thin films are not provided because the peaks at ca. 550 nm are too small or absent.)

The model by Spano enables a quantitative analysis of P3HT absorption spectra with respect to the analysis of intra- and intermolecular ordering of polymer chains.[131-133] The film absorption spectra are composed of a crystalline region because of ordered chains and an amorphous higher energy region due to disordered chains. Within the crystalline regions, interchain coupling contributes to the formation of vibronic bands. The magnitude of interchain coupling can be estimated from the ratio of the 0−0 and 0−1 vibronic bands, which correlates with the free exciton bandwidth (W) of the aggregates.[129, 133] A decrease of W can be ascribed to an increase in conjugation length and/or chain ordering. The values of W were calculated by the following Equation 2.4:

$$\frac{I_{0-0}}{I_{0-1}} \approx \left(\frac{1 - 0.24W/E_p}{1 + 0.073W/E_p}\right)^2 \tag{2.4}$$

I_{0-0} and I_{0-1} represent the intensities of the 0−0 and 0−1 transitions, respectively obtained from fits to the experimental spectra (Figure 2.3a−e). E_p denotes the vibrational energy of the symmetric vinyl stretch at 0.18 eV.[131, 133] The W value of both pristine P3HT and blend solutions could not be estimated since no aggregation was observed in the solution state. However, W for pristine P3HT thin film appears at 158.4 meV as shown in Figure 2.3f. Notably, this value continuously decreased to 93.35 meV with increased BTTT blend ratio up to 70%, suggesting that inclusion of the crystalline oligomer into the P3HT matrix may promote intermolecular ordering with increasing oligomer concentration.

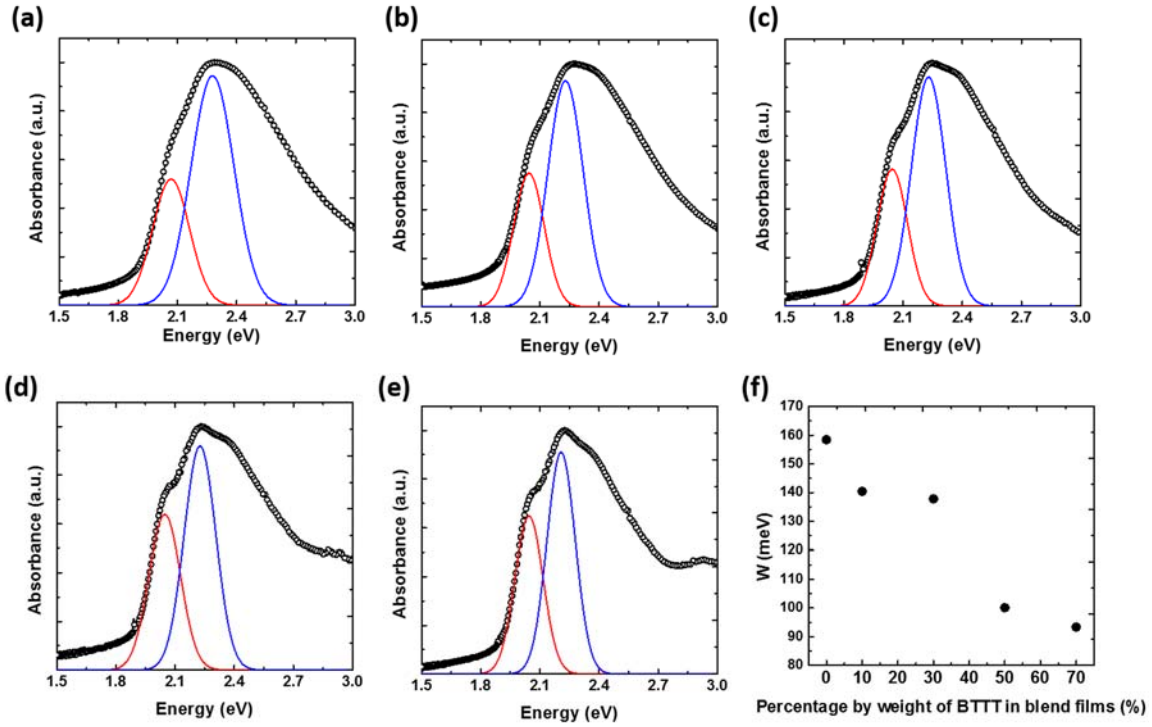

Figure 2.3 Absorption spectra of P3HT:BTTT blend thin-films, fabricating with a range of weight percentage of BTTT in blend films (a) 0%, pristine P3HT, (b) 10%, (c) 30%, (d) 50%, (e) 70%. The black open circles are the experimental absorption spectra. The red and blue Gaussian fitted lines indicate 0−0 and 0−1 vibronic transition bands respectively. (f) Evolution of exciton bandwidth *W* as a function of additional BTTT weight ratio.

2.3.2 Thin Film Crystallinity

Grazing incidence X−ray diffraction (GIXD) measurements were performed to confirm P3HT:BTTT blend thin film microstructure as shown in Figure 2.4a. For pristine P3HT, the diffractogram presents a relatively weak and broad (100) peak associated with a lamellar packing structure of polymer chains,[103, 134, 135] and is indicative of either less ordering or an amorphous morphology. In contrast to the polymer thin film where crystallinity might be inhibited by chain entanglement, chain folding, or polydispersity, oligomer or low-molecular weight polymers crystallize more readily during rapid thin-

film forming conditions such as spin coating.[119] Thus, it can be expected that addition of the oligomer led to an increase in (100) peak intensity, which could be ascribed to either an increase in individual crystal size, number of crystallites, or both.[107] Pure, drop cast BTTT and P3HT thin films were also measured by GIXD as shown in Figure 2.5. The results reveal that the pristine semiconductors exhibit diffraction peaks at 2θ = 5.40° (*d*-spacing = 16.35 Å) and 2θ = 5.43° (*d*-spacing =16.26 Å), respectively, which are in close proximity to each other. Overlap between the XRD peaks makes it difficult to evaluate the improvement of P3HT crystallinity in blend thin films. Fortunately, the P3HT and BTTT thin films show a distinct absorption band, which can provide an alternative perspective to evaluate polymer chain structural ordering in the two-component system.

As discussed above, UV−vis spectral analysis suggests that not only does the crystalline BTTT contribute to the enhanced diffraction peaks of blends but the enhancement can also partially be attributed to improved P3HT ordering. The size of the crystalline domains could be further estimated using the Scherrer's equation,[136, 137] where λ is the incident X-ray wavelength, K is a crystallite-shape factor, θ is the Bragg angle, B is the full-width at half-maximum (FWHM) obtained from the X-ray diffraction peak in radians, and L represents the size of crystallites.

$$L = \frac{K\lambda}{B\cos\theta} \tag{2.5}$$

In the case of pristine P3HT thin films, the value of L could not be calculated because of the amorphous morphology. With an increase in BTTT weight percent, the (100) peak

FWHM decreased. Thus, the calculated crystallite size grew from about 70 to roughly 180 Å as shown in Figure 2.4b.

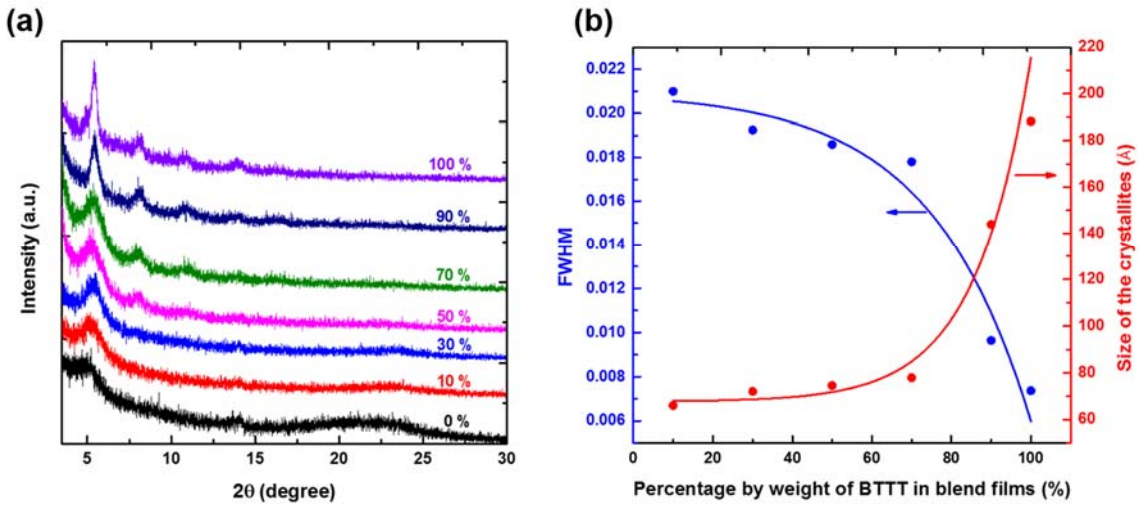

Figure 2.4 (a) GIXD profiles of P3HT:BTTT blend thin films with varying additional oligomer concentrations. (b) FWHM of (100) peaks and corresponding size of crystallites as a function of P3HT:BTTT blend ratio.

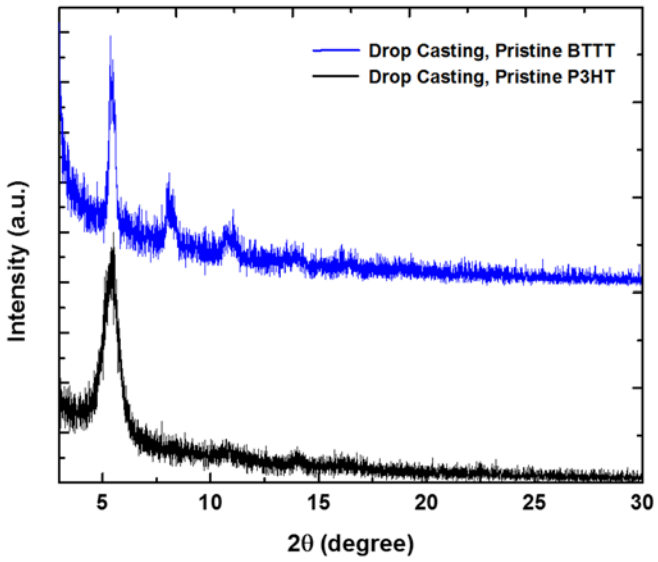

Figure 2.5 GIXD profiles of pristine P3HT and pristine BTTT thin-films deposited by drop casting.

2.3.3 Surface Morphology

P3HT:BTTT blend thin-film surface morphologies were investigated by tapping mode Atomic Force Microscopy (AFM). Phase images (2 × 2 μm) of the blends are presented in Figure 2.6. For pristine P3HT or blend thin films with low levels of BTTT, the topographic images lack crystalline texture, consistent with the amorphous structure observed through XRD analysis. However, island-like features begins to appear and increase in size as the BTTT weight ratio rose over 30%. Concomitantly, surface roughness increased from 0.6 to 9.7 nm as shown in Figure 2.7, in further support of increased thin film crystallinity and molecular ordering. The images suggest that the polymer:oligomer blend thin films are comprised of crystals separated by an amorphous matrix. Increasing the oligomer fraction further, the crystal size became larger and then near 100%, evolved into a lump-like film structure with decreased surface roughness (9.7 to 3.9 nm). It is worth noting that although pristine BTTT shows a highly ordered structure compared to pristine P3HT or blended thin films, the crystal size is not sufficient to fully cover the active channel (50 μm). Thus, charge transport between source and drain electrodes may be limited because of the large number of grain boundaries, and lack of interconnectivity between domains.

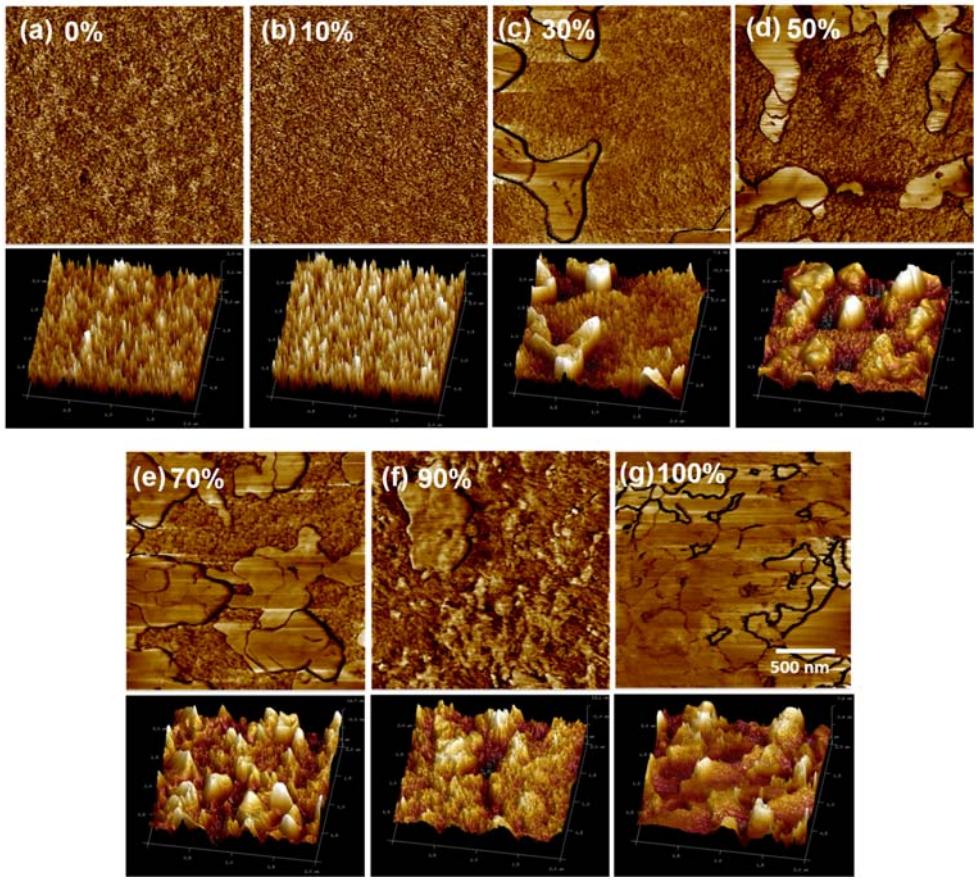

Figure 2.6 Tapping mode AFM phase images (upper) and corresponding 3D height images (lower) of P3HT:BTTT blend thin films, fabricating with a range of BTTT weight percentage in blend films (a) 0%, pristine P3HT, (b) 10%, (c) 30%, (d) 50%, (e) 70%, (f) 90%, (g) 100%, pristine BTTT. The scan area of all images was 2 × 2 μm.

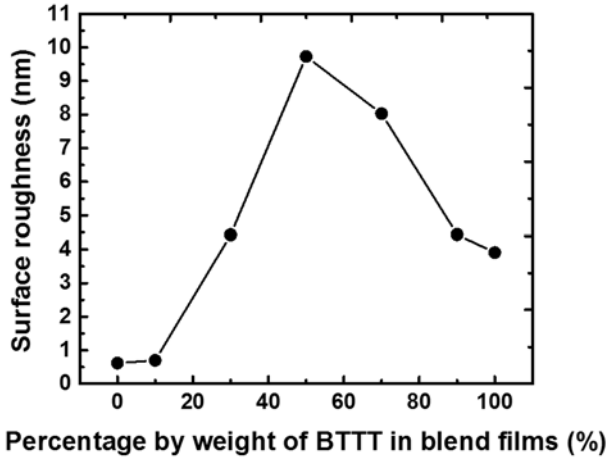

Figure 2.7 Surface roughness of P3HT:BTTT blend thin-films as a function of additional BTTT weight ratio.

2.3.4 Charge Transport Performance

The charge-carrier transport properties of P3HT:BTTT blend thin films were investigated by spin coating respective blend solutions onto bottom-gate bottom-contact field-effect transistor substrates. The channel length and width between source and drain gold electrodes was 50 μm and 2 mm, respectively. Figure 2.8a, c and d depict the transfer and output curves for devices fabricated with P3HT:BTTT blends, and the resulting average mobilities, as a function of the BTTT weight percent, are presented in Figure 2.8b. The average mobility was calculated in the saturation regime at −80 V drain voltage.

As shown in Figure 2.8b, the pristine P3HT thin film exhibited a mobility ($9.37 \pm 1.00 \times 10^{-3}$ cm^2 V^{-1} s^{-1}) and large threshold voltage (40.0 ± 5.0 V). All devices were fabricated under ambient conditions with no electrode/dielectric surface treatment or postdeposition processing such as thermal annealing were employed. Hence, residual doping and/or acceptor-like traps at the P3HT-oxide interface are inevitable and are likely responsible for the high threshold voltage.[138, 139] In other words, a decrease in carrier trap density is favorable for decreasing the threshold voltage. However, P3HT is very susceptible to atmospheric oxygen due to its relatively low ionization potential (IP).[48, 140, 141] Thus, some oxygen is expected to diffuse into the P3HT thin films generating a P3HT-O_2 complex, which can act as a charge carrier trap and lead to a positive shift in threshold voltage.[142-146] The semiconducting performance did not show any improvement upon addition of a small quantity of BTTT (10%). However, the charge carrier mobility was enhanced approximately 5-fold with a BTTT weight ratio up to 50%. Significantly, the threshold voltage decreased from 40.0 ± 5.0 V to 1.7 ± 4.3 V, whereas the I_{ON}/I_{OFF}

improved from 1×10^4 to 1×10^5 as shown in Figure 2.8a-b. Additionally, the output characteristics of the 1:1 P3HT:BTTT blend thin film presents apparently different features with respect to pristine P3HT, which showed only partial saturation. An ideal OFET should enter the saturation region when $V_D \geq (V_G - V_{Th})$. In other words, further increases in V_D should yield no additional drain current.

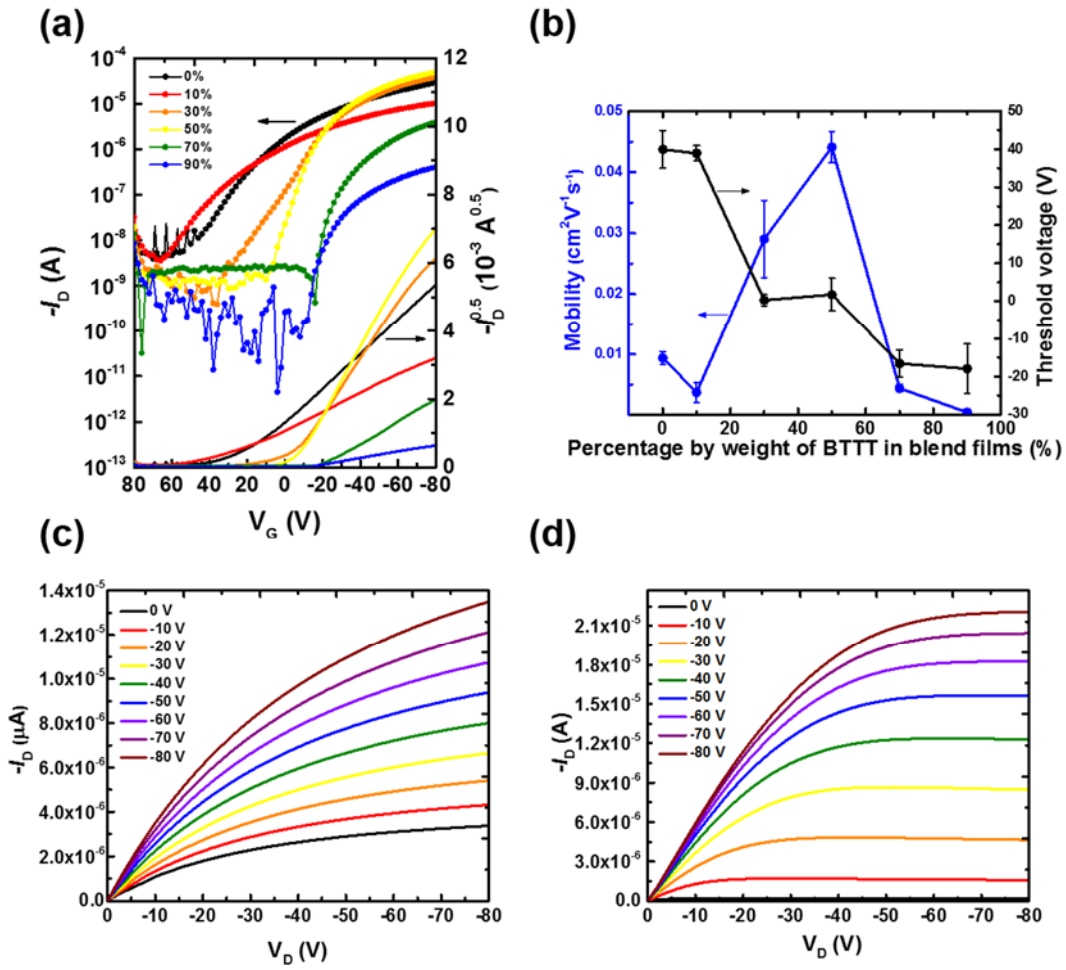

Figure 2.8 (a) Transfer characteristics of P3HT:BTTT blend OFETs with different blend percentages of BTTT (V_D = −80 V). (b) Average field-effect mobility and threshold voltage obtained from P3HT:BTTT blend OFET devices as a function of oligomer concentrations. Output characteristics of (c) pristine P3HT and (d) 50% P3HT:BTTT blend thin film measured from different gate voltage (V_G = 0 to −80 V).

As shown in Figure 2.8c, pristine P3HT devices exhibit much higher drain currents with no applied gate voltage (V_G = 0 V), suggesting a significant parasitic bulk conductivity.[144] Horowitz et al.[146] revealed that this "ohmic" current behavior in pristine P3HT devices can be ascribed to p-doping of the mobile impurities in polythiophene, particularly since all device fabrication was carried out under ambient conditions. These mobile dopants are likely to migrate in the electric field, resulting in nonsaturated drain current. In contrast, the issues associated with p-doping were markedly diminished when 50% BTTT was incorporated into the P3HT thin film and afforded saturated output characteristics as shown in Figure 2.8d.

The device characterization results are consistent with UV−vis and XRD demonstrating increased molecular ordering upon incorporation of the crystalline oligomer BTTT into P3HT thin films leading to more effective charge carrier transport pathways. Also, because a larger fraction of oxygen sensitive P3HT was substituted with the air-stable crystalline oligomers having relatively deep highest occupied molecular orbitals (HOMO), the blend thin films acquired greater resistance against oxidative doping, resulting in a substantial decrease in V_{Th} and increase in I_{ON}/I_{OFF}.

In order to further confirm the above assumption, the intrinsic work function (∅) and IP of the parent semiconductors and their respective blends were determined by ultraviolet photoelectron spectroscopy (UPS). The UPS spectra and corresponding IP for the blend thin films are provided in Figure 2.9 and 2.10, respectively. The pristine P3HT thin film exhibited a relatively low IP at 4.57 $\pm$ 0.07 eV, in agreement with previously reported results.[147, 148] In contrast, the IP for BTTT is at about 5.20 $\pm$ 0.02 eV,

approximately 0.6 eV higher than the conjugated polymer, suggesting greater environmental stability. For the blends, the UPS spectra for the onset of the secondary electron cut off energy, shift to a lower binding energy as the BTTT weight ratio increased (Figure 2.9a). This shift is indicative of a deeper HOMO energy level and concomitant reduction in the impact of unintentional oxidative doping, which could severely deteriorate device charge transport performance.

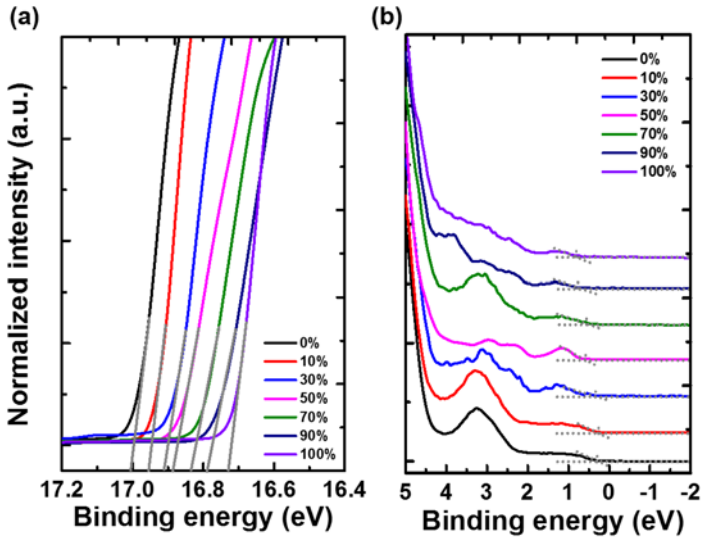

Figure 2.9 UPS spectra of (a) high binding energy cutoff and (b) lowest binding energy point of P3HT:BTTT blend thin-films.

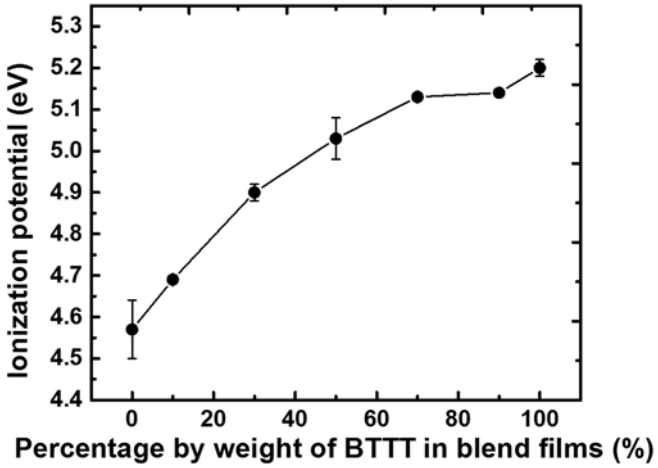

Figure 2.10 Ionization potential of P3HT:BTTT blend thin films as a function of the weight percentage of BTTT with respect to P3HT in the blend films.

Device performance peaks at a 1:1 blend ratio, followed by an abrupt decrease in thin-film mobility upon further increases in the fraction of BTTT. From XRD analysis, the highest crystallinity of the blend thin films was observed when the oligomer concentration exceeded 90%. Nevertheless, the 90% blend exhibited inferior charge transport performance, and no macroscopic mobility could be measured from solution processed, pristine BTTT thin films. Zheng et al.[125] demonstrated that a pristine BTTT thin film exhibits charge transport properties when the high boiling point solvent, chlorobenzene (b.p. = 131 °C) was used for device fabrication. However, the mobility was limited by rapid solvent evaporation during solution processing. The deterioration of OFET performance when the oligomer became the majority component of the blend thin film will be further discussed in section 2.3.5.

Figure 2.11 shows the transfer curve of pristine P3HT OFET devices fabricated under ambient and nitrogen conditions and 50% P3HT:BTTT blend OFET devices fabricated under ambient condition. In comparison to pristine P3HT OFET devices fabricated under ambient condition, V_{Th} and off-state current can be decreased when the pristine P3HT OFET devices were fabricated in a nitrogen glovebox with strictly controlled moisture and oxygen content (H_2O < 0.5 ppm, O_2 < 0.5 ppm). However, the 50% P3HT:BTTT blend OFET devices fabricated under ambient condition not only significantly diminish the p-doping effect but also provide higher field-effect mobility.

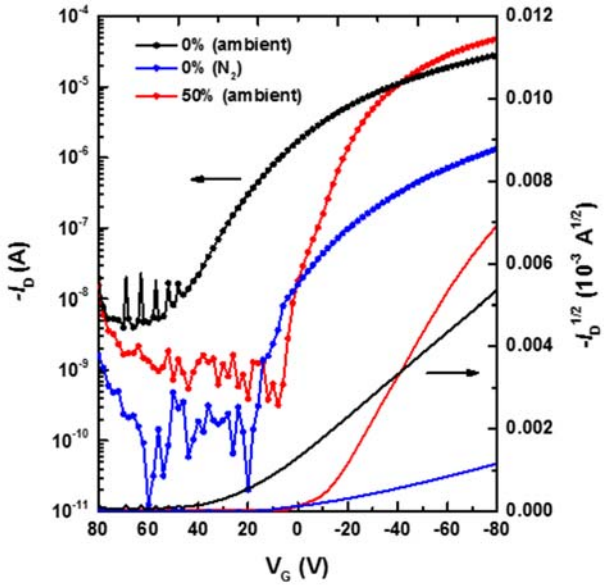

Figure 2.11 Transfer characteristics of pristine P3HT (fabricated under ambient and nitrogen conditions) and 50% P3HT:BTTT blend OFET devices (fabricated under ambient condition). (V_D = −80 V)

2.3.5 Mechanistic Interpretations

Figure 2.12 presents a schematic illustration of the evolution of thin-film morphology for P3HT:BTTT blends as the oligomer weight ratio increases. UV−vis, XRD, and AFM results suggest that the molecular ordering of a pristine P3HT thin film is inhibited by intrinsic polymer properties such as long-chain entanglement during the kinetically limited spin coating process which results in poor charge transport performance. As an appropriate amount of BTTT is incorporated into the P3HT thin films, island-like crystal domains appear, and are embedded in an amorphous matrix. Meanwhile, the long polymer chains can serve as interconnection pathways between crystalline domains, which are isolated by disordered regions. The interconnecting

polymer chains minimize the possibility that charge carriers will be trapped at grain boundaries. Above the optimum blend ratio, further increase in the proportion of BTTT leads to a negative impact on charge transport. The deterioration in semiconducting performance can be ascribed to two root causes. First, as observed from the AFM images (Figure 2.6), there are a relatively large number of grain boundaries present in thin films prepared with a high proportion of BTTT. Kelley et al.[34] demonstrated that the presence of grain boundaries produce an energy barrier and increase contact resistance, hence preventing effective charge transport between grains. Second, P3HT polymer chains, which can bridge and connect the large crystal domains are absent in the high oligomer concentration thin films, thereby severely limiting the formation of charge percolation paths between crystals. These results confirm that crystallinity is, in and of itself, insufficient for effective macroscopic organic/polymer charge carrier transport performance, and increased connectivity between the crystalline domains must also be considered.[31, 89]

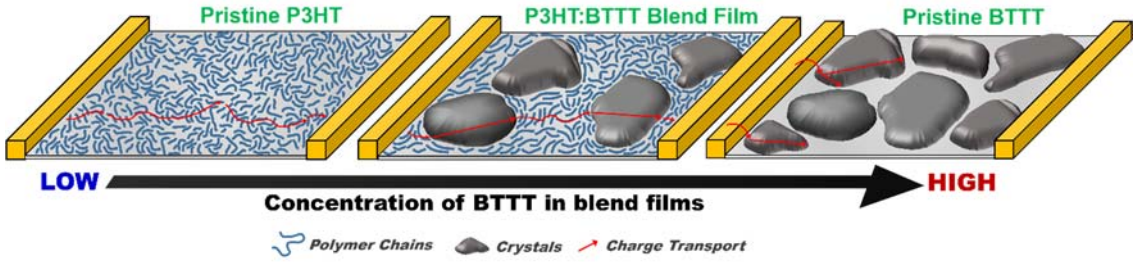

Figure 2.12 Schematic illustration of the morphology evolution of P3HT:BTTT blend thin films as a function of the BTTT concentration.

2.4 Conclusions

In conclusion, the overall macroscopic charge carrier transport performance of a representative solution processable, polymer semiconductor, P3HT, was significantly improved through a blend approach where the oligomer BTTT was incorporated into the polymer thin films. The surface morphology and thin film crystallinity was tunable by varying the weight fraction of oligomer. The macroscopic charge carrier transport properties, as determined by OFET performance, were optimum at a 1:1 blend ratio because of synergistic effects in the two-component system. The incorporation of the crystalline oligomer into P3HT is favorable for the formation of supramolecular ordered morphologies during the rapid thin-film formation process. Meanwhile, the presence of the long chain polymer appears to reduce the negative impact of grain boundaries between small crystalline domains, leading to more effective charge hopping between transport sites. Furthermore, the remarkable decrease in V_{Th} in the absence of surface treatment or annealing steps underscores the advantages of this approach for low-cost, large area, flexible electronics fabrication.

CHAPTER 3. TOWARD PRECISION CONTROL OF NANOFIBER ORIENTATION IN CONJUGATED POLYMER THIN FILMS: IMPACT ON CHARGE TRANSPORT

3.1 Introduction

As we presented in the Chapter 2, OSCs typically exhibit a semicrystalline thin film structure, with macroscopic charge transport properties that represent some combination of transport through highly conductive crystalline regions and poorly conductive amorphous domains.[150-152] Therefore, controlling the structure and morphology of the semiconducting layer is essential to improve the charge carrier mobility and overall device performance. Moreover, it has been shown that charge transport within OSCs is highly anisotropic.[2, 70] In the case of P3HT, the charge carrier mobility along the conjugated polymer backbone is significantly higher than in the direction of insulating alkyl side chains.[33] Accordingly, the long-range alignment of OSCs is beneficial for efficient charge transport when the crystallographic direction of the thin films is oriented along the active channel of electronic devices. For example, out-of-plane alignment of polymer chains is desired for fast vertical charge transport in OPVs[134] and OLEDs.[153] On the other hand, the in-plane direction is the major charge transport pathway for thin film transistors.[2]

To obtain long-range aligned thin-film structures, several methods have been proposed, including evaporation-induced self-assembly,[154, 155] epitaxial crystallization,[156, 157] nanoimprint lithography,[75, 134, 158] electrospinning,[159] mechanical stretching,[160, 161] and

high-temperature rubbing.[162-165] Although these approaches are able to precisely control the orientation of crystalline structures, leading to charge transport and optical anisotropy, some serious problems still exist. For instance, the improvement of device performance obtained from strained or rubbed thin films is very limited because some proportion of crystal planes still adopt a face-on orientation, which is not favorable for effective in-plane charge transport.[160, 165] For directional solidification, mass transport limitations during the solvent evaporation process may lead to sharp grain boundaries and void formation, which will become charge carrier traps and thus hinder transport.[32] Most of all, the above-mentioned methods are difficult and costly to implement on an industrial-scale and with continuous device production.

Meniscus-guided coating techniques such as zone casting, blade coating, and solution shearing are alternative, simple, and scalable strategies to induce long-range ordering and well aligned thin-film structures.[166] For example, Park et al.[167] suggested that the combination of differential substrate surface energy and solution shearing can generate highly oriented and precisely self-registered crystalline structures within the active channel, affording low device-to-device variability. Alternatively, Diao et al.[168] showed that shear coating with a micropillar-pattered printing blade can facilitate the formation of well aligned small molecule crystals. These reported solution coating methods, however, still relied on complex equipment and/or experimental procedures such as prepatterned substrates or microstructured coating blades.[169-172] In addition, most investigations focused on the fabrication of anisotropic crystalline conjugated small molecule assemblies.[167-169, 173-175] To date, only a few studies have discussed the alignment of semiconducting polymers via unidirectional solution-coating techniques,

which would be compatible with roll-to-roll printing processes. For example, the McCulloch research group[176] demonstrated a flow-coating process that is able to control the crystal orientation of poly(2,5-bis(3-alkylthiophen-2-yl)thieno[3,2-b]thiophene) (pBTTT). However, this approach required relatively high processing temperatures to induce the phase transition and thereby form a well-oriented terraced ribbon structure. Recently, Bao and co-workers[170] introduced a flow-enhanced solution printing method to increase polymer crystallinity, which is facilitated by prestretched polymer chains through extensional flow. However, a micropillar-patterned printing blade was required.

The difficulties associated with chain alignment are especially true for high-MW conjugated polymers, which generally exhibit greater charge-carrier mobility than their low molecular weight counterparts.[89, 90] One reason for this is the difficulty associated with nucleation and growth of self-assembled conjugated polymers due to chain-entanglement effects that can severely hinder the alignment and π–π stacking of polymer chains during rapid solvent evaporation associated with solution-coating methods.[36, 91, 177]

Here, we demonstrate a blade-coating approach to induce long-range alignment of conjugated polymer nanocrystalline structures by preprocessing the polymer solution with low-dose ultraviolet (UV) irradiation and solution aging. The demonstration vehicle was P3HT. It has been reported that the low dose UV-irradiation is able to induce solution-phase P3HT aggregation into nanofibrillar structures via a shift in the overall balance between "aromatic-" and "quinoidal-like" configurations (as shown in Figure 3.2a). The latter polymer conformation exhibits a higher degree of backbone coplanarity and thus facilitates the π–π interchain interactions necessary for nanofiber formation.[112] However, the development of UV-irradiated aggregation becomes saturated after ~8 min

UV-irradiation time. Fortunately, further P3HT aggregation can be driven by time-dependent self-assembly.[111] As a result, the population of P3HT nanofibrils can be controlled and enhanced by simply storing the UV-irradiated P3HT solutions under ambient conditions for the designated period of time in a so-called solution-aging approach.

This combined approach takes advantage of the facile and straightforward solution preprocessing steps that were found to effectively facilitate the controlled nucleation and crystal growth of conjugated polymers prior to the rapid thin-film formation process.[40, 178] Interrogation of the resultant thin films revealed that the degree of crystallinity and chain alignment were both significantly improved with increased solution-aging time, and the optical and charge transport properties were found to be anisotropic. Analysis of the surface morphology coupled with mechanistic interpretation supports the supposition that polymer chain-entanglement effects, which negatively impact polymer self-assembly and chain alignment, were greatly reduced when the semiconducting films were fabricated by blade-coating preaggregated polymer solutions. The anisotropic charge-carrier mobility of uniaxially aligned nanofiber arrays further suggests that interfiber tie chains facilitate the alignment of nanoaggregates and provide for efficient charge transport pathways between nanofibrillar structures.

3.2 Experimental Methods

3.2.1 Materials

Regioregular P3HT (MW: 90 kD, Regioregularity: 96%) and chloroform (anhydrous) were purchased from Rieke Metals Inc. and Sigma-Aldrich, respectively, and used without further purification.

3.2.2 Solution Processing of P3HT

A combination of UV-irradiation and solution aging was used to control the aggregation of P3HT in solution state. First, 10 mg of P3HT was dissolved in 2 mL of chloroform at 55 °C under stirring for 30 min. After complete dissolution of P3HT, the solution was left to cool to room temperature. Then, the vial containing the solution was placed on a hand-held UV lamp (Entela UVGL-15, 5 mW cm^{-2}, 254 nm), which had been placed on a magnetic stirrer (Corning Inc.), and the solution was then stirred at 300 rpm. The UV-irradiation time was fixed at 8 min, and the solution exhibited a notable color change from bright orange to dark purple/brown, indicating that the P3HT began to aggregate and form nanofibrillar structures in the solution. The UV− P3HT solutions were then stored for a designated period of time (0, 3, 8, 15, 24 h). The vials containing the solution were covered with aluminum foil to avoid additional exposure to light. All solution processing was done in ambient condition.

3.2.3 OFET Fabrication and Characterization

The OFETs with a bottom-gate bottom-contact configuration were fabricated using a heavily n-doped silicon wafer as the gate electrode. A 300 nm thick layer of thermally

grown SiO_2 served as the gate dielectric. The 50 nm Au source and drain electrodes with 3 nm Cr as the adhesion layer were both deposited via standard photolithography based lift-off processing, followed by E-beam evaporation onto the SiO_2 layer. Before the semiconducting layer deposition, the device substrates were cleaned in an ultrasound cleaning bath and sequentially rinsed with acetone, methanol, and isopropanol. At the final step of the cleaning process, the devices were exposed to UV-ozone (Novascan PSD-UV) to ensure complete removal of residual photoresist and other organic contaminants. OFET fabrication was completed by depositing the preprocessed P3HT solutions onto the precleaned substrates via either spin coating (WS-650MZ-23NPP, Laurell) at a spin speed of 1500 rpm for 60 s or blade coating at an optimized coating speed.

For the blade coating system, the coating blade was vertical to the substrate at a fixed gap of 10 μm. The device substrate was placed onto a homemade vacuum chuck equipped with a motorized linear stage (A-LSQ150AE01, Zaber). According to different blade coating speeds, the thin film deposition can be divided into two regimes: evaporation and Landau-Levich regime.[179, 180] In evaporation regime, the time scale of solvent evaporation is similar to the solid film formation due to the relatively low blade coating speed. In this work, the film deposition was controlled within this regime (fixed coating speed at 3 mm s^{-1}), which is also known as "convective assembly" regime. Accordingly, the concentration gradient of the polymer solution that arises from solvent evaporation will force migration of polymer chains toward the solution meniscus, leaving behind a highly aligned nanofibrillar thin film structure. It is worth noting that the nanofibrillar structure is difficult to be well-aligned at very low coating speed (0.5 mm s^{-}

[1]) since most of the solvent were evaporated before the blade was passed through a solution reservoir.

In contrast, a higher blade coating speed leads the thin film deposition to Landau-Levich regime, which is similar to drop casting since a liquid film is first dragged out via viscous forces and dries afterward. Thus, the thin film structure and morphology is mainly controlled by the wet film drying process instead of convective assembly observed in evaporation regime. As shown in Figure 3.1, the resultant films obtained from higher blade coating speeds (> 10 mm s^{-1}) revealed a weak oriented nanofibrillar structure.

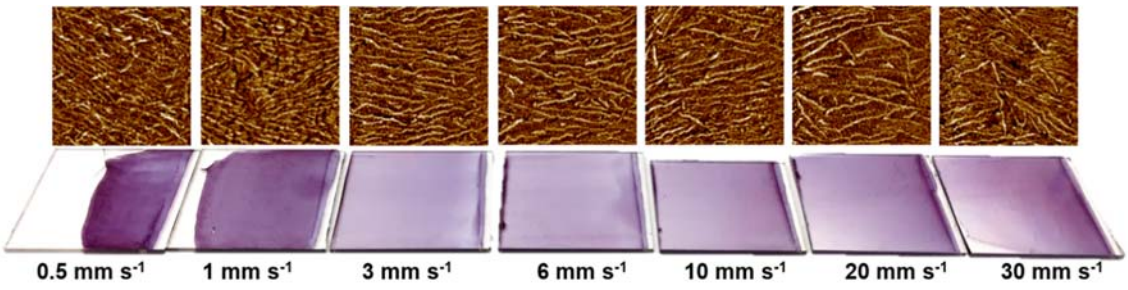

Figure 3.1 AFM phase images (2 × 2 μm) and corresponding photo images obtained by blade coating 24 h aged UV-irradiated P3HT solutions with various of coating speeds.

OFET electrical properties were investigated in a nitrogen glovebox and using an Agilent 4155c semiconductor parameter analyzer. The charge-carrier mobilities were calculated in the saturation regime from the transfer plots of drain current (I_D) versus gate voltage (V_G) using the following Equation 3.1:

$$I_D = \frac{W}{2L} C_i \mu (V_G - V_{Th})^2 \tag{3.1}$$

where W and L refer to channel width (50 μm) and length (2000 μm), respectively. μ presents the hole mobility, V_{Th} is the threshold voltage, and C_i is the capacitance per unit area of the SiO_2 gate dielectric (1.15×10^{-8} F cm^{-2}).

3.2.4 UV−vis Spectroscopy

The solution and solid-state UV−vis spectra were determined using an Agilent HP 8510 UV−vis spectrophotometer. The corresponding P3HT films were deposited onto precleaned glass slides, which had undergone the same clean procedure as indicated above for OFET devices. This spectrophotometer was also used for polarized UV−vis absorption measurements by polarizing the incident light vertical or perpendicular to the blade coating direction.

3.2.5 Atomic Force Microscopy (AFM).

The surface morphologies of the thin films were characterized by AFM using a Bruker Dimension Icon atomic force microscopy system, operating in tapping mode with a n-type silicon tips (HQ:NSC14, MikroMasch).

3.2.6 Polarized Optical Microscopy (POM).

POM images were obtained using a Leica DMRX optical microscope equipped with a rotatable polarizer, analyzer, and Nikon D300 digital SLR camera.

3.2.7 Grazing-Incidence Wide-Angle X-ray Scattering (GIWAXS).

The GIWAXS measurements were carried out on beamline 11−3 at the Stanford synchrotron radiation light source (SSRL) with the help of Dr. Chris Tassone. The beam

was kept at an energy of 12.7 keV and the critical angle of measurement was 0.13°. A LaB6 standard sample was used to calibrate the instrument, and the software WxDiff was used to reduce the 2D scattering data into the corrected 1D integration plots.

3.3 Results and Discussions

3.3.1 Photophysical Properties

Figure 3.2a depicts the experimental polymer solution preprocessing and thin-film formation sequence. The P3HT solutions were prepared in $CHCl_3$ at a concentration of 5 mg mL^{-1}, and they were treated with low dose UV-irradiation. Next, the UV-irradiated P3HT (UV-P3HT) solutions were aged for a designated period of time (0, 3, 8, 15, 24 h) under ambient conditions in the dark. As shown in Figure 3.2b, the UV−vis spectrum obtained from pristine P3HT solutions exhibited a single absorption maximum at ca. 453 nm, and no distinct spectral features were observed. Upon UV-irradiation, the orange polymer solutions turned to dark purple/brown, and absorption bands at ca. 550 nm and ca. 605 nm associated with intrachain (0−1) and interchain (0−0) vibronic transitions, respectively, began to develop. These spectral features are indicative of P3HT aggregate formation.[129] With aging, the intensity of the low-energy absorption bands notably increased in a time-dependent manner, suggesting that the polymer aggregates further evolved into longer nanofibrillar structures. The degree of polymer aggregation in solution as a function of aging time was estimated from Franck−Condon fits to the absorption spectra, as shown in Figures 3.2c and 3.3.[87, 177] The raw UV-vis absorbance

measurements were fit to a Frank−Condon progression assuming a Gaussian line shape according to the following Equation 3.2:[132, 181, 182]

$$A(E) \propto \sum_{m=0} \left(\frac{S^m}{m!}\right)\left(1 - \frac{We^{-S}}{2E_p}\sum_{n\neq m}\frac{S^n}{n!\,n-m}\right)^2 \exp\left(\frac{\left(E - E_{0-0} - mE_p - \frac{1}{2}WS^m e^{-S}\right)^2}{2\sigma^2}\right) \quad (3.2)$$

where W is the exciton bandwidth, $E_{0\text{-}0}$ is the 0-0 transition energy, σ is the Gaussian linewidth, m is the number of vibrational transitions, n is the number of chromophores, S is the Huang-Rhys factor (fixed to 1), and E_p is the effective energy of the vinyl stretch mode (fixed to 0.179 eV). In this framework, W, $E_{0\text{-}0}$, σ, and a proportionally constant, k, are free parameters. In order to analyze the aggregate contributions to the spectrum, the above equation was fitted to the low-energy part of the spectrum that contained the 0-0 and 0-1 absorption peaks. The upper and lower wavelength bounds for the fit were varied until the sum of squared errors was minimized. The non-linear least squares problem was implemented in MATLAB using *lsqcurvefit*. The ratio of the area under the aggregate fit to the total area under the absorbance curve gives the aggregate fraction. The percentage of P3HT aggregates increased gradually from 9.0 to 20.4% through 24 h of aging. The spectroscopic results are indicative of a time-dependent polymer self-assembly process that is driven by interchain interactions.

Figure 3.2d and e present the absorption spectra of pristine and processed P3HT thin films deposited by spin coating and blade coating, respectively. A red-shift of the π−π* intraband transition and increased intensity of the (0−0) absorption peak at ca. 605 nm were observed from both spin coated and blade coated thin films, and the evolution of polymer aggregation appeared consistent with the solution-phase UV−vis spectral results.

Given that the band intensities increased irrespective of coating method, it is likely that the nanofibers formed in solution and survived the thin-film fabrication process.[128, 183] According to Spano's model, the intensity ratio of the (0−0) and (0−1) vibronic bands can be related to the free exciton bandwidth (W), which enables estimation of the magnitude of interchain coupling within aggregates.[133, 149] A decrease in W is associated with increased conjugation length and/or improved chain ordering. The values of W were calculated by the following Equation 3.3:[132]

$$\frac{I_{0-0}}{I_{0-1}} \approx \left(\frac{1 - 0.24W/E_p}{1 + 0.073W/E_p} \right)^2 \tag{3.3}$$

where I_{0-0} and I_{0-1} represent the intensities of the 0−0 and 0−1 vibronic bands, respectively, obtained from Gaussian fits to the experimental spectra (Figure 3.4 and 3.5). E_p is the vibrational energy of the symmetric vinyl stretch (taken as 0.18 eV).[133] Figure 3.2f provides the calculated free exciton bandwidths for corresponding thin films. The value of W decreased approximately linearly with longer aging time, regardless of the film formation process. Notably, the blade coated samples exhibited lower exciton bandwidth values compared with spin coated analogues, suggesting that the blade-coating approach more effectively extended and coplanarized the polymer chains thereby promoting intermolecular ordering.

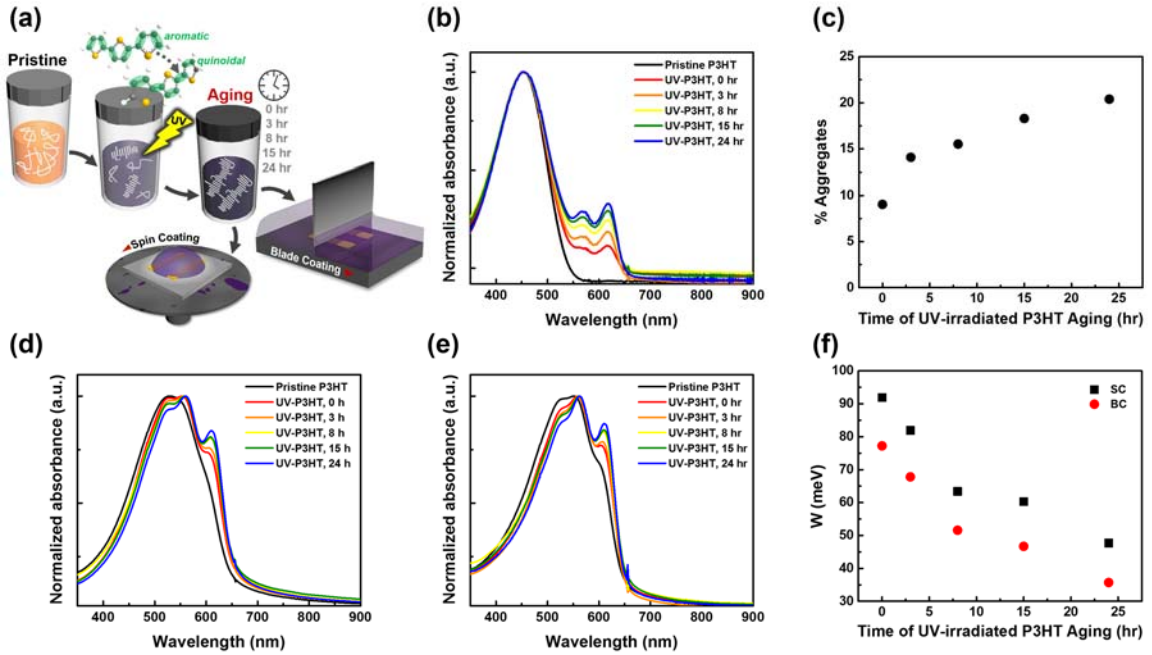

Figure 3.2 (a) Schematic illustration of polymer solution preprocessing and thin-film formation experimental sequence. (b) Normalized UV−vis absorption spectra of pristine and UV−P3HT in solution state with varying solution-aging time. (c) Percentage of UV−P3HT aggregates as a function of solution-aging time in solution. Normalized UV−vis absorption spectra of pristine and aged UV−P3HT thin films deposited by (d) spin coating and (e) blade coating. (f) Evolution of exciton bandwidth (W) as a function of solution-aging time.

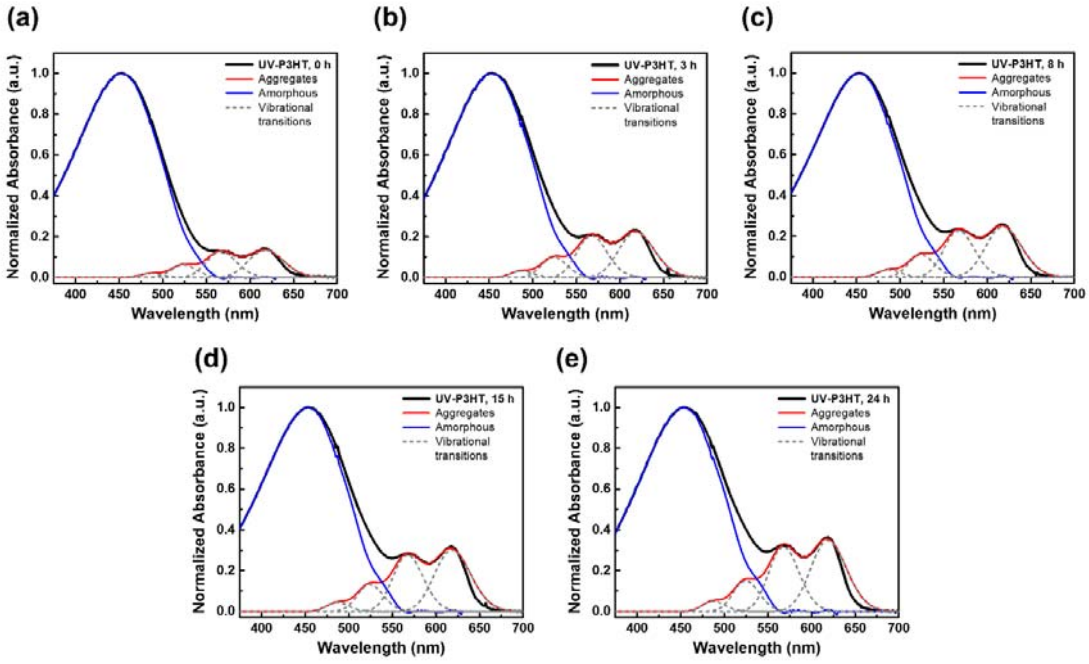

Figure 3.3 Normalized absorption spectra of UV-irradiated P3HT solutions with different solution aging time (a) 0 h, (b) 3h, (c) 8 h, (d) 15 h, (e) 24 h. The black lines ae experimental absorption spectra. The aggregate absorbance (red line) were obtained from the Franck-Condon fits. The amorphous absorbance (blue line) is the difference between the total spectra and the fit of aggregate absorbance. The individual vibrational transitions in the aggregate absorption region are also provided.

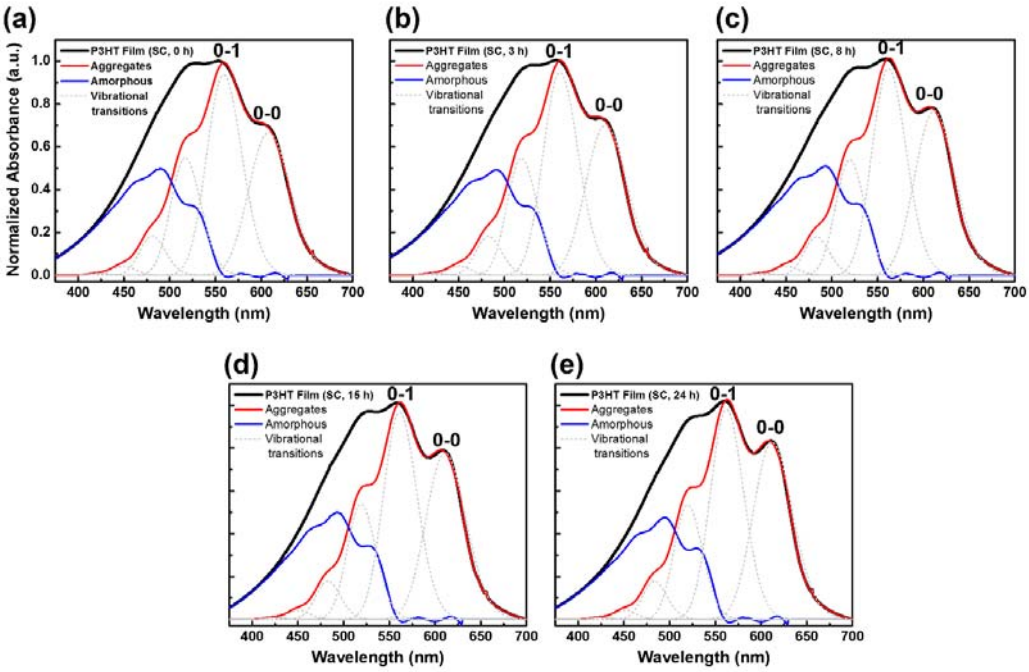

Figure 3.4 Normalized absorption spectra of UV-irradiated P3HT spin coated films with different solution aging time (a) 0 h, (b) 3h, (c) 8 h, (d) 15 h, (e) 24 h.

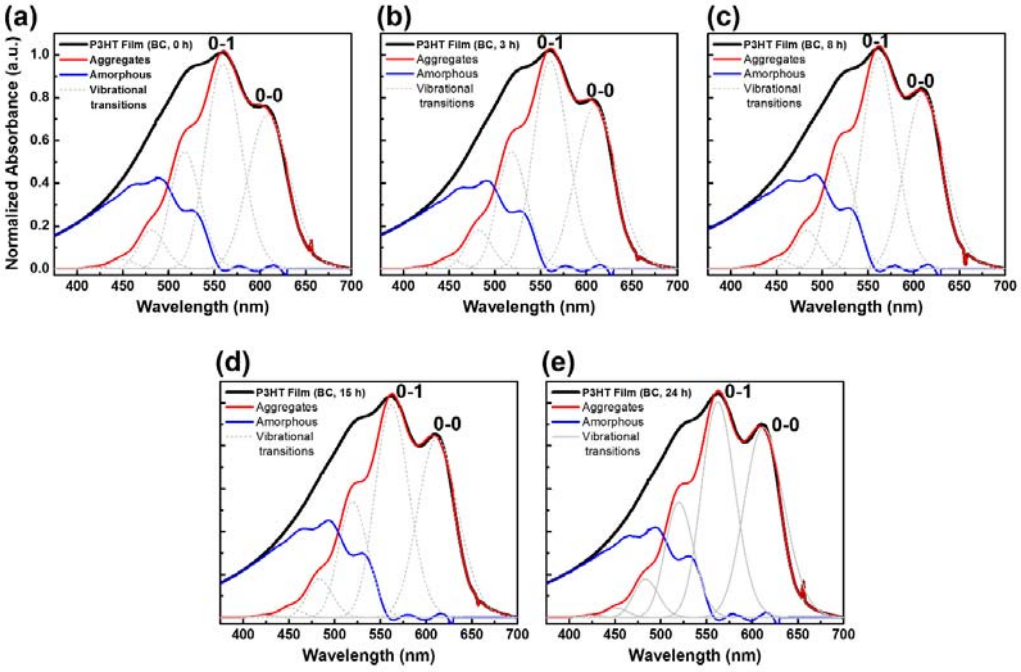

Figure 3.5 Normalized absorption spectra of UV-irradiated P3HT blade coated films with different solution aging time (a) 0 h, (b) 3h, (c) 8 h, (d) 15 h, (e) 24 h.

3.3.2 Surface Morphology

Based on examination of the photophysical properties, the level of solution state polymer aggregation was successfully manipulated by the combined UV-irradiation/ aging method. The impact of solution preprocessing on the surface morphologies of blade coated thin films as a function of aging time was evaluated using atomic force microscopy (AFM) imaging. As shown in Figure 3.6a, pre-deposition processing with just UV-irradiation led to the development of randomly oriented, nanoscale fibrillar structures that were isolated by disordered regions. With increased solution-aging time, the average nanofiber length and density increased significantly. In addition, P3HT nanofiber orientation became more unidirectional. (Figure 3.6b-e).

As shown in Figure 3.6f–j, the AFM phase images were analyzed for their nanofiber orientation distribution and degree of nanofiber alignment using an open-source image processing algorithm.[184] According to the polar figure (Figure 3.6k), which is generated by counting the number of fiber backbone pixels of each orientation, the fiber orientation distribution of aged UV−P3HT thin films was mainly oriented along the horizontal axis, which corresponded to the blade coating direction. The nanofiber alignment was further quantified by the orientational order parameter (S_{2D}),[185, 186] which is defined for a population of oriented fiber segments (pixels) as follows in Equation 3.4:

$$S_{2D} = 2\cos^2\theta_n - 1 \tag{3.4}$$

where θ_n is the angle between a fiber segment and the population's director, $\vec{n}$, which is chosen as the average orientation of the populations; for completely aligned nanofibrillar structures S_{2D} = 1, whereas for totally randomly oriented thin films S_{2D} = 0. S_{2D} can be

correlated to the degree of nanofiber alignment, as plotted against aging time in Figure 3.6l. The films blade coated with fresh (0 h) UV−P3HT solutions provide an S_{2D} value of 0.53, showing a weakly oriented microstructure. However, this value gradually increased with longer solution-aging times and reached a highest value of S_{2D} at 0.89 for an aging time of 24 h, suggesting a highly aligned nanofibrillar structure.

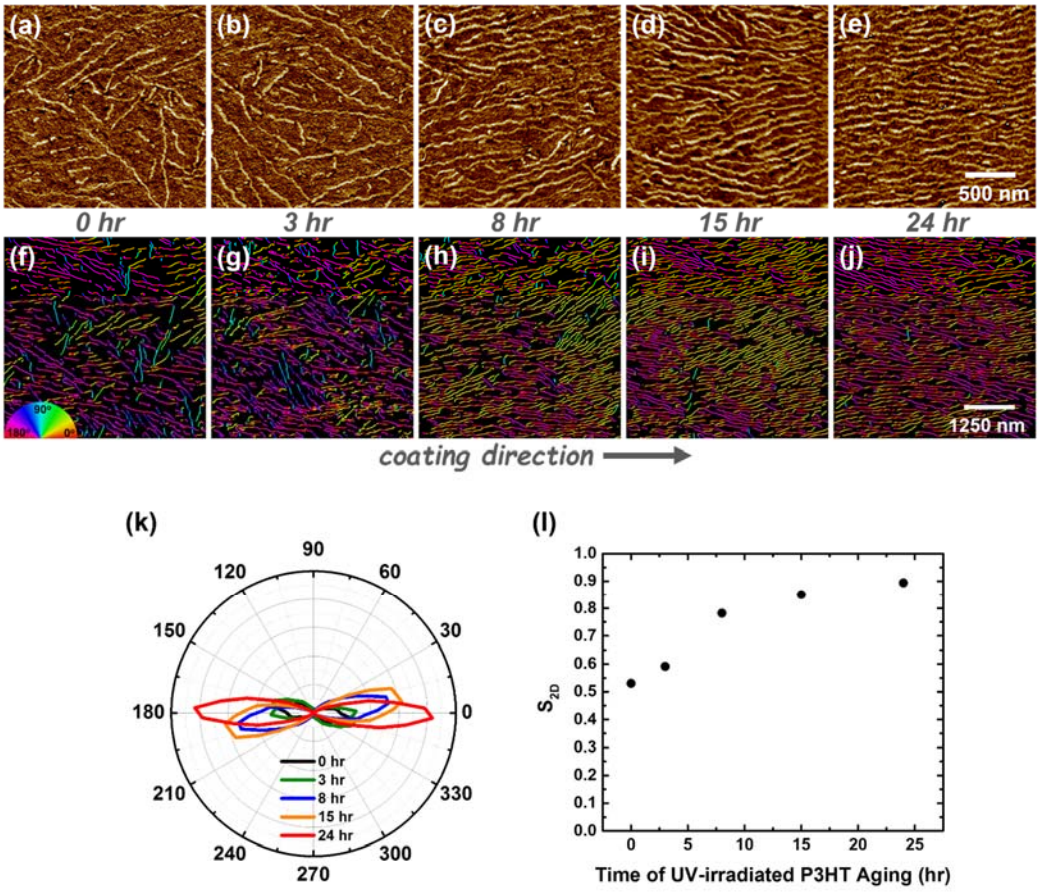

Figure 3.6 AFM phase images (2 × 2 μm) of P3HT films deposited by blade coating UV−P3HT solutions with (a) 0 h, (b) 3 h, (c) 8 h, (d) 15 h, and (e) 24 h solution-aging time. Image analysis (5 × 5 μm) of P3HT films deposited by blade coating UV−P3HT solutions with (f) 0 h, (g) 3 h, (h) 8 h, (i) 15 h, and (h) 24 h solution-aging time. (k) Polar plots and (l) S_{2D} of blade coated films as a function of solution-aging time.

The UV−P3HT solution with 24 h aging time was also deposited onto a substrate via spin coating. The spin-coated thin films showed a distinct surface morphology compared with blade coated samples as shown in Figure 3.7. In contrast to the long-range aligned nanocrystalline structure observed from blade coated samples, films deposited by spin coating the 24 h aged UV−P3HT solution exhibited randomly oriented P3HT nanofibrillar surface morphology, indicating that a unidirectional coating process is a prerequisite for aligning the conjugated polymer nanofibers along the coating direction.

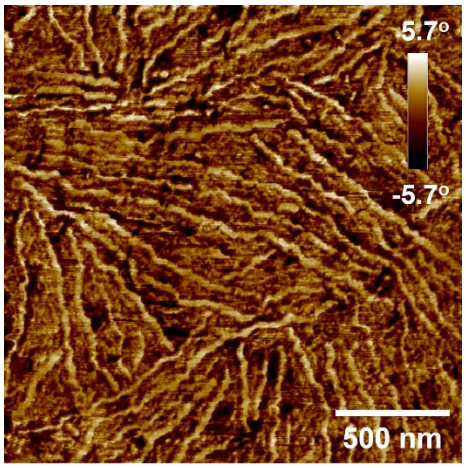

Figure 3.7 AFM phase images (2 × 2 μm) of P3HT thin films deposited by spin coating 24 h aged UV-irradiated P3HT solutions.

3.3.3 Optical Anisotropy

Cross-polarized optical microscopy (POM) was used to investigate the optical anisotropy of aged UV−P3HT thin films. As evidenced by POM (Figure 3.8), the fresh (aged 0 h) UV−P3HT blade coated thin film appeared completely dark when viewed through crossed polarizers regardless of angle, demonstrating isotropic characteristics.

Alternatively, films obtained by blade coating aged UV−P3HT solutions exhibited clear birefringence, and the brightness concomitantly appeared to be enhanced with longer solution aging time. The almost complete extinction and re-emergence of brightness upon rotation of the thin-film long axis from 0 to 45° with respect to the crossed polarizers suggests a highly anisotropic crystalline structure.[187, 188] The POM results are well correlated with AFM images that showed well-aligned nanofibrillar surface morphologies. It is worth noting that the POM image area is 1000 times larger than that of the AFM images (2 × 2 μm), pointing to macroscopically aligned nanofibrillar structures. The spin coated thin films were also investigated with POM.

The extent of polymer chain alignment can be further evaluated through polarized UV−vis spectroscopy. For spin coated samples, 24 h aged UV−P3HT thin films exhibited no differences with respect to polarization direction owing to their isotropic nature (Figure 3.9a). The 24 h aged UV−P3HT films fabricated by blade coating showed distinct polarized UV−vis spectra as shown in Figure 3.9b. As anticipated, the anisotropic thin films exhibited a stronger absorbance when the polarized light beam was parallel to the aligned polymer chains; note that the transition dipole moment is typically along the long axis of conjugated polymer backbones.[189, 190] As a result, the low-energy absorption peak (0−0) at ca. 605 nm was concomitantly enhanced when the UV−vis polarization was vertical to the coating direction. In contrast, the overall polarized optical absorbance, which is parallel to the blade coating direction was significantly reduced. The above features demonstrated that the polymer backbones associated with the 24 h aged UV−P3HT thin films fabricated via blade coating are closely packed and perpendicular to

the long axis of the nanofibers, which in turn are well-aligned along the blade coating direction as shown in Figure 3.9c.

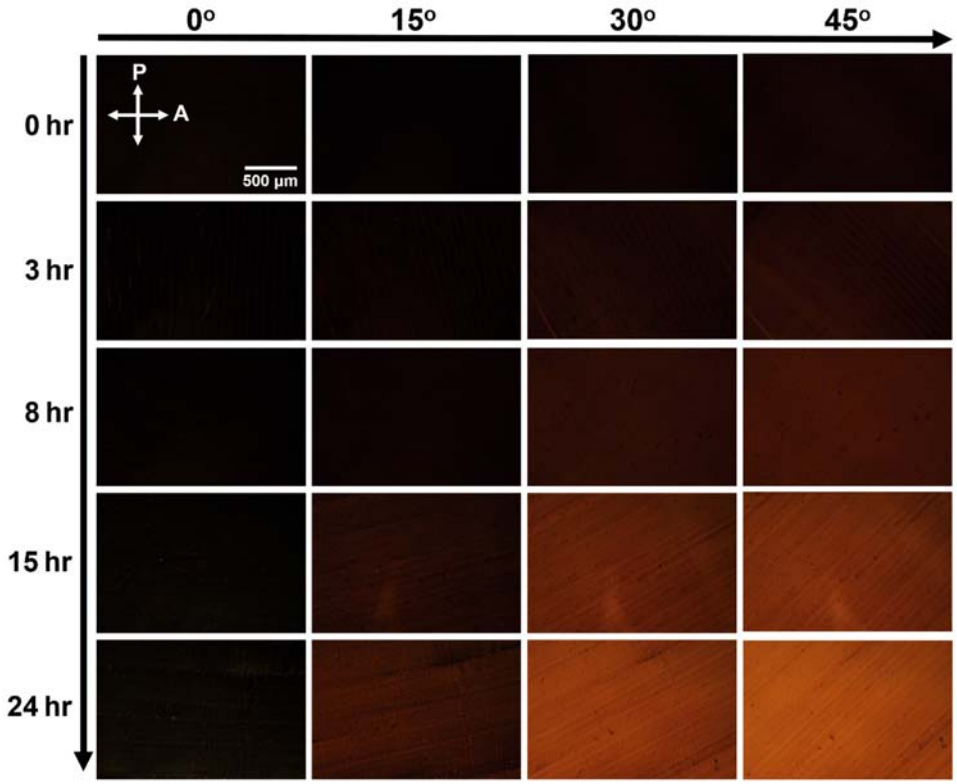

Figure 3.8 POM micrographs of blade-coated P3HT films with varying solution-aging time, rotated in increments of 15° between crossed polarizers.

To quantitatively analyze the structural anisotropy as a function of solution-aging time, the dichroic ratio ($R = A_{\perp} / A_{\parallel}$),[160] defined as the absorption of (0−0) peak obtained from polarized UV−vis spectra (Figure 3.10 and 3.11) in the direction perpendicular ($\perp$) to the absorption in the parallel direction ($\parallel$), was calculated. As shown in Figure 3.9d, the dichroic ratios of spin-coated thin films were ca. 1.0 and remained constant even with extended solution-aging time, providing additional support for the premise that spin coated thin films were randomly oriented. Alternatively, the dichroic ratio of blade coated

thin films increased linearly by 4 orders of magnitude as a function of solution-aging time, demonstrating that polymer chain alignment was improved and was easily tunable by varying the solution-aging time. These factors are further correlated with the degree of polymer aggregation in solution. It is worth noting that the rubbing P3HT films at high temperature can reach a dichroic ratio at 20, however, these films lack of long-range positional ordering, resulting in poor charge carrier mobilities.[165]

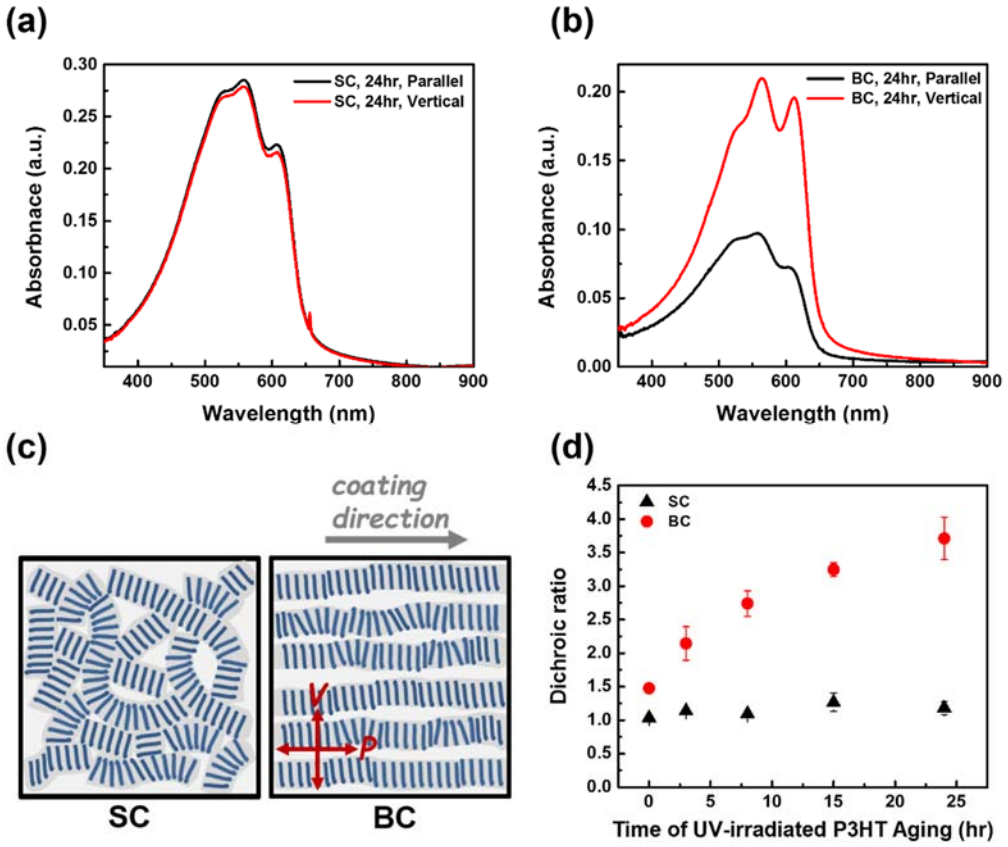

Figure 3.9 Polarized UV−vis spectra of 24 h aged UV−P3HT thin films deposited by (a) spin coating and (b) blade coating. (c) Schematic diagram of P3HT nanofibrillar structures in spin coated and blade coated thin films. The UV−vis polarization direction (red arrows) vertical (V) and parallel (P) to the blade coating direction are provided. The short blue lines schematically indicate the individual polymer chains, which are vertical to the long axis of nanofibers. (d) Evolution of the dichroic ratio as a function of solution-aging time.

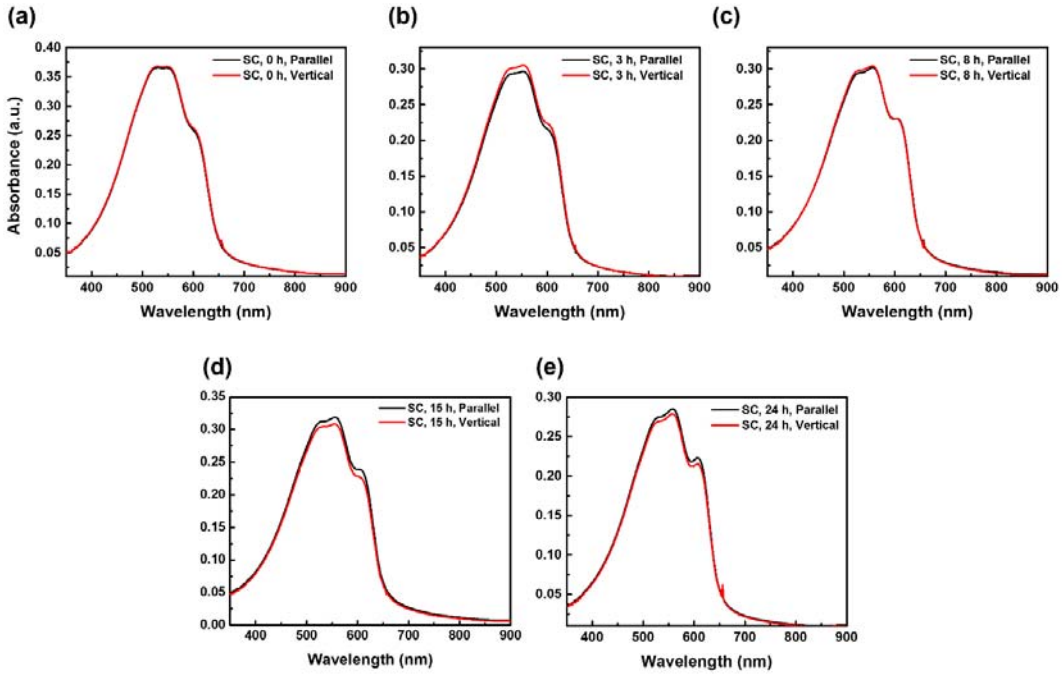

Figure 3.10 Polarized UV-vis spectra of spin coated films with (a) 0 h, (b) 3 h, (c) 8 h, (d) 15 h, (e) 24 h solution aging times.

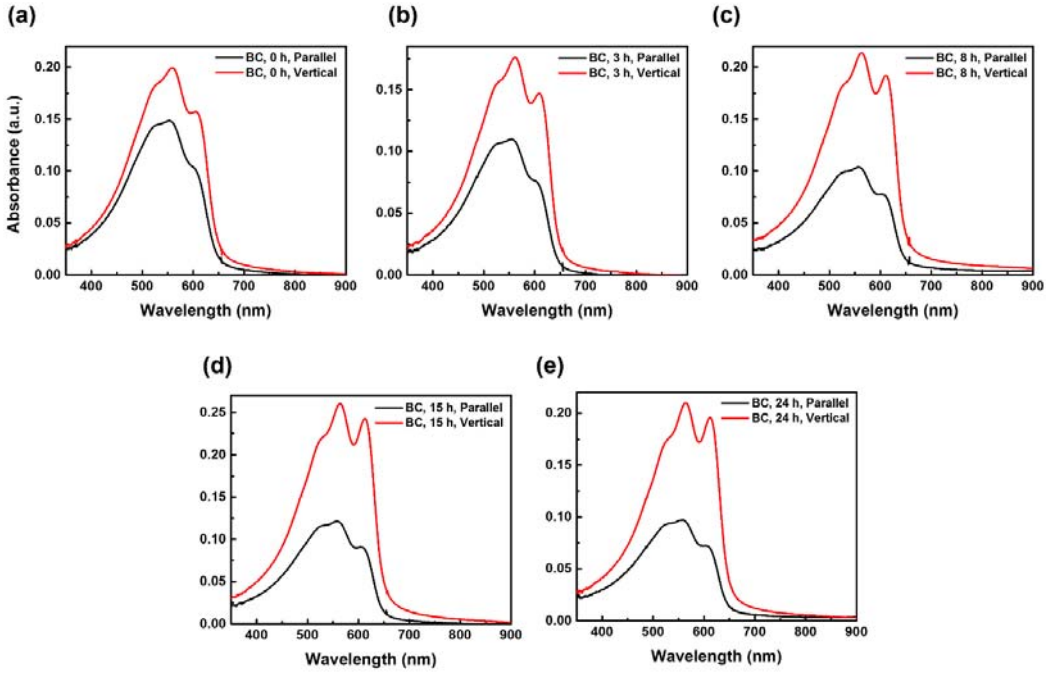

Figure 3.11 Polarized UV-vis spectra of blade coated films with (a) 0 h, (b) 3 h, (c) 8 h, (d) 15 h, (e) 24 h solution aging times.

3.3.4 Thin Film Crystallinity

To probe the thin-film crystallinity and microstructure, the 24 h-aged UV−P3HT thin films deposited by spin coating were investigated using two dimensional grazing-incidence wide-angle X-ray scattering (2D-GIWAXS), as shown in Figure 3.12a. The blade-coated thin films, which exhibited highly anisotropic microstructures, were measured in the two orientations where the blade-coating direction was parallel or vertical to the incident X-ray beam (Figure 3.12b and c). The 2D-GIWAXS profiles of these films present a series of intense characteristic (*h*00) (*h* = 1, 2, 3) reflection spots along the out-of-plane (q_z) direction, corresponding to lamellar stacking of P3HT oriented normal to the substrate.[74] The appearance of these high order reflections is a strong indicator of enhanced thin film crystallinity.[191] For the high q regime, the halo-like patterns that appeared along the azimuthal angle are attributed to the random oriented microstructures within the film.[192]

Figure 3.12d depicts the GIWAXS in-plane profiles for spin-coated and blade-coated thin films with the incident beam oriented parallel and perpendicular to the coating direction. A reflection peak at q = 0.379 ($Å^{-1}$) is evident in the in-plane scattering of the spin-coated sample, indicating that a certain portion of the polymer crystal planes lie parallel to the substrate.[74] Notably, this (100) in-plane diffraction peak, which is correlated with face-on crystal orientation was absent for blade coated thin films. Additionally, a sharp (010) peak was recorded at q = 1.649 ($Å^{-1}$) for the blade-coated sample when the incident X-ray beam was oriented vertical to the blade-coating direction. These results suggest strong π−π interchain stacking of polymer chains comprising the blade-coated sample and the crystalline microstructure of these films

exhibited a primarily edge-on orientation, expected to facilitate efficient charge transport in the plane of the substrate.[2] It has been reported that the characteristic π–π stacking peak would exhibit a maximum intensity when the X-ray incident beam is aligned along the polymer backbone as shown in Figure 3.12e.[179] Thus, the distinct intensity of (010) reflection peaks of blade coated thin films between the parallel and vertical directions provides further support that the polymer backbones are well-aligned and oriented perpendicular to the blade coating direction.

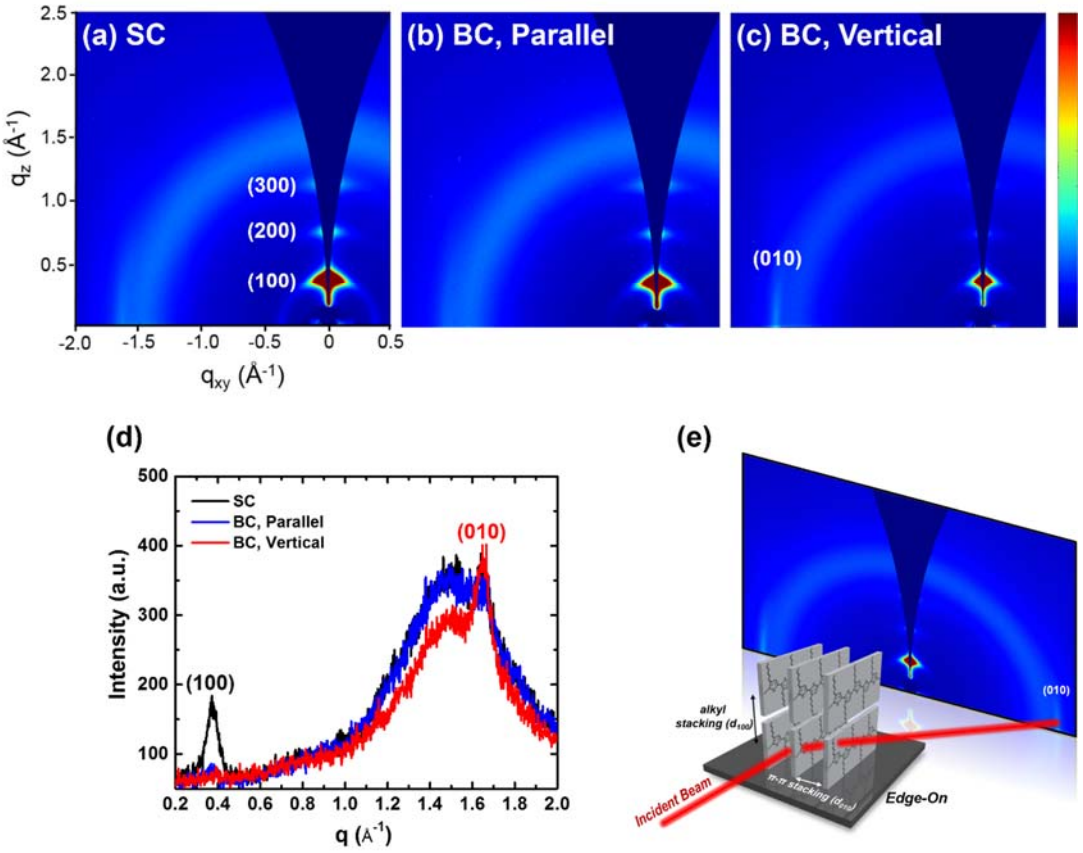

Figure 3.12 2D-GIWAXS of (a) spin coated and bladed coated films with the incident beam oriented (b) parallel and (c) vertical to the coating direction. (d) The GIWAXS in-plane profiles for spin coated and blade coated films with the incident beam oriented parallel and perpendicular to the coating direction. (e) Schematic illustration of in-plane (010) reflections when the incident beam is parallel to aligned polymer backbones.

3.3.5 Mechanistic Interpretations

In the blade coating process, the blade is used to drag the solution moving along one direction relative to the substrate at a controlled speed. The concentration gradient of the polymer solution that arises from solvent evaporation will force the migration of polymer chains toward the solution meniscus, leaving behind a uniform solid film. During thin film formation, polymer crystallization depends upon nucleation and crystal growth. Nucleation is the first step in the formation of polymer aggregates, which requires overcoming of a free-energy barrier and is intrinsically stochastic.[166] Subsequent crystal growth will be initiated from the available nucleation sites, leading to development of nanofibrillar structures.[193, 194] However, these self-assembly processes are time-dependent and typically require long periods of time to evolve and form an ordered thin-film structure.[195] As shown in Figure 3.13a, in pristine solutions, P3HT polymer chains behave as random coils, preventing the chains from stretching and packing into a well-ordered microstructure during a rapid solvent evaporation process, resulting in an amorphous thin film morphology.[40]

Low-dose UV-irradiation (Figure 3.14) was suggested to induce a higher degree of polymer backbone planarity, thereby facilitating π−π stacking necessary for nanofiber formation in the solution phase.[196] Although crystalline regions were obtained from blade coated fresh (aged 0 h) UV−P3HT solutions (Figure 3.13b), the population of aggregates was too low to form long-range ordered films due to the presence of significant numbers of solubilized polymer chains that still rely on the slow diffusion of polymer chains to the crystal growth front by π−π interchain interactions. Additionally, a certain degree of

flexibility and entanglement of unstacked polymer chains may inhibit chain alignment, especially for high-MW P3HT.

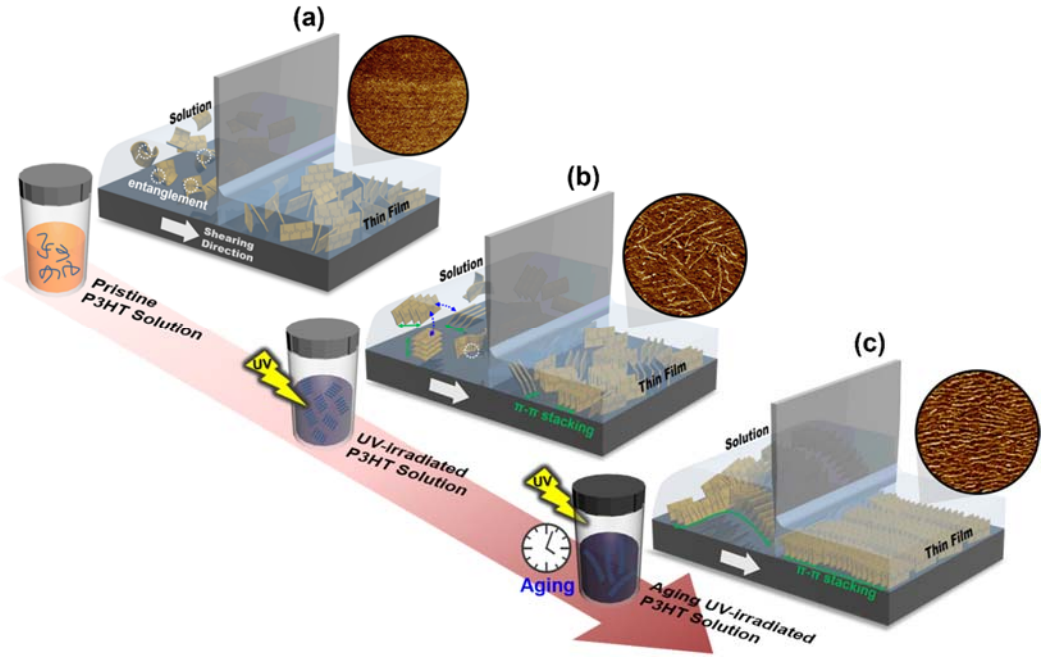

Figure 3.13 Schematic illustration of blade-coating process with (a) pristine P3HT (b) fresh UV−P3HT, and (c) aged UV−P3HT solutions.

The additional solution-aging step allowed for a further increase in the proportion of π−π stacked polymer chains in the solution state via time-dependent polymer self-assembly. Note that the level of aggregation is positively correlated with solution-aging time, confirmed by UV−vis analysis. As shown in Figure 3.13c, the high degree of polymer aggregation obtained by the synergistic combination of UV-irradiation and solution-aging effectively reduced the number of unstacked and tortuous polymer chains, which may cause severe chain entanglement effects.[36, 177] Moreover, interfiber connections, such as tie-chains, may further limit the freedom of nanofiber motions to a single direction upon blade coating the preaggregated polymer solutions,[91, 197, 198] thereby affording a long-range and highly aligned nanocrystalline structure.

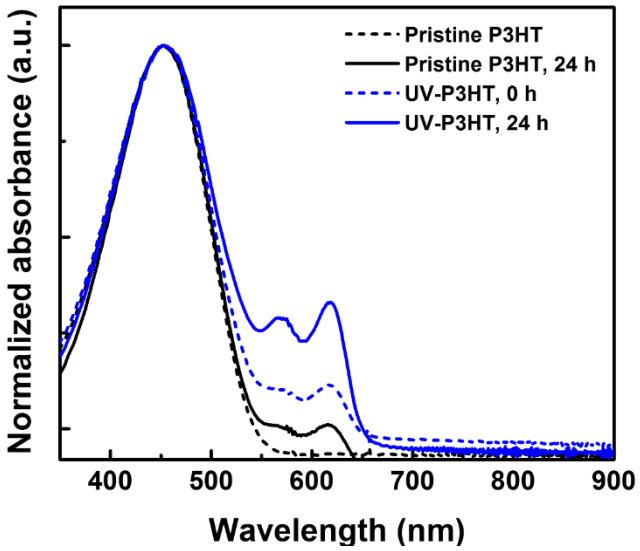

Figure 3.14 Normalized UV-vis absorption spectra of pristine and UV-irradiated P3HT solutions with 0 and 24 h solution aging time. The low energy absorption of UV-irradiated P3HT solutions were significantly higher than the peaks obtained from 0 and 24 h aged pristine P3HT solutions, suggesting that the UV-irradiation steps is able to promote the polymer aggregation process in the solution state.

3.3.6 Charge Transport Anisotropy

While previous studies focused on the alignment of individual polymer backbones along a certain direction,[159-165] the approach presented here effects long-range ordering of conjugated polymers into nanofibers and induces macroscopic alignment. Given the alignment of numerous well-packed and coplanarized conjugated polymer chains, the system presents an opportunity to study charge transport anisotropy in a highly aligned nanofibrillar structure.

OFETs were fabricated to evaluate the impact of nanofiber orientation on the charge-carrier transport properties of the semiconducting polymer, which was deposited

by blade coating and spin coating the respective UV−P3HT solutions with different aging times onto device substrates. For the blade coated thin films, the preprocessed polymer solutions were coated in vertical and parallel directions with respect to the source/drain electrodes as shown in the Figure 3.15. Representative transfer and output curves acquired from OFETs with semiconducting layers deposited by spin coating and blade coating in parallel and vertical directions are presented in Figure 3.16.

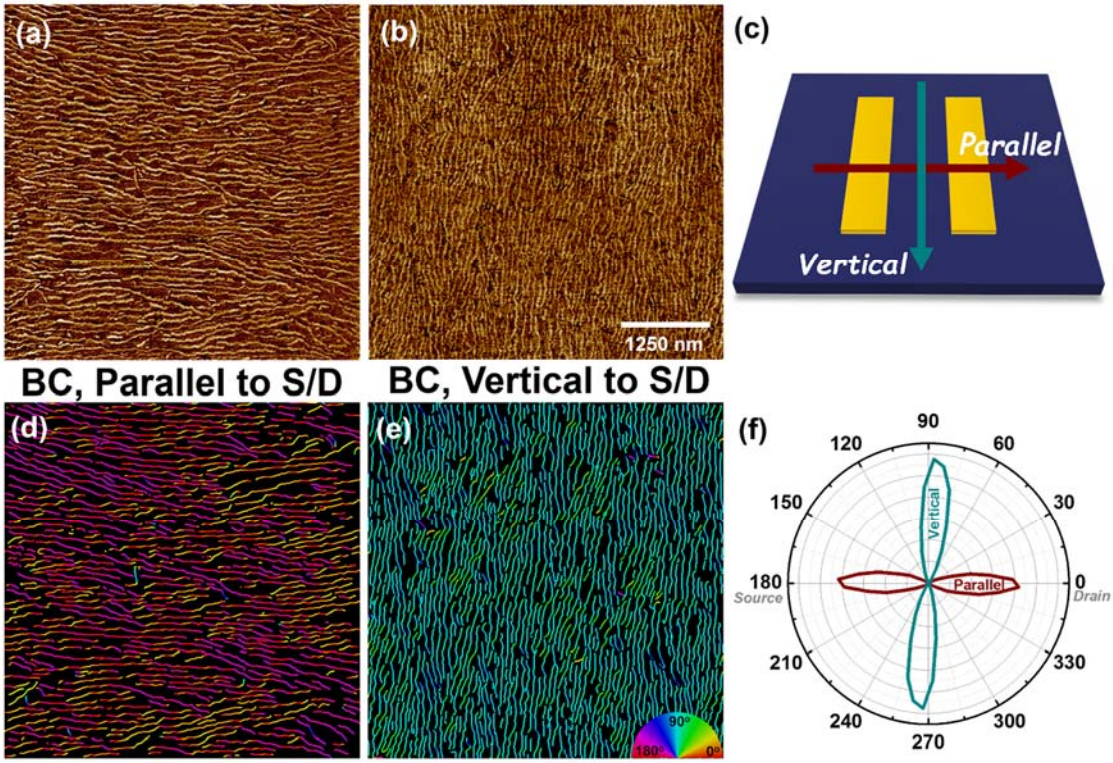

Figure 3.15 AFM phase images (5 × 5 μm) of P3HT thin films deposited by blade coating 24 h aged UV-irradiated P3HT solution in (a) parallel and (b) vertical direction. (c) Blade coating parallel and vertical to the direction of source and drain electrodes. AFM images analysis (5 × 5 μm) of P3HT thin films deposited by blade coating 24 h aged UV-irradiated P3HT solution in (a) parallel and (b) vertical direction. (f) Orientation distribution of P3HT nanofibers collected from the blade coated films.

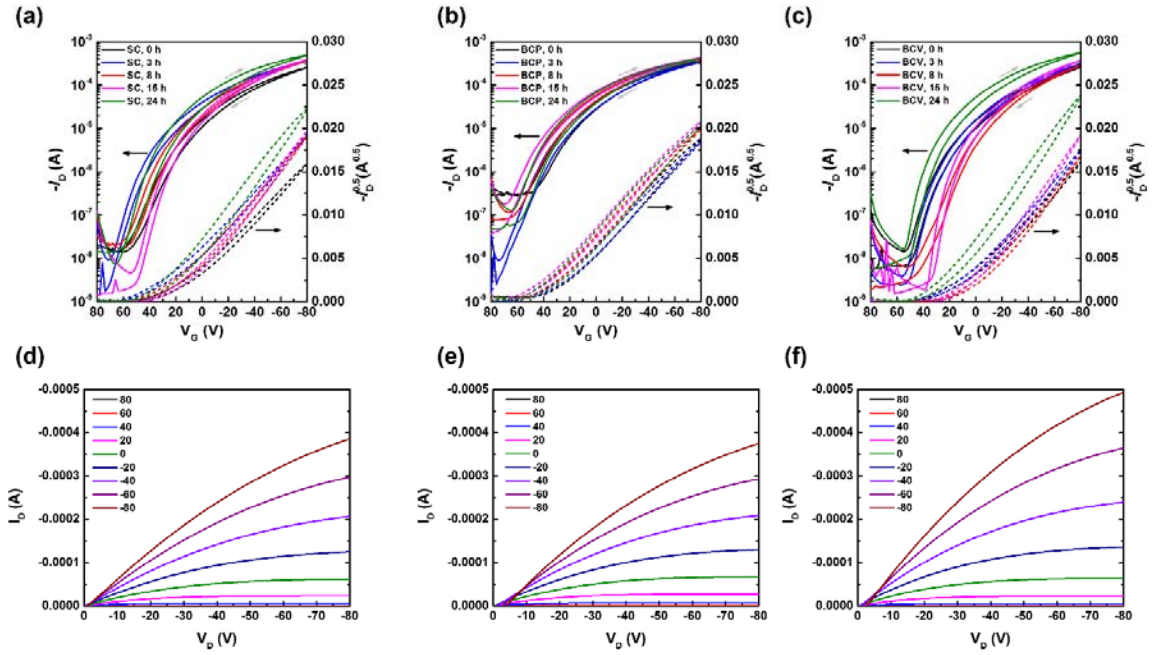

Figure 3.16 Forward and backward (V_G swept between -80 to 80 V) transfer characteristics of OFETs with active layers deposited by (a) spin coating and blade coating (b) parallel and (c) vertical to the direction of source and drain electrodes. Output characteristics of OFETs with active layers deposited by (d) spin coating and blade coating (e) parallel and (f) vertical to the direction of source and drain electrodes. All of the OFETs were operated at $V_D = -80$ V.

The calculated charge carrier mobilities extracted from the transfer characteristics were plotted against the solution-aging time as shown in Figure 3.17a. The charge-transport performance of spin coated and blade coated OFETs all gradually increased with extended solution-aging time, as anticipated due to the improvement in thin-film crystallinity. However, the blade coated samples exhibited anisotropic charge-transport properties when the films were fabricated by blade coating in directions parallel and perpendicular to the source/drain electrodes. For well-aligned nanofibrillar thin films, such as those obtained from blade coated 24 h aged UV−P3HT, the charge carrier mobility was an average of 0.198 ± 0.003 $cm^2 V^{-1} s^{-1}$ and 0.122 ± 0.004 $cm^2 V^{-1} s^{-1}$ for

films fabricated in the vertical and parallel directions, respectively. These results can be ascribed to the fact that the intramolecular charge transport of well-aligned nanofibrillar structures in the vertical direction with respect to source/drain electrodes is more effective than in the parallel direction (Figure 3.17b). Note that intramolecular charge transport along the conjugated polymer backbone is reported to be much faster than intermolecular charge transport parallel to π–π stacking direction (Figure 3.17c).[2] As a result, charge transport anisotropy was enhanced with increased solution-aging time, and can be correlated with the degree of chain alignment.

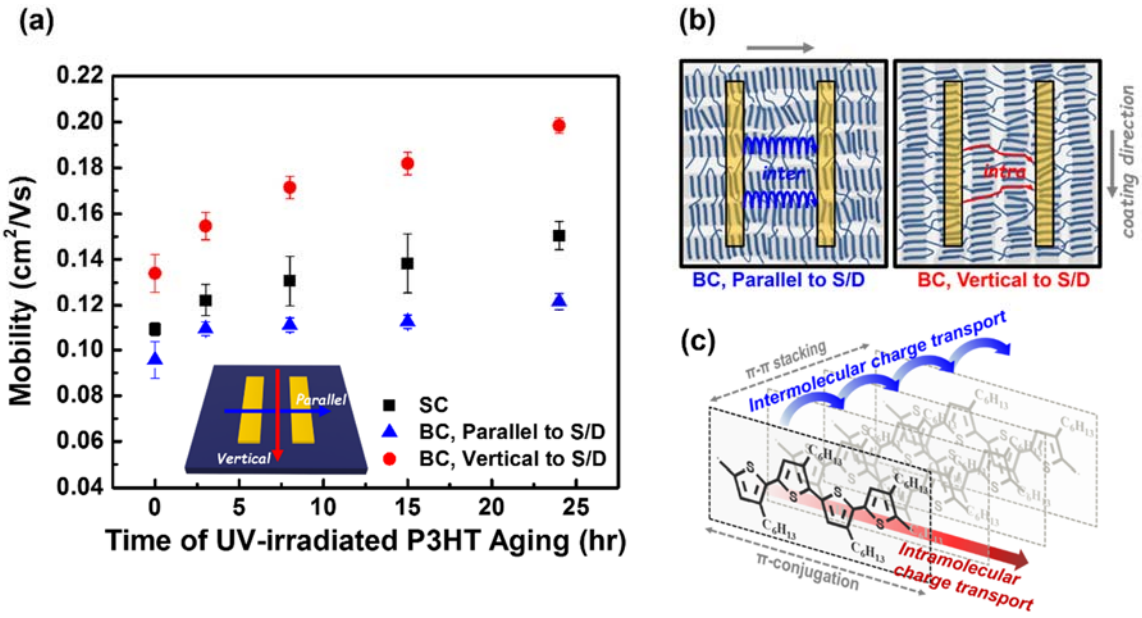

Figure 3.17 (a) Average charge carrier mobilities of OFETs with active layers deposited by spin coating and blade coating in parallel and vertical directions. (b) Schematic diagram of blade coated films with perfectly aligned nanofibrillar structures parallel and vertical to source/drain electrodes. The short blue lines schematically indicate the individual polymer chains. Long blue and red line represent the intermolecular and intramolecular charge transport, respectively, (c) charge transport direction in P3HT crystalline structure.

Furthermore, the remarkable charge transport mobility observed from the films deposited by blade coating in the vertical direction could further support the premise that the nanofibrillar structures are interconnected by tie-chains, which serve as bridges between well-aligned nanofibers to afford efficient intramolecular charge transport.[151, 163, 198] To demonstrate reproducibility, the mobility distribution of over 20 devices is illustrated in Figure 3.18. For spin coated thin films, the randomly oriented nanofibrillar structure may exhibit binary charge transport behavior, resulting in an intermediate charge carrier mobility.

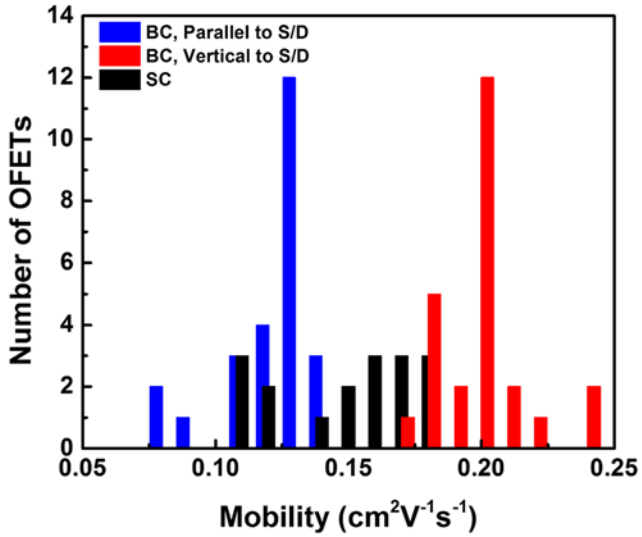

Figure 3.18 Mobility distribution of OFETs with active layers deposited by spin coating and blade coating parallel and vertical to the direction of source and drain electrodes.

3.4 Conclusions

The combination of UV-irradiation and solution aging was shown to facilitate the control of polymer self-assembly, which exhibits a strong correlation with thin film crystallinity and charge transport anisotropy. Rather than effecting alignment of the individual polymer backbones without long-range positional ordering, we demonstrated a facile strategy to induce macroscopic alignment of P3HT by pre-stacking a significant fraction of polymer chains into orthorhombic nanofibers prior to the rapid thin film formation process. The pre-aggregated polymer chains were bonded by cofacial π–π interactions, and therefore, the tortuosity and entanglement effects of long polymer chains were significantly reduced during the blade coating process. According to surface morphology analysis, the orientation distribution of P3HT nanofibers were aligned parallel to the blade coating direction. The degree of chain alignment is greatly improved with increased polymer aggregation, which can be easily tuned by solution-aging time. Furthermore, the crystal planes are mainly oriented edge-on, which benefits in-plane charge transport. The strategy afforded well-aligned and long-range, macroscopically ordered nanofibrillar structures. It is noteworthy that the approach obviates the need for additional blade patterning or surface functionalization steps, suggesting a low-cost and scalable process for high-throughput flexible polymer semiconductor device manufacturing.

To the best of our knowledge, for the first time, we have demonstrated an evolution of P3HT nanofibers from totally randomly oriented to long-range aligned nanocrystalline architectures. The highly aligned nanofibrillar structure provides a platform to mechanistically elucidate the anisotropic charge transport behavior. The results indicate

that the charge carrier mobilities were determined by P3HT nanofiber orientation with respect to the direction of source and drain electrodes. The charge carrier mobility reached a maximum value as high as 0.241 $cm^2\ V^{-1}\ s^{-1}$ when the nanofibers were well-aligned perpendicular to the direction of source and drain electrodes, presumably due to enhanced intramolecular charge transport within the film. These results also support the concept that semicrystalline, semiconducting polymer nanofibers are often interconnected by tie-chains which allow for efficient charge transport between nanoaggregated structures. The significant insights that correlate thin film morphology/structure and charge transport anisotropy for well-aligned conjugated polymers are expected to impact the design and development of future high performance organic electronic devices.

CHAPTER 4. SYNERGISTIC EFFECT OF REGIOREGULAR AND REGIORANDOM POLY(3-HEXYLTHIOPHENE) BLENDS FOR HIGH PERFORMANCE FLEXIBLE ORGANIC FIELD EFFECT TRANSISTORS

4.1 Introduction

The anisotropic charge transport properties of conjugated polymers strongly depend on the molecular stacking and macroscopic polymer chain alignment, which has been systematically discussed in the previous Chapter.[2, 78] In addition to electrical properties, the most attractive advantage of OSCs is their inherent mechanical flexibility, which enable the possibility of various flexible applications such as electronic skin,[200] flexible display[77] and radio-frequency identification tags (RFID-tags).[114]

In general, high conjugated polymer crystallinity positively impacts thin film charge transport performance, but concomitantly can stiffen and embrittle the films, leading to seriously decreased mechanical reliability and integrity of devices under external strain.[61, 62, 201-203] Several strategies have been reported to alleviate this issue, including the use of organic semiconducting/insulating polymer blends. This blend approach has the potential to improve thin film mechanical compliance and reduce cost since the conjugated polymers are embedded within economical elastic insulators.[204-206] Importantly, semiconducting polymer electronic performance can be preserved, while exposure to the ambient environment is minimized.[207, 208] Though conjugated polymer electronic characteristics could be retained, devices were typically fabricated using rigid silicon

substrates with a thermally grown silicon dioxide (SiO_2) insulator. Thus, interrogation of mechanical performance through stretching or bending experiments was prohibited.[47, 206, 208-210]

Identification of compatible materials and processes for semiconducting/insulating polymer blend thin film transistors poses additional challenges when the semiconductor and dielectric are both solution-processed organic materials. Since the insulating polymer blend components, i.e., polystyrene (PS), poly(methylmethacrylate) (PMMA), or polydimethylsiloxane (PDMS) are also common dielectric materials for flexible device applications, it can prove challenging to deposit an insulator blend film without impacting the underlying layer.[208, 211, 212] Dielectrics such as divinyltetramethyldisiloxanebis-(benzocyclobutene) that require high temperature curing must also be avoided since many flexible substrates cannot sustain the thermal curing process.[213] These factors further limit the set of available dielectric materials and corresponding solvents.

The alternative top-gate flexible device architecture requires two sequential solution-processing steps, which also presents challenges. Identification of compatible solvents can be difficult, but perhaps equally importantly, the morphological characteristics of the semiconductor–dielectric interface can impact performance. For instance, active layer crystallinity and charge carrier transport improve when the semiconductor morphology comprises nanorods or nanofibrils;[107, 214, 215] however, concomitantly, surface roughness, detrimental for subsequent deposition of a uniform dielectric layer, is increased. A nonuniform dielectric can effect excessive current leakage and degradation of device performance.[211]

Herein, we demonstrated a facile and scalable blend approach to fabricate flexible OFETs using low-dose UV irradiated RR-P3HT/RRa-P3HT blend thin films as the active layers. RR-P3HT nanofibrillar structures were formed in solution via UV irradiation, and co-deposited with untreated RRa-P3HT in different blend ratios. In contrast to conventional semiconductor/insulator blend approaches, the insulating component here was RRa-P3HT, which facilitated solution deposition of a uniform dielectric layer. Interrogation of the resultant blend thin films revealed that the semiconducting nanofibrils formed upon UV irradiation were embedded well into the RRa-P3HT matrices. The nanofibrous network was enriched at the substrate interface and afforded a continuous semiconducting layer in contact with the source/drain electrodes. Consequently, charge transport performance was preserved, even when the blend films were comprised of only a very small proportion of RR-P3HT. Moreover, owing to the mechanical flexibility of the amorphous RRa-P3HT matrix,[60] blend film charge transport performance survived a series of bending experiments. Materials thin film crystallinity, surface morphology, photophysical properties, and electrical performance were further investigated via GIWAXS, AFM, UV–vis absorption spectroscopy and charge carrier mobility measurements, respectively. The experimental observations provide a robust materials chemistry foundation for the advantageous use of regioregular/regiorandom semiconducting polymer blends. The results suggest a promising methodology for large area roll-to-roll printing of flexible, solution-processed π-conjugated polymer devices and circuits.

4.2 Experimental Methods

4.2.1 Materials

The RR-P3HT (MW: 51 kD, PDI: 2.1, RR: 96%) and RRa-P3HT (MW: 60–95 kD, PDI: 2.8–3.1) were purchased from Rieke Metals Inc. The PMMA (MW: 996 kD), chlorobenzene (anhydrous), and chloroform (anhydrous) were purchased from Sigma-Aldrich. All of the materials are used without further purification. The DuPont Teijin PET (Polyethylene terephthalate) films were selected as flexible substrates (Melinex ST505, 5.0 mil, 48"×24", Tekra Corp.).

4.2.2 Blend Solutions Preparation

For UV irradiated RR-P3HT samples, the RR-P3HT solution (5 mg mL^{-1}) was performed by following the published UV irradiation procedure.[112] The UV irradiation time was fixed at 8 min while the solution exhibited a notable color change from bright orange to dark brown, indicating that the RR-P3HT began to aggregate and form nanofibrillar structures in the solution state. The RRa-P3HT (5 mg mL^{-1}) solutions were prepared in chlorobenzene at ~55 °C for 30 min. After complete dissolution, the RRa-P3HT solution was cooled to room temperature and mixed with UV irradiated RR-P3HT solution with defined ratios (RR-P3HT:RRa-P3HT = 100:0, 25:75, 50:50, 40:60, 30:70, 20:80, 10:90, 5:95, 0:100), which is corresponding to the percentage by weight of RRa-P3HT in blend films (0, 25, 50, 60, 70, 80, 90, 95, 100%). The 0% and 100% are representing the pure UV irradiated RR-P3HT and the pure RRa-P3HT, respectively. The pristine RR-P3HT thin films were also prepared by dissolving 5 mg RR-P3HT in 1 mL chloroform at ~55 °C for 30 min, and deposited without any processing treatment.

4.2.3 PDMS Sheet Fabrication

The silicone elastomer base and the curing agent were mixed in a ratio of 10:1 and poured onto a plastic mold. The bubbles were removed with a vacuum pump and the silicones were hardened by heat treatment in an oven (at 50 °C) for 1.5 h. After solidification, the PDMS sheets were attached to the top of P3HT thin films, which were pre-deposited on substrates. The adhesion difference between PDMS/P3HT and P3HT/substrate interfaces makes it possible to peel off from the PET substrate and expose the bottom layer of P3HT thin films to air.

4.2.4 Flexible OFETs Fabrication and Characterization

The flexible OFETs with top-gate bottom-contact configuration were fabricated to characterize charge transport properties of P3HT films, which were deposited from solutions prepared as above. The 50 nm Au source and drain electrodes with 3 nm Cr as adhesion layer were both deposited by shadow mask evaporation onto the PET substrates. Before the thin films formation process, the Au/Cr/PET substrates were rinsed with acetone, methanol, and isopropanol. The active layers were deposited by spin coating (WS-650MZ-23NPP, Laurell) the blend solutions onto precleaned flexible substrates at a spin speed of 1500 rpm for 60 s. Subsequently, PMMA solutions (40 mg mL^{-1}) were directly spin coated on the top of active layers at a spin speed of 1500 rpm for 90 s, resulting in 600 nm thick dielectric and encapsulation layers. All of the thin films deposition was fabricated under ambient conditions. The flexible OFETs were completed by drop casting the PEDOT:PSS as gate electrodes, which were deposited on the top of dielectrics and fully covered the active channel area. The OFET electrical properties were

investigated in nitrogen ambient using an Agilent 4155C semiconductor parameter analyzer. The filed effect mobilities were calculated in saturation regime from the transfer plot of V_G versus I_D and using the following Equation 4.1:

$$I_D = \frac{W}{2L} C_i \mu (V_G - V_{Th})^2 \quad (4.1)$$

Where W and L refer to channel length (30 μm) and width (1000 μm), respectively, C_i is the capacitance per unit area of the PMMA gate dielectric (5.31×10^{-9} F cm^{-2}), μ represents the hole mobility, V_G and V_{Th} denote gate voltage and threshold voltage, respectively.

4.2.5 UV-vis Spectroscopy (UV-vis)

The solution and solid state UV–vis spectra were obtained using Agilent HP 8510 UV–vis spectrophotometer. The blend thin films were prepared by spin coating the corresponding solutions onto precleaned glass slides.

4.2.6 Grazing-Incidence Wide-Angle X-Ray Scattering (GIWAXS)

The GIWAXS measurements were carried out on beamline 11–3 at the Stanford synchrotron radiation light source. The beam was fixed at an energy of 13 keV and the critical angle was 0.12°. The measurements were calibrated by a LaB 6 standard sample. The 2D images were corrected from intensity versus pixel to intensity versus q-spacing by using the WxDiff software. The 1D line-cut profiles were obtained from the processed 2D images, and the peaks were subjected to the Gaussian fitting.

4.2.7 Stylus Profilometer

The thin fi lm thicknesses were measured by using a Bruker DektakXT stylus profilometer in Hills & Valleys mode. The scan lengths were 700–1000 μm with 10 s scan duration.

4.2.8 Atomic Force Microscopy (AFM)

The surface morphologies of the thin films were characterized by AFM using a Bruker Dimension Icon atomic force microscopy system, operating in tapping mode. The top and bottom surfaces were measured by HQ:NSC14 and HQ:NSC15 n-type silicon tips, respectively.

4.3 Results and Discussions

4.3.1 Photophysical Properties

Figure 4.1a and b presents optical absorption spectra of pristine and UV irradiated RR-P3HT (0%) solutions and corresponding thin films. The pristine solution phase spectrum exhibits the expected single absorption maximum at ~453 nm. Low energy absorption bands at ~550 and ~605 nm associated with intrachain (0–1) and interchain (0–0) vibronic transitions, respectively, are seen in the UV irradiated polymer solution and indicate the formation of P3HT aggregates.[129] The further development of weak absorption bands (at ~605 nm) for UV irradiated RR-P3HT (0%) films support prior

results suggesting that the irradiation process promotes formation of a well-ordered thin-film morphology.[128, 129, 183]

Figure 4.1c depicts the absorption spectra of UV-irradiated RR/RRa-P3HT blend solutions. The 100% regiorandom solution exhibited an absorption maximum at ~433 nm, which represents a slight blue-shift in comparison to the regioregular counterpart. The shift is likely due to increased steric distortions that emanate from the former.[130] As the proportion of UV irradiated RR-P3HT decreased, the lower energy band intensities appeared to decrease proportionately. In the solidified state, the primary π–π* transition underwent a notable redshift with respect to the corresponding solution spectra (Figure 4.1c and d). Increased irradiated RR-P3HT concentration led to what appears to be a more extensive shift in the peak position due to higher degree of polymer chain planarization in solid state. Further, upon incorporation of the regioregular blend component, weak absorption bands were observed at ~605 nm, which corresponds to (0–0) vibronic transitions.[129] The low energy band intensities are consistent with the proportions of the two components. The long wavelength absorbance is apparent even when the film was comprised of 90% RRa-P3HT. Thus, the stronger interchain π–π electronic coupling between RR-P3HT chains is not disrupted upon incorporation of the regiorandom analog.[127, 216] It can be inferred that incorporation of RRa-P3HT does not interfere with continued aggregation of irradiated RR-P3HT during the rapid thin film formation process.

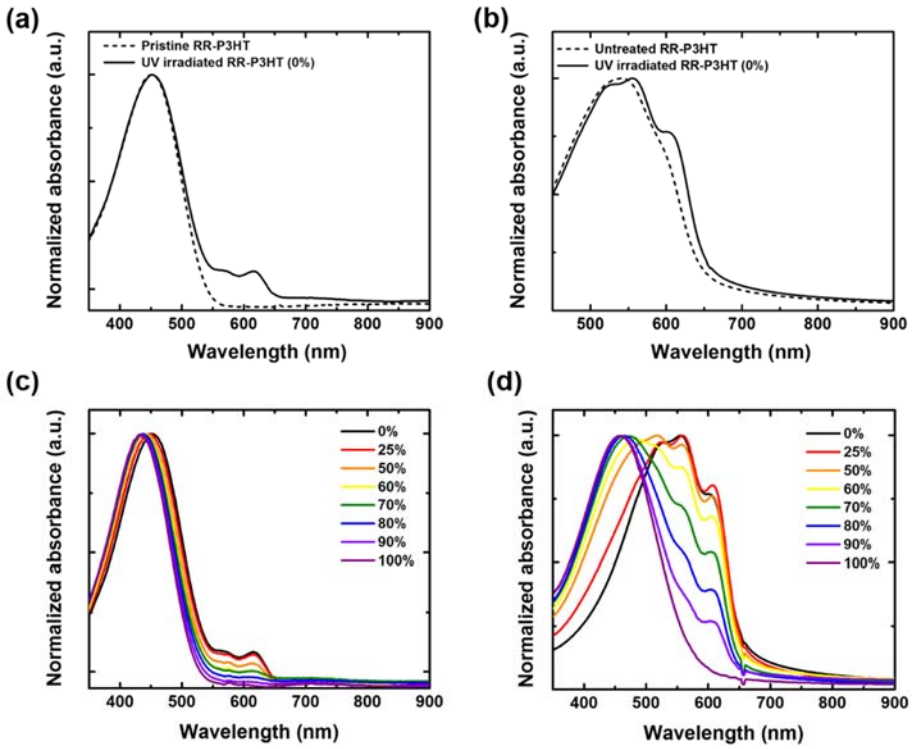

Figure 4.1 Normalized UV–vis absorption spectra of pristine RR-P3HT and UV irradiated RR-P3HT (0%) in (a) solution state and (b) solid state. Normalized UV–vis absorption spectra of UV irradiated RR-P3HT/RRa-P3HT blend (c) solutions and (d) thin films with varying blend ratios.

The intra- and intermolecular ordering of the polymer chains was analyzed quantitatively using Spano's model.[131-133] The thin film UV–vis spectra have contributions that emanate from both crystalline and amorphous regions. The amorphous phase which is composed of largely disordered polymer chains, exhibits higher energy features. The lower energy vibronic bands are ascribed to the more ordered crystalline phase. Within the crystalline region, the ratio of the 0–0 and 0–1 vibronic bands has been correlated with the free exciton bandwidth (W), which enables estimation of the magnitude of interchain coupling within aggregates.[129, 133] A decrease in W is generally

associated with increased conjugation length and/or chain ordering. The values of W were calculated by the following Equation 4.2:

$$\frac{I_{0-0}}{I_{0-1}} \approx \left(\frac{1 - 0.24W/E_p}{1 + 0.073W/E_p}\right)^2 \tag{4.2}$$

I_{0-0} and I_{0-1} represent the intensities of the 0–0 and 0–1 transitions, respectively, obtained from Gaussian fits to the experimental spectra (Figure 4.2a-g). E_p denotes the vibrational energy of the symmetric vinyl stretch (taken as 0.18 eV).[133, 216] The absence of a perceptible low energy band for pristine RR- and RRa-P3HT thin films obviated estimates of W for those samples. UV irradiated RRP3HT (0%) exhibited a W value of 241 meV (Figure 4.2h). Surprisingly, W decreased significantly to ~120 meV upon incorporation of RRa-P3HT. This result supports the earlier UV–vis spectral analysis suggesting that the inclusion of less ordered RRa-P3HT in the blend thin films does not negatively impact the molecular assembly of RR-P3HT into ordered aggregates. Further, application of Spano's model to the experimental results strongly suggests that inclusion of the RRa polymer analog promotes increased, favorable intermolecular interactions of UV irradiated material.

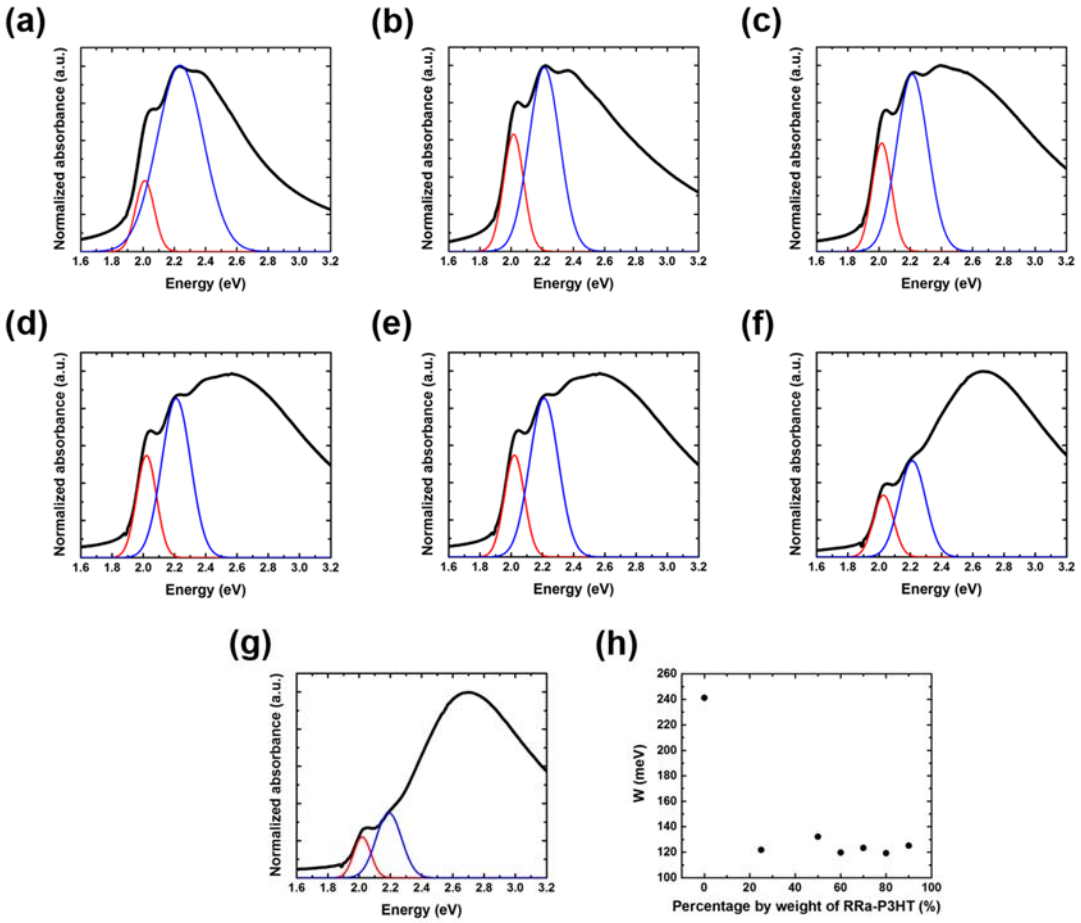

Figure 4.2 Normalized absorption spectra of UV irradiated RR/RRa-P3HT blend thin films, fabricated with a range of weight percentage of RRa-P3HT in blend films (a) 0%, (b) 25%, (c) 50%, (d) 60%, (e) 70%, (f) 80%, (g) 90%. The black lines are the experimental absorption spectra. The red and blue Gaussian fitted lines indicate 0-0 and 0-1 vibronic transition bands, respectively. (h) Evolution of exciton bandwidth (W) as a function of additional RRa-P3HT weight ratios.

4.3.2 Thin Film Crystallinity

The molecular packing and orientation of crystalline domains of pristine RR-P3HT and UV irradiated RR/RRa-P3HT blend thin films were investigated by GIWAXS as shown in Figure 4.3a-c. The 2D GIWAXS profiles of both films present (100) reflection

peaks along the out-of-plane (q_z) direction, corresponding to P3HT lamellar stacking oriented normal to the substrate. However, halo-like patterns are apparent along the azimuthal angle, which indicate a random oriented thin film microstructure, even in the case of the irradiated semiconducting polymer film. In contrast to the relatively isotropic patterns obtained from the pure RR-P3HT samples, the UV irradiated RR/RRa-P3HT blend, comprised of 80% regiorandom polymer exhibits a series of intense characteristic (*h*00) (*h* = 1, 2, 3) spots along the q_z direction. Additionally, the apparently improved π–π interchain stacking of the polymer backbones leads to stronger (010) arcs along the in-plane (q_{xy}) axis, suggesting that the crystallites are well organized and preferentially in an edge-on orientation.[74, 99] For pristine RRa-P3HT, the amorphous thin film structure exhibits a completely isotropic pattern without any significant reflection as shown in Figure 4.4.

Figure 4.3d and e depicts the line-cut profiles of structures at χ = 15° and 85°, which represent out-of-plane and in-plane 1D–GIWAXS patterns. The out-of-plane scattering (Figure 4.3d, χ = 15°) exhibits strong (100) peaks at q = 0.371, 0.372, and 0.376 ($Å^{-1}$) for pristine RR-P3HT, UV irradiated RR-P3HT (0%), and UV irradiated RR/RRa-P3HT (80%), respectively. The (100) peak intensity of the UV irradiated blend sample was significantly increased in comparison to either pristine RR-P3HT or UV irradiated RRP3HT. Furthermore, a second order (200) peak at q = 0.751 ($Å^{-1}$) and third order (300) peak at q = 1.130 ($Å^{-1}$) were also observed in the out-of-plane line-cut profile. The appearance of these high order reflections is a strong indicator of enhanced thin film crystallinity.[191] The position and full width at half-maximum of the diffraction peaks can be correlated to the lamellar spacing and crystalline correlation lengths

(crystalline domain sizes) via Scherrer's equation in reciprocal space.[137] The calculated d_{100}-spacing and crystallite size of UV irradiated RR-P3HT (0%) were slightly improved compared to pristine RR-P3HT from 16.90 to 16.88 Å and 78.03 to 79.74 Å, respectively, as show in Table 4-1 . When the UV irradiated semiconductor was incorporated into RRa-P3HT matrices, the alkyl lamellar stacking became more close-packed (d_{100}-spacing = 16.68 Å), and the crystalline domain size increased to 97.48 Å.

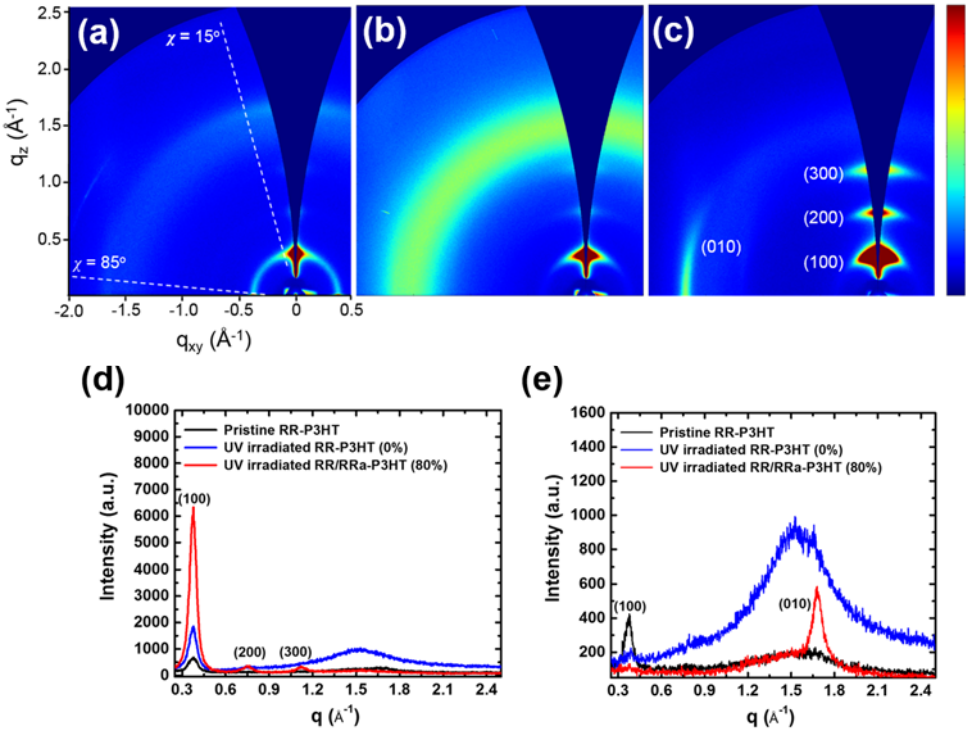

Figure 4.3 2D-GIWAXS patterns of (a) pristine RR-P3HT, (b) UV irradiated RR-P3HT (0%) and c) UV irradiated RR/RRa-P3HT (80%). The line-cut profiles of (d) out-of-plane (χ = 15°) and (e) in-plane (χ = 85°) GIWAXS patterns.

A reflection peak at q = 0.371 (Å^{-1}) is evident in the in-plane scattering (Figure 4.3e, χ = 85°) of pristine RR-P3HT, which indicates that some portion of the untreated polymer thin film crystal planes lie parallel to the substrate.[74, 217] Although this reflection was not evident in single component UV irradiated RR-P3HT, the in-plane profile

appears as a broad band extending from q = 0.9 to 2.1 ($Å^{-1}$), which may be due to scattering from randomly oriented regions.[192, 218] The π–π stacking distance of this UV irradiated RR-P3HT sample was difficult to calculate, since the (010) peak is fully overlapped with the broad scattering. In addition, no significant (010) peak can be observed from pristine RR-P3HT thin films. The UV irradiated RR/RRa-P3HT (80%) blend thin film results are substantially different. A single sharp (010) peak was recorded at q = 1.688 ($Å^{-1}$), or alternatively a π–π intermolecular stacking distance (d_{010}-spacing) of 3.72 Å, as shown in Table 4-1. These results support the UV–vis data that suggest a strong intermolecular overlap integral for the blend system.[78, 192, 219]

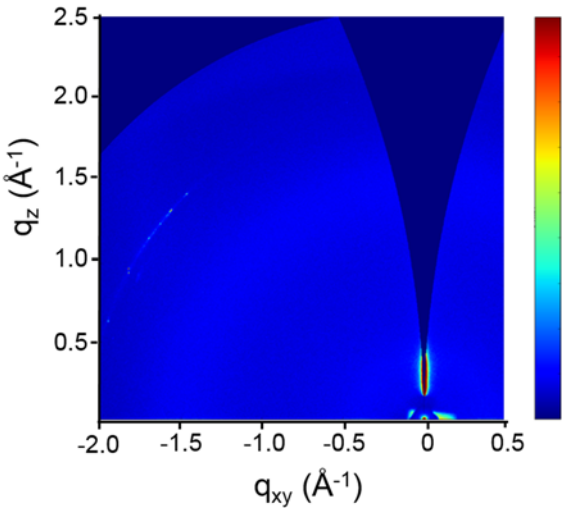

Figure 4.4 2D-GIWAXS pattern of pristine RRa-P3HT.

The electrical properties of semiconducting polymers are intimately related to crystal orientation, which can be quantified by Herman's orientation factor, f_H. Calculated from the first order alkyl stacking (100) peaks, these factors can range from -0.5 to 1, where 1 corresponds to perfectly oriented crystal planes perpendicular to the substrate (edge-on), -0.5 denotes a lattice plane strictly oriented parallel (face-on), and

randomly oriented structures afford a factor value at 0.[192, 220, 221] As shown in Table 4-1, UV irradiated RR/RRa-P3HT (80%) provides for the highest f_H at 0.59, suggesting a highly oriented microstructure with primarily edge-on orientation. Such a microstructure is expected to facilitate efficient charge transport in the plane of substrate.

Table 4-1. GIWAXS peaks analysis data of pristine RR-P3HT, UV irradiated RR-P3HT (0%) and UV irradiated RR/RRa-P3HT (80%).

	d_{100} (Å)	d_{010} (Å)	crystalline size (Å)	f_H
Pristine RR-P3HT	16.90	-	78.03	0.10
UV irradiated RR-P3HT (0%)	16.88	-	79.74	0.27
UV irradiated RR/RRa-P3HT (80%)	16.68	3.72	97.48	0.59

4.3.3 Surface Morphology

AFM was used to examine the thin film surface morphologies. Pristine RRa-P3HT (100%) thin films are as expected, amorphous and featureless (Figure 4.5a), while pristine RR-P3HT exhibits nanoscale fibrillar structures as shown in Figure 4.5b. Pre-deposition processing with low intensity UV irradiation led to the development of distinct rod-like nanofibrils (Figure 4.5c). Upon blending with up to 80% RRa-P3HT, the nanorod density significantly decreased and became isolated by disordered regions (Figure 4.5d). Concomitantly, surface roughness of the blend was reduced from 3.05 to 1.07 nm versus the UV irradiated semiconductor.

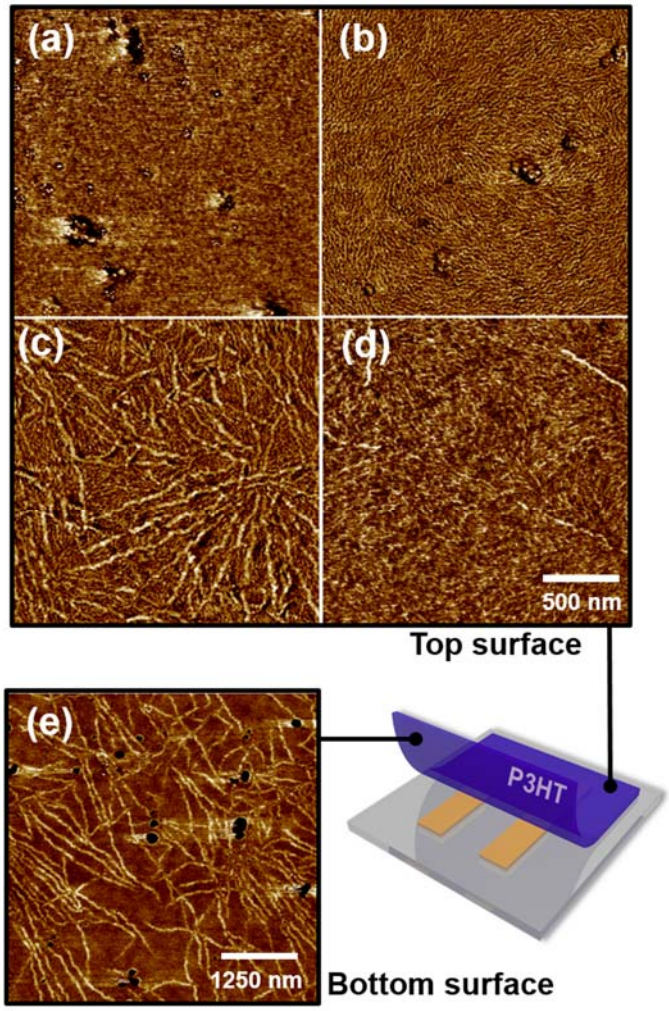

Figure 4.5 AFM phase images (2 × 2 μm) of the top surface of (a) pristine RRa-P3HT, (b) pristine RR-P3HT, (c) UV irradiated RR-P3HT (0%) and (d) UV irradiated RR/RRa-P3HT (80%). (e) AFM phase images (5 × 5 μm) of the bottom surface of UV irradiated RR/RRa-P3HT (80%).

Since GIWAXS and UV–vis analyses point to superior intermolecular stacking and anisotropic crystalline orientation for UV irradiated RR/RRa-P3HT (80%) blend thin films, the appearance of only a limited number of P3HT nanofibrils was somewhat unexpected. To explore the possibility that a preponderance of well-ordered structures was present at the film–substrate interface, the blend films were peeled from the substrates and transferred to PDMS sheets for AFM interrogation. As shown in Figure

4.5e, significantly more nanofibrils were observed at the bottom surface of the blend films. In addition, nanofibril length increased from 300–800 to 1500–2000 nm for blend versus UV irradiated RR-P3HT films. The AFM evidence demonstrates that RR-P3HT nanofibrils were vertically phase segregated from the regiorandom polymer and formed preferentially at the semiconductor–substrate interface.

4.3.4 Mechanistic Interpretation

In the single-component system, nanostructure development is believed to be driven by nucleation and crystal growth, and the preaggregated nanofibrils facilitate formation of extended supramolecular semiconducting polymer assemblies; invariably however, spontaneous nucleation and random crystal growth take place during solvent evaporation. Thus, well oriented nanofibrillar structures are difficult to achieve during the rapid thin film formation process.

For the binary system explored here, the essential driving force for crystallization relies on both molecular self-assembly and vertical phase segregation of the components (Figure 4.6a and b). Deposition of the apparently metastable RR/RRa-P3HT blend solution leads to supersaturated RR-P3HT aggregates effectively 'precipitating' to the substrate as opposed to either remaining distributed within the film or segregating to the fi lm–air interface. Presumably, heterogeneous nucleation is more favorable on foreign objects, which exhibit lower nucleation energy barriers.[222, 223] Additionally, in contrast to the random coil conformation of RRa-P3HT chains, the surface of well-stacked RR-P3HT nanofibrils is essentially encased by nonpolar hexyl side chains, which

preferentially interact with the hydrophobic substrate, leading to an edge-on semiconductor configuration for the blend films. The thickness of these ordered regions depended upon the RR/RRa ratio. Conceivably, reduced RR-P3HT concentration in blend films with concomitant decreased thickness of the ordered regions at the substrate interface leads to confinement and resultant narrowed crystal orientation distribution in accordance with the GIWAXS results. Note that Joshi et al.[224-226] demonstrated that thinner polymer films appear as more oriented crystalline structures vs. thicker films due to confinement effects.

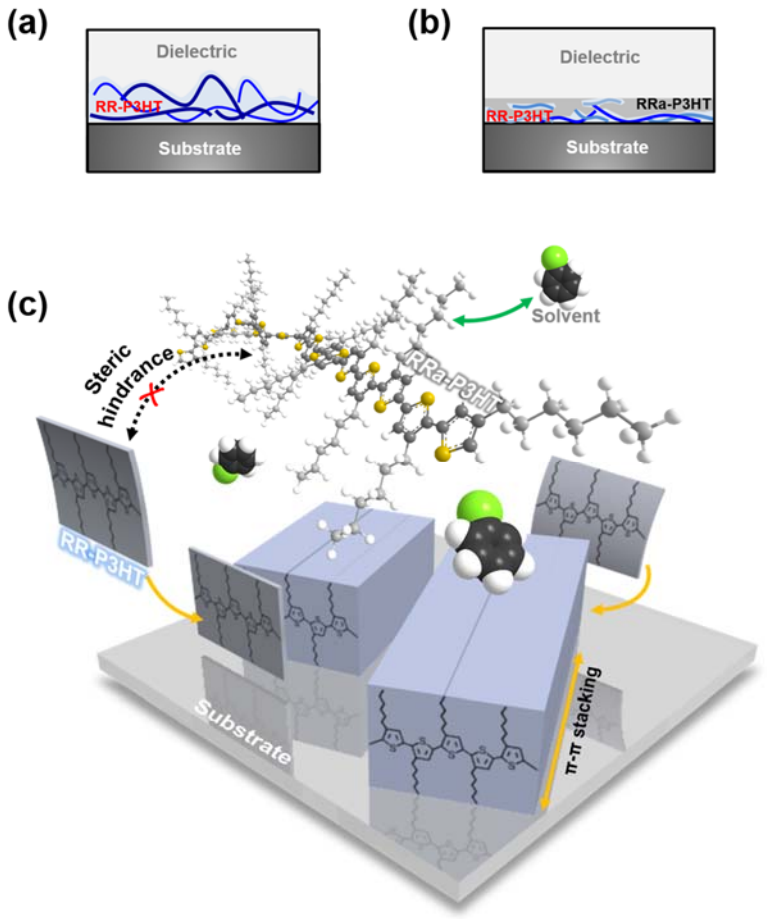

Figure 4.6 Schematic of vertical depth profiles for (a) 0% and (b) 80% of UV irradiated RR/RRa-P3HT blend thin films. (c) Schematic depicting the proposed mechanism of phase separation for UV irradiated RR/RRa-P3HT (80%) blend thin films.

Further, randomly oriented RRa-P3HT side chains (e.g., H–H coupling) give rise to a twisted polymer backbone, which suppresses the effective conjugation length and inhibits interchain interactions. Unfavorable steric interactions between the RR and RRa components may facilitate migration of the RR-P3HT toward the substrate, where the proportion of RRa-P3HT is more limited. Concomitantly, the regioregular polymer chains come into contact with RR-P3HT nucleation sites near the substrate surface, experience favorable intermolecular interactions and undergo π–π stacking into relatively long nanofiber networks (Figure 4.6c). In contrast to the moderately supersaturated UV irradiated RR-P3HT, untreated RRa-P3HT experiences more favorable solute–solvent interactions and tends to remain solubilized. Hence, the more soluble electroactively inert polymer preferentially accumulates at the film–air interface, which is where solvent evaporation generally begins. The synergistic effects of repulsive steric interactions between the RR and RRa components and favorable intermolecular interactions between RR-P3HT chains promote effective growth of RR-P3HT into well-organized assemblies at the semiconductor–substrate interface. During the course of thin film solidification, relatively long nanofibrillar structures, as observed in the AFM images, develop.

4.3.5 Charge Transport Performance

Macroscale charge carrier transport properties of pristine RRP3HT and UV irradiated RR/RRa-P3HT blend thin films were evaluated using a top-gate bottom-contact flexible OFET device architecture (Figure 4.7a). The active layer was deposited by spin coating the respective blend solutions onto PET substrates, PMMA was the dielectric and

poly(3,4-ethylenedioxythiophene) polystyrene sulfonate (PEDOT:PSS) served as the gate electrode. The active channel length and width between the gold source and drain electrodes was 30 and 1000 μm, respectively. Representative transfer and output curves obtained from UV irradiated RR/RRa-P3HT blend OFETs are presented in Figure 4.7c and 4.8, respectively.

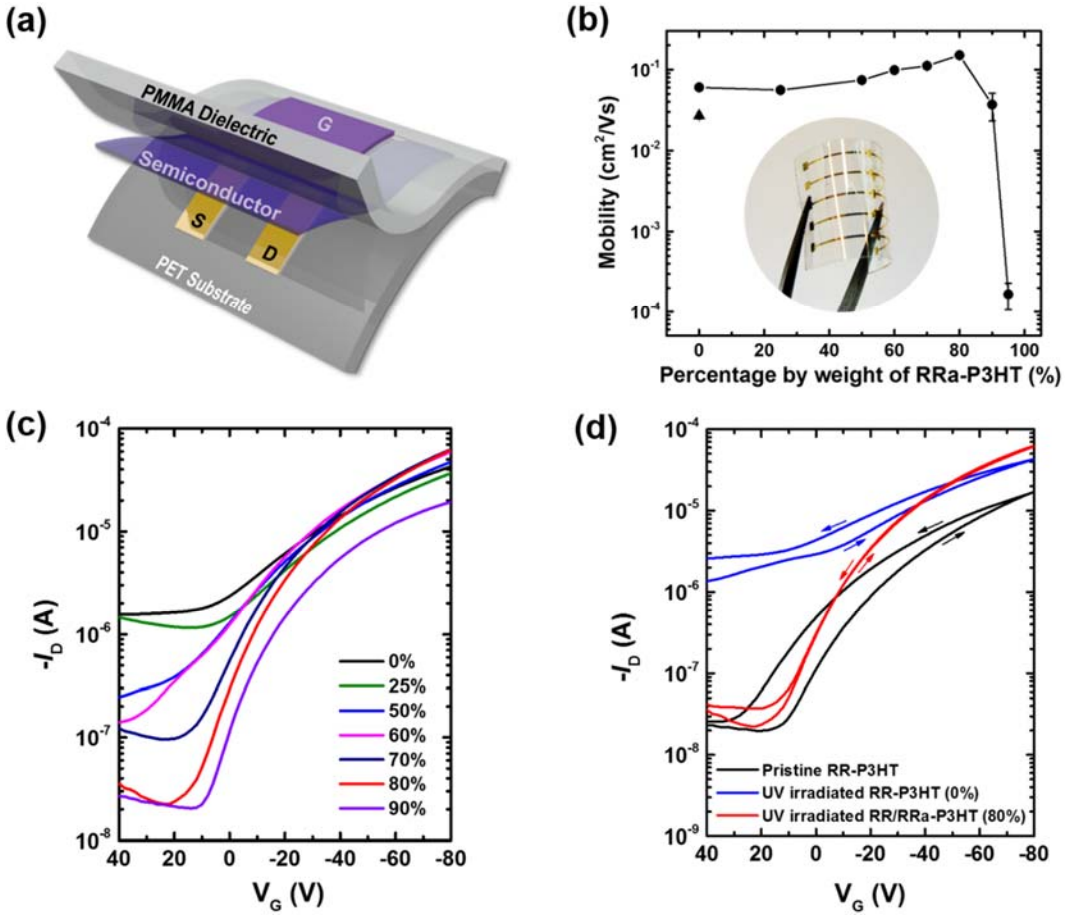

Figure 4.7 (a) Device configuration of flexible OFETs. (b) Average field-effect mobilities obtained from pristine RR-P3HT (black triangle) and UV irradiated RR/RRa-P3HT blend OFETs as a function of RRa-P3HT concentrations. (c) Transfer characteristics of UV irradiated RR/RRa-P3HT blend OFETs with different blend percentages of RRa-P3HT. (d) Forward and backward (V_G = 40 and −80) transfer characteristics of pristine RR-P3HT, UV irradiated RR-P3HT (0%), and UV irradiated RR/RRa-P3HT (80%). All of the OFETs were operated at V_D = −40 V.

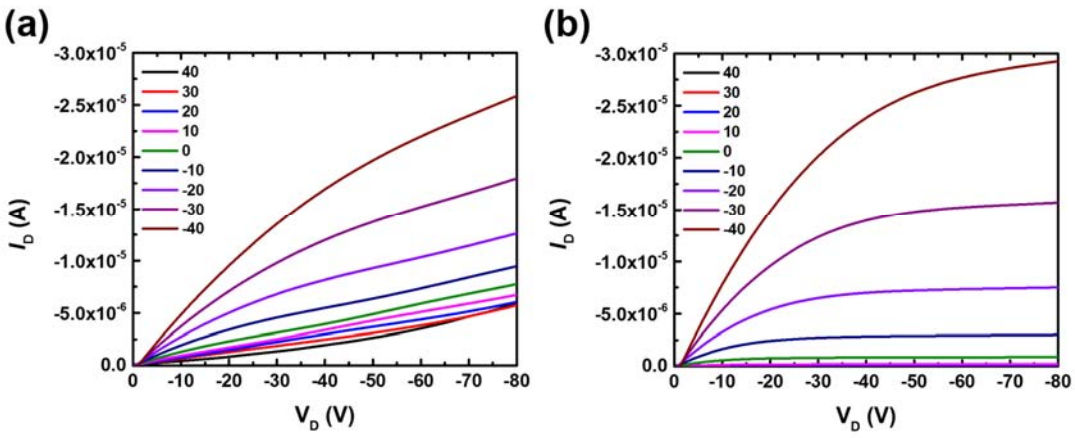

Figure 4.8 Output characteristics of (a) UV irradiated RR-P3HT (0%) and (b) UV irradiated RR/RRa-P3HT (80%) flexible OFETs. (V_G = 40 to −40).

The average charge carrier mobilities, as a function of RRa-P3HT weight percentage, are given in Figure 4.7b. The calculated field effect mobility of pristine RR-P3HT ($2.69 \pm 0.28 \times 10^{-2}$ cm^2 V^{-1} s^{-1}) is also provided (Figure 4.7b). UV irradiated RR-P3HT exhibited approximately a two-fold enhancement in charge carrier mobility ($6.03 \pm 0.30 \times 10^{-2}$ cm^2 V^{-1} s^{-1}), which most likely derives from well-ordered RR-P3HT fibrillar structures formed in solution upon UV irradiation.[112] Incorporation of RRa-P3HT into the irradiated RR polymer solution afforded no degradation in OFET performance. Rather, charge carrier mobility increased gradually with increased levels of the RRa polymer analog. The 80% UV irradiated RR/RRa-P3HT blend thin film devices reached a maximum hole mobility of 2.17×10^{-1} cm^2 V^{-1} s^{-1} ($1.58 \pm 0.05 \times 10^{-1}$ cm^2 V^{-1} s^{-1} on an average), which represents approximately an eightfold and fourfold improvement in comparison to pristine and UV irradiated RR-P3HT (0%), respectively. To demonstrate reproducibility, the mobility distribution of over 30 flexible devices is illustrated in Figure 4.9. The device performance abruptly decreased to $1.67 \pm 0.61 \times 10^{-4}$ cm^2 V^{-1} s^{-1} when 95% of the blend was RRa-P3HT. At these higher levels of inert polymer loading,

discontinuous charge transport pathways are most likely. Pristine RRa-P3HT (100%) exhibited no measurable macroscopic charge carrier mobility, suggesting insulating behavior.

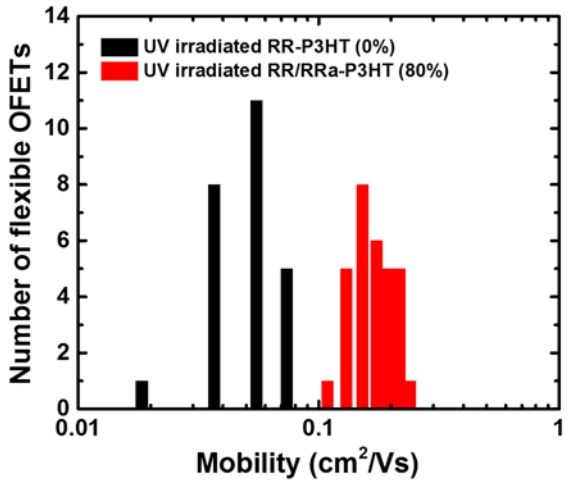

Figure 4.9 Mobility distribution of UV irradiated RR-P3HT (0%) and UV irradiated RR/RRa-P3HT (80%) OFETs.

The device characterization results are consistent with UV–vis and GIWAXS demonstrating that enhanced intermolecular interactions and edge-on orientation of the semiconducting polymer present in UV irradiated RR/RRa-P3HT blend films are responsible for the enhanced charge transport performance. Additionally, the off-current for devices fabricated under ambient was effectively reduced by up to two orders of magnitude as a function of RR/RRa-P3HT weight ratio owing to the large fraction of oxygen-sensitive RR-P3HT having been substituted with insulating RRa-P3HT.

The decreased surface roughness (3.05 to 1.07 nm) observed from AFM imaging might also contribute to this phenomenon. For a top-gate device architecture, underlying semiconductor surface morphology could negatively impact solution deposition of a uniform polymer dielectric layer.[211] While polycrystalline nanostructures may be

favorable for efficient charge carrier transport, the concomitantly increased surface roughness is expected to be detrimental to the insulating properties of dielectrics, resulting in significant leakage currents. Here, the blend approach provides for an essentially featureless RRa-P3HT top surface layer as demonstrated by AFM imaging. The inactive layer may serve as a passivation layer at the semiconductor–dielectric interface for the RR/RRa-P3HT (80%) blend films. The presence of this passivation layer may in turn improve thin film uniformity and insulating properties of the dielectric since most of the semiconducting nanofibrils are concentrated at the film–substrate interface. (Figure 4.5a and b) The superior thin film crystallinity of UV irradiated RR/RRa-P3HT (80%) paired with improved semiconductor–dielectric contact provides for almost ideal forward and backward transfer characteristics with no perceptible hysteresis as shown in Figure 4.7d. Note, all of the flexible OFETs were fabricated under ambient conditions with no surface modification or post thermal annealing.

4.3.6 Mechanical Properties

Compared to rigid inorganic semiconductors and devices, the principal advantage of the organic counterparts is their compatibility with a variety of flexible substrates. To evaluate their mechanical flexibility, the devices fabricated here were subject to tensile stress through a series of bending experiments. The extent of bending was measured by attaching the devices around cylindrical rods with various radii, R, as shown in Figure 4.10a and b. The bending strain (ε) associated with different R can be calculated from the equation, $\varepsilon = D/2R$.[227, 228] The total film thickness (D) was approximated as that of the

PET substrate, 127 μm, since in comparison, the thickness of the device layers is negligible. The bending radii and the corresponding strain values are listed in Table 4-2.

Table 4-2 External strain and corresponding radii of cylindrical rods.

Rod Diameter (in)	N/A	1	5/8	3/8	1/4
Bending Radius (mm)	N/A	12.7	7.9	4.7	3.1
Strain, ε (%)	0	0.5	0.8	1.3	2

In the first set of bending tests, the as-prepared devices were initially characterized in a planar geometry (ε = 0%), followed by bending experiments with different magnitudes of external strain. The UV irradiated RR-P3HT (0%) devices experience a slight decrease in charge transport performance after experiencing some strain (ε = 0.5%). By contrast, charge carrier mobility remained constant for the blend devices with identical hysteresis-free transfer characteristics, even though the external strain was increased up to 2.0% (Figure 4.10a and c). Second, the flexible OFETs were bent repeatedly at a fixed strain. As shown in Figure 4.10b and d, UV irradiated RR/RRa-P3HT (80%) device performance exhibited no significant change after bending 1000 times, and a charge carrier mobility as high as ~0.1 $cm^2 V^{-1} s^{-1}$ was preserved. Generally, superior thin film crystallinity benefits charge carrier transport performance, but concomitantly films can stiffen and be embrittled, leading to performance degradation after large bending strain.[61, 201] Nevertheless, the blends allowed for fabrication of devices that could withstand the bending test performed here. Presumably, the well-ordered RR-P3HT nanofibrils are embedded within amorphous RRa-P3HT matrices, which have a better mechanical compliance.[60] Furthermore, the curved contour path of semiconducting nanofibrils might facilitate the absorption of excessive mechanical stress, resulting in the desirable thin film flexibility.[215]

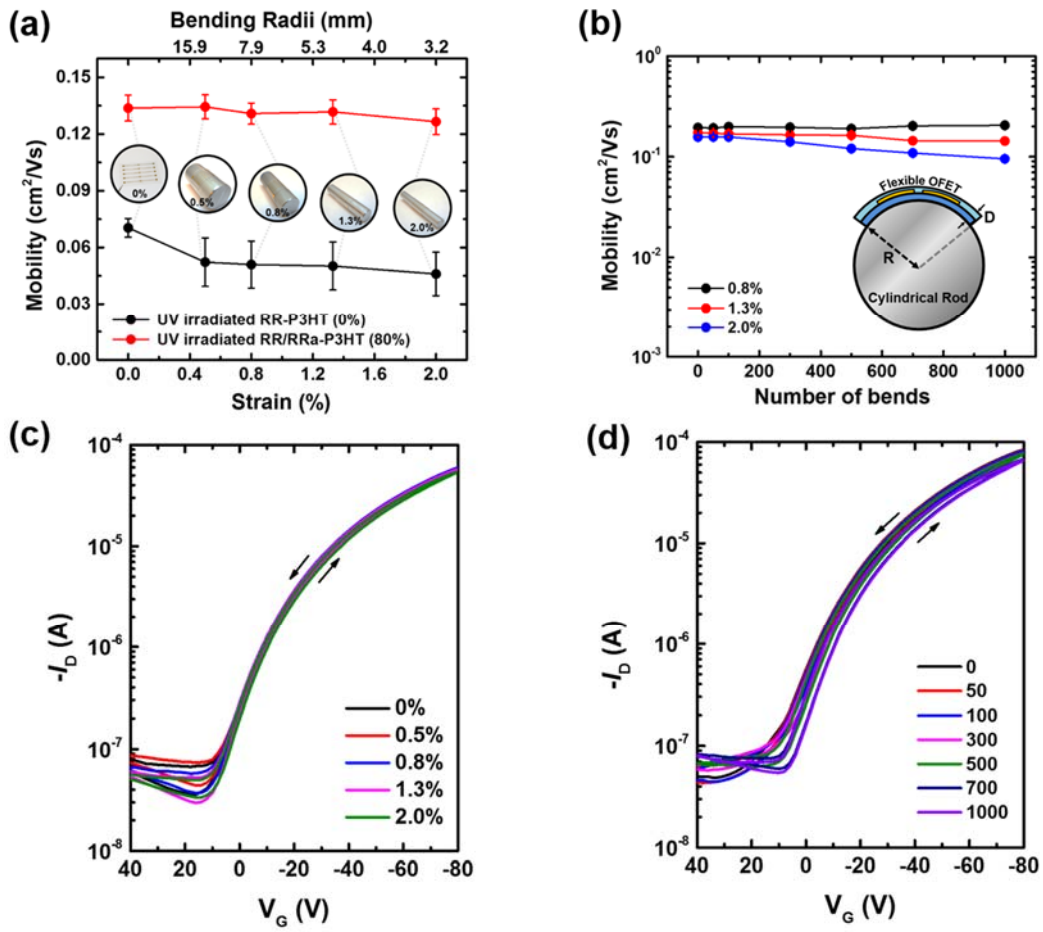

Figure 4.10 Average field-effect mobilities as a function of strain. b) UV irradiated RR/RRa-P3HT (80%) blend OFETs as a function of bending cycles at a fixed strain. Forward and backward transfer characteristics of UV irradiated RR/RRa-P3HT (80%) blend OFETs with different c) external strain, and d) bending cycles at 1.3% strain.

4.3.7 Ambient Stability

For polythiophenes, the extension of effective p-conjugation length can lead to a decreased ionization potential (*IP*), with the resulting higher susceptibility to oxidative doping and short operational lifetime under ambient conditions.[48, 140] Encapsulation of the active layers with insulating polymers or inorganic materials such as SiN_x, Al_2O_3 has

been presented as a promising method to alleviate these issues.[229-231] However, these approaches all require additional processing steps, which increase the complexity of device fabrication and associated production costs. Devices fabricated with top-gate architectures may eliminate the encapsulation steps, because the insulating polymers can serve dual roles, both dielectric and encapsulation layer, thereby preventing oxygen and moisture permeation.

To date, semiconducting/insulating polymer blend thin film device examples which provide for improved mechanical flexibility fabricated in top-gate architectures are limited. Simply, the choice of solution-processed gate dielectric polymers is constrained,[47, 110, 208, 232] and an orthogonal solvent is required to avoid potentially adverse effects on the underlying blend films during deposition.[211, 232] Herein, the UV irradiated RR/RRa-P3HT blend thin film devices were fabricated using the readily available, insulating polymer, PMMA, which served as both the top-gate dielectric and encapsulation layer. In contrast to conventional semiconductor/insulator blends, the insulating component here was RRa-P3HT, which will not be damaged during dielectric deposition steps, and thus the fabrication of top-gate geometry devices was enabled. To explore device ambient stability, all flexible OFETs were stored at ambient conditions, and periodically characterized. For nonencapsulated devices, the as-prepared blend films were first directly exposed to air for a given period of time, and the dielectric and gate electrodes were deposited prior to electrical property measurement. As shown in Figure 4.11a, the charge carrier mobilities of nonencapsulated devices dropped by over a factor of 50 after 360 h, and no measurable mobility was observed for longer storage times. By contrast, the charge transport performance of OFETs self-encapsulated with the dielectric

layer exhibited no appreciable change upon exposure to air for over 700 h (~30 day). These results suggest that the devices are significantly more robust when maintained under ambient conditions (as shown in Figure 4.11a and b).

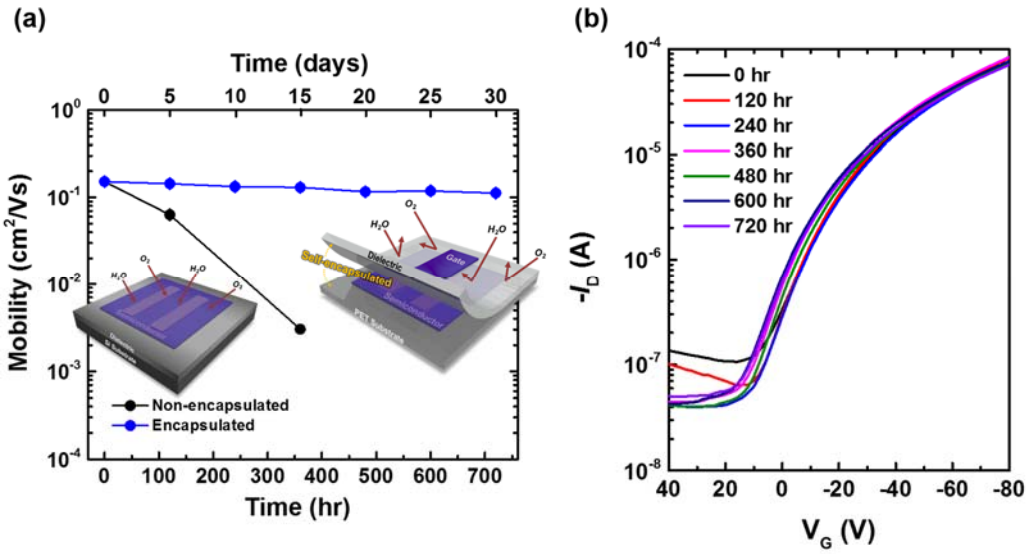

Figure 4.11 (a) Average field-effect mobilities obtained from nonencapsulated and encapsulated UV irradiated RR/RRa-P3HT (80%) blend OFETs as a function of air exposure times. (b) Transfer characteristics of encapsulated UV irradiated RR/RRa-P3HT (80%) blend OFETs with different air exposure times. (V_D = –40 V)

4.4 Conclusions

High performance, flexible field effect transistor devices were demonstrated using UV irradiated RR/RRa-P3HT blend thin films as active layers over PET substrates. Semiconductor supramolecular ordering and crystal orientation were greatly improved when small quantities of UV irradiated RR-P3HT were incorporated into insulating RRa-P3HT matrices. Examination of the surface morphology revealed that the majority of RR-P3HT nanofibrils preferentially grew at the semiconductor–substrate interface, while the

amorphous RRa-P3HT presented mainly at the surface–air interface of the blend films. The molecular self-assembly of RR-P3HT induced by UV irradiation, coupled with additional driving forces associated with unfavorable steric interactions between the RR and RRa components lead to this vertical phase distribution. The profile of the blend films gives rise to a more uniform, smooth surface, and improved film–dielectric interface. These characteristics, in turn, effect enhanced charge carrier transport performance.

Furthermore, the blend thin films are compatible with flexible substrates and well-adapted to high bending strain owing to the mechanical compliance of the amorphous RRa-P3HT matrices and curved contour path of RR-P3HT nanofibrils. In the top-gate geometry, PMMA functions as the dielectric layer and effectively self-encapsulates the device, which helps to extend the device operational lifetime under ambient conditions. The results provided here underscore the value of polymer–polymer blends to achieve efficient, tightly packed, and networked charge conduction pathways for flexible device applications. The systematic investigation of structure–process–property relationships in general, and structure–mechanical/electrical property relationships in particular will lead to efficient and robust devices.

CHAPTER 5. CONCLUSIONS AND RECOMMENDATIONS

5.1 Conclusions

The primary objective of this thesis was to improve P3HT-based OFET performance in terms of charge carrier mobility, threshold voltage, on/off ratio, mechanical flexibility and ambient stability by manipulating the intra/inter-molecular interactions, surface morphology, thin film crystallinity and structure anisotropy. Additionally, device characterization was not only limited to the conventional BGBC configuration, which used rigid silicon as the substrate; but also was extended to the BGTC transistor geometry over a flexible plastic substrate, and thus provided insights into the important roles of both electrical properties and mechanical flexibility in P3HT for future organic electronics development.

The studies described in Chapter 2 elucidate the complex correlations between thin film morphology and macroscopic charge transport properties in polymer-oligomer blends. The charge carrier mobilities strongly depend on the number of grain boundaries and the interconnectivity between ordered domains, which can be tuned and optimized by varying the weight fraction of oligomer. Additionally, the P3HT oxidative doping effect, which is a long-standing issue when processing was conducted under ambient conditions can be diminished, resulting in a substantial decrease in threshold voltage and off-current.

Chapter 3 highlights the significant impact of anisotropic crystalline structure on intra- and intermolecular charge transport. The P3HT nanofiber orientation distribution from totally randomly oriented to long-range aligned structures can be precisely

controlled by the polymer solution-aging time owing to the P3HT time-dependent self-assembly properties. The long-range ordering and highly aligned nanofibrillar thin film structure, which was induced by a blade coating method, provides a platform to quantitatively evaluate the anisotropic charge transport behavior along and across the nanofibers. Interestingly, the results show that the charge transport across the well-aligned P3HT nanofibers was more efficient than along the long-axis of nanofibrillar structures due to enhanced intramolecular charge transport and tie-chains. The facile and scalable solution-coating method investigated here suggests an effective approach to induce anisotropic crystalline structures, which are readily obtained by directly controlling their intrinsic solution properties without the need for extrinsic techniques such as surface templating or shearing blade patterning.

The research works mentioned above were mainly accomplished on a rigid silicon substrate, which is incompatible with flexible applications. Herein, in Chapter 4, high performance fully-flexible OFETs using PET as the substrate and UV irradiated RR/RRa-P3HT blend thin films as the device active layer have been demonstrated for the interrogation of device mechanical flexibility. The resultant devices exhibit remarkable charge carrier mobility even when the blend films comprise only a small fraction of active materials. The underlying mechanism is correlated to molecular self-assembly of RR-P3HT and its unfavorable intermolecular interactions with RRa-P3HT. The transistor performance is retained upon application of high external strain and multiple bending. In addition, the top-gate architecture enables the dielectric to serve as a self-encapsulation layer to protect the underlying semiconductor from atmospheric oxygen and moisture,

resulting in extended ambient device stability. This facile blend approach is expected to be an alternative strategy for the realization of next-generation flexible electronics.

5.2 Recommendations

The main advantages of OSCs are their solution processability, chemical tunability and the potential for flexible and even stretchable device fabrication. As we presented in this thesis, OFET performance can be greatly improved by process optimization, materials design and device geometry modification. In addition, it has been proved that P3HT thin films are compatible with plastic substrates and well-adapted to high bending strain owing to their tunable mechanical compliance, making them a promising candidate for flexible electronic fabrication and roll-to-roll printing processes. However, in order to be applicable to emerging electronics such as wearable device, electronic skins, artificial muscles, smart clothing and soft robots, these organic materials not only require mechanical flexibility but also stretchability. In other words, the deformed films should not experience any significant interconnect fracture, degradation in electrical properties and delamination of components during cyclic loading and stretching.

Previous studies done by O'Connor and coworkers[160] have evaluated the strain tolerance of pristine P3HT films. The results show that the films remain continuous and no cracks can be observed at strains greater than 150%. Recently, Cho and coworkers[233] systematically investigated the electrical characteristics of P3HT nanofibers under a series of unidirectional tensile strains. As shown in Figure 5.1a, the P3HT nanofibrillar networks are randomly distributed and formed a large number of tight junctions, which

are responsible for the severe breakage of nanofibers at high tensile strain. As a result, the strained P3HT nanofibrillar thin films showed an apparent decrease in charge carrier mobility beyond 50% strain (Figure 5.1b). However, in Chapter 3, we have successfully induced macroscopic alignment of P3HT nanofibers (Figure 3.15), which might be a potential solution to alleviate the fiber breaking issues due to minimized fiber junctions. Therefore, the further investigations associated with the correlations between electrical and mechanical properties of these highly-aligned P3HT nanofibers under tensile strain are recommended.

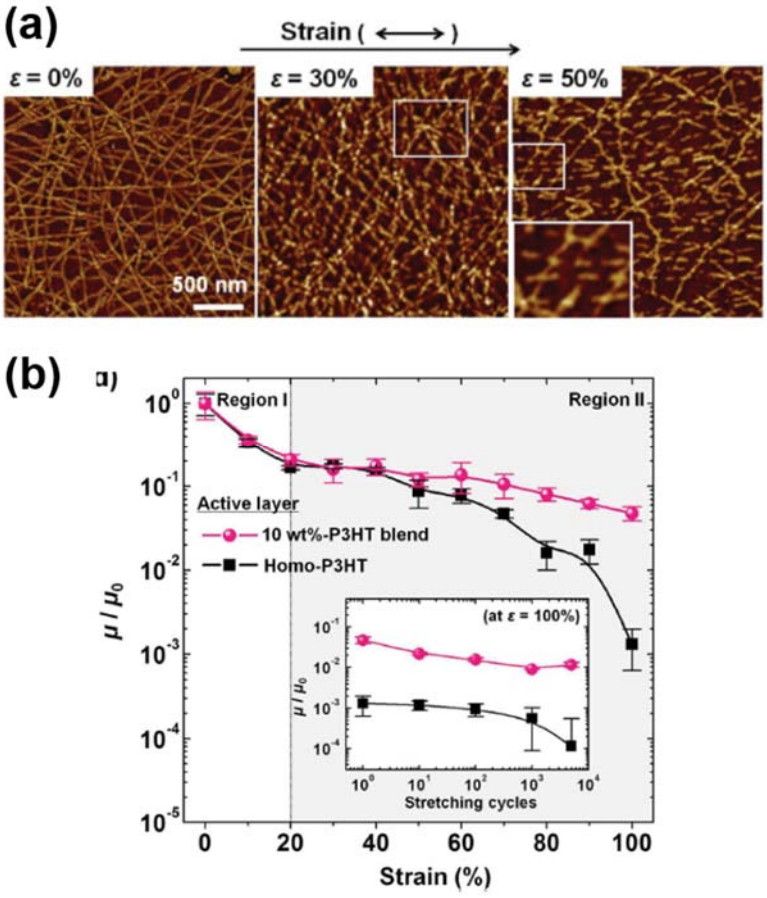

Figure 5.1 (a) AFM phase images of P3HT nanofibers at 0, 30 and 50% strain, respectively. (b) The charge carrier mobility of homo-P3HT and 10 wt% P3HT blend films as a function of tensile strain. The inset show the charge carrier mobility of 100% strained films as a function of stretching cycles.[233]

Figure 5.2 describes the process flow of the lamination approach used to evaluate the mechanical and electrical properties of the P3HT films. First, the blade coated P3HT films were transferred to an elastomeric PDMS slab from a glass substrate. The P3HT/PDMS slabs were subsequently stretched with a certain strain. The corresponding charge transport characteristics were measured by laminating the strained P3HT films onto the prefabricated device substrates.

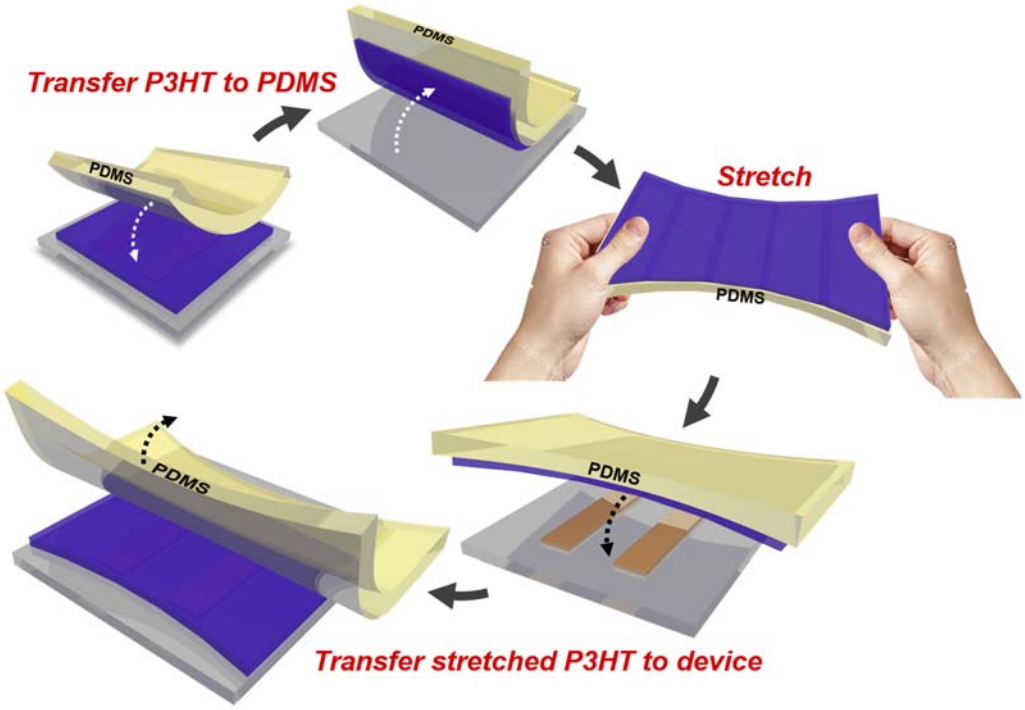

Figure 5.2 The process flow of the lamination approach used to evaluate the mechanical and electrical properties of the P3HT films.

As a preliminary study, the thin film crystallinity of 0 and 100 % strained films with well-aligned nanofibrillar structure was investigated by GIWAXS. Figure 5.3a-b revealed that the 100% strain is found to induce apparent face-on crystal orientation in the randomly distributed nanofibrillar thin films. However, the well-aligned nanofibrillar thin

films remain in an edge-on crystal orientation after the application of 100% strain either parallel or perpendicular to the long axis of nanofibers as shown in Figure 5.3c-e. Accordingly, the large number of fiber junctions that appeared in the randomly distributed nanofibrillar thin films might be responsible for the reoriented crystalline structure. However, more characterization such as surface morphology, photophysical and mechanical properties are required to support this assumption. Besides, the evolution of charge carrier mobility of randomly oriented and highly aligned nanofibrillar thin films as a function of tensile strain should also be evaluated.

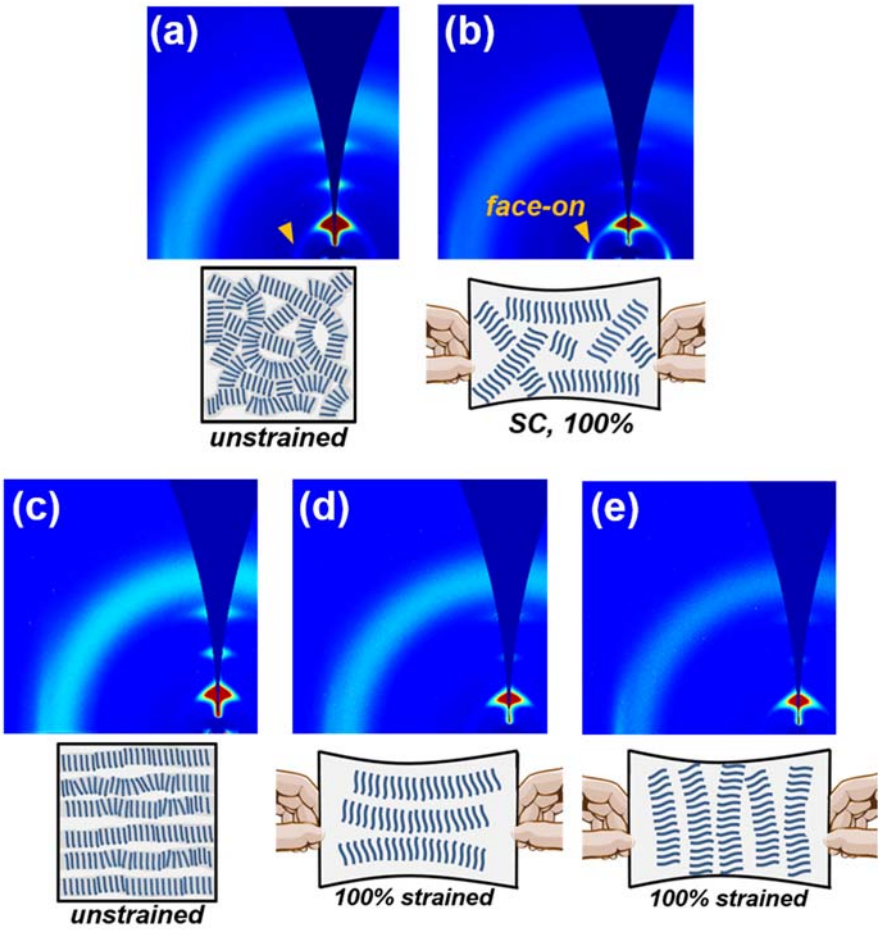

Figure 5.3 GIWAXS of (a) unstrained and (b) 100% strained films with randomly distributed nanofibrillar structure; (c) unstrained aligned film, (d) 100% strain parallel to aligned nanofibers and (e) 100% strained perpendicular to aligned nanofibers.

In addition to the investigation of mechanical stretchability for OSCs, it is equally important to design and develop a fully-stretchable OFET in order to have devices that are compatible with soft and wearable electronic applications as we mentioned above. Figure 5.4 suggested a process flow of the lamination approach used to fabricate OFETs on deformable elastomer with TGBC configuration. The 50 nm Au source and drain electrodes were deposited by e-beam evaporation through a shadow mask onto the PDMS slabs. Next, the resultant Au/PDMS slabs were directly attached to the top of the P3HT thin films, which were pre-deposited on glass substrates. The adhesion difference between PDMS/P3HT and P3HT/glass interfaces facilitates the transfer of P3HT thin films from glass substrates to Au/PDMS slabs. Similarly, the insulating dielectrics, PMMA were subsequently transferred to the P3HT/Au/PDMS from glass substrates. The devices were completed by drop casting the PEDOT:PSS as gate electrodes, which were deposited on the top of PMMA and fully covered the active channel area.

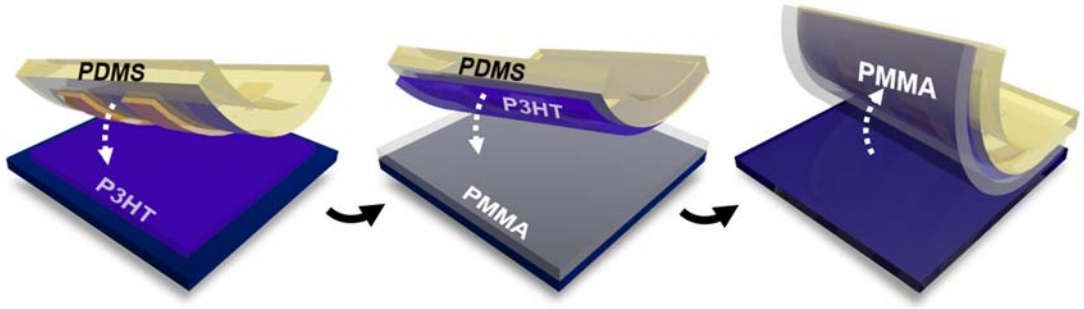

Figure 5.4 The process flow of the lamination approach used to fabricate OFETs on PDMS substrates.

According to the representative transfer curves as shown in Figure 5.5, the devices presented a low V_{Th} and almost ideal forward and backward transfer characteristics with small hysteresis, suggesting that the OFETs were successfully fabricated by using

deformable elastomers, PMMA and PDMS as the dielectric and substrate, respectively. The active layers were deposited by spin coating the pristine P3HT (5 mg mL^{-1}) solutions on to the substrates, resulting in a charge carrier mobility at 1.1×10^{-3} $cm^2 V^{-1} s^{-1}$. Note that this is only preliminary work, and thus many challenges remain to be addressed in order to fabricate fully-stretchable OFETs and evaluate their device performance under high tensile strains. The potential difficulties include: (1) charge carrier mobilities of OSCs are sacrificed with increased mechanical compliance; (2) device performance shows significant degradation upon high tensile stains; (3) poor adhesion between each of the layers; (4) fracture or fatigue of the films caused by extreme deformation or cyclic loading at moderate strains.

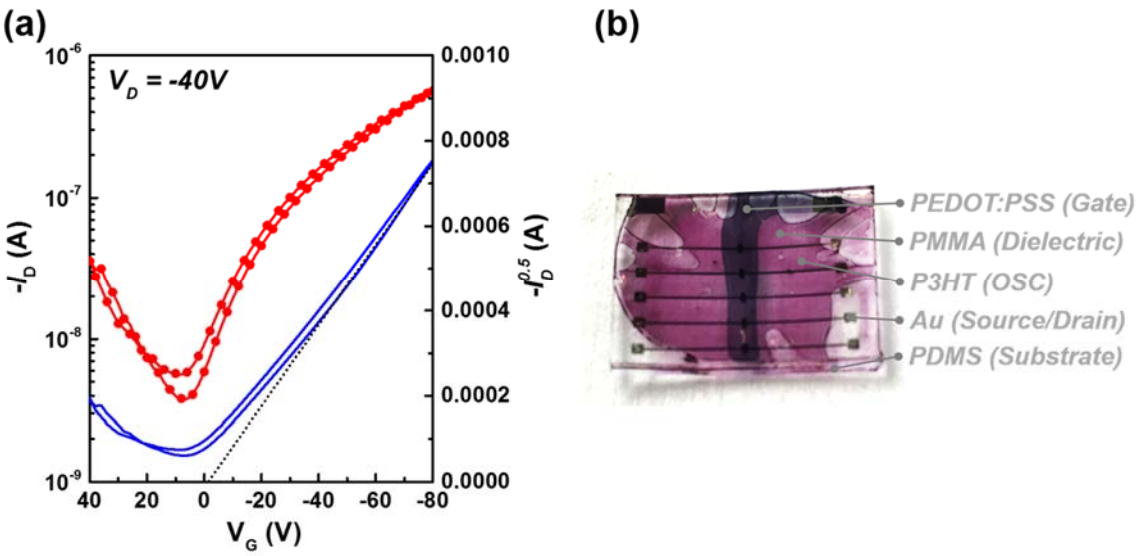

Figure 5.5 (a) Transfer characteristics of OFETs using pristine P3HT as the active layer. (b) OFETs fabricated on PDMS substrate.

REFERENCES

1. Bardeen, J.; Brattain, W. H. The Transistor, A Semi-Conductor Triode. *Phys. Rev.* 1948, 74, 230-231.

2. Salleo, A. Charge transport in polymeric transistors. *Mater. Today* 2007, 10, 38-45.

3. Reuss, R. H.; Chalamala, B. R.; Moussessian, A.; Kane, M. G.; Kumar, A.; Zhang, D. C.; Rogers, J. A.; Hatalis, M.; Temple, D.; Moddel, G.; Eliasson, B. J.; Estes, M. J.; Kunze, J.; Handy, E. S.; Harmon, E. S.; Salzman, D. B.; Woodall, J. M.; Alam, M. A.; Murthy, J. Y.; Jacobsen, S. C.; Olivier, M.; Markus, D.; Campbell, P. M.; Snow, E. Macroelectronics: Perspectives on Technology and Applications. *Proc. IEEE* 2005, 93, 1239-1256.

4. Chalamala, B. R.; Libsch, F. E.; Reuss, R. H.; Gnade, B. E. Scanning the issue - Special issue on flat-panel display technology. *Proc. IEEE* 2002, 90, 447-452.

5. Shirakawa, H.; Louis, E. J.; MacDiarmid, A. G.; Chiang, C. K.; Heeger, A. J. Synthesis of electrically conducting organic polymers: halogen derivatives of polyacetylene, (CH). *J.C.S. Chem.Comm.* 1977, 578-580.

6. Tsumura, A.; Koezuka, H.; Ando, T. Macromolecular electronic device: Field-effect transistor with a polythiophene thin film. *Appl. Phys. Lett.* 1986, 49, 1210-1212.

7. Bell Labs History of The (the "crystal Triode"). *http://www.beatriceco.com/bti/porticus/bell/belllabs_transistor.html* (Accessed February 2017).

8. PolyIC GmbH & Co. KG - Pictures for the Press: Laboratory printing machine. *http://www.polyic.com/press-news-events/pictures-for-the-press.html* (Accessed February 2017).

9. Laaperi, A. OLED lifetime issues from a mobile-phone-industry point of view. *J. Soc. Inf. Disp.* 2008, 16, 1125-1130.

10. Noda, M.; Kobayashi, N.; Katsuhara, M.; Yumoto, A.; Ushikura, S.; Yasuda, R.; Hirai, N.; Yukawa, G.; Yagi, I.; Nomoto, K.; Urabe, T. An OTFT-driven rollable OLED display. *J. Soc. Inf. Disp.* 2011, 19, 316-322.

11. Li, C.-H.; Wang, C.; Keplinger, C.; Zuo, J.-L.; Jin, L.; Sun, Y.; Zheng, P.; Cao, Y.; Lissel, F.; Linder, C.; You, X.-Z.; Bao, Z. A highly stretchable autonomous self-healing elastomer. *Nat. Chem.* 2016, 8, 618-624.

12. Trung, T. Q.; Ramasundaram, S.; Hwang, B.-U.; Lee, N.-E. An All-Elastomeric Transparent and Stretchable Temperature Sensor for Body-Attachable Wearable Electronics. *Adv. Mater.* 2016, 28, 502-509.

13. Nawrocki, R. A.; Matsuhisa, N.; Yokota, T.; Someya, T. 300-nm Imperceptible, Ultraflexible, and Biocompatible e-Skin Fit with Tactile Sensors and Organic Transistors. *Adv. Electron. Mater.* 2016, 2, 1500452.

14. Irimia-Vladu, M.; Troshin, P. A.; Reisinger, M.; Shmygleva, L.; Kanbur, Y.; Schwabegger, G.; Bodea, M.; Schwödiauer, R.; Mumyatov, A.; Fergus, J. W.; Razumov, V. F.; Sitter, H.; Sariciftci, N. S.; Bauer, S. Biocompatible and Biodegradable Materials for Organic Field-Effect Transistors. *Adv. Funct. Mater.* 2010, 20, 4069-4076.

15. Qian, C.; Sun, J.; Yang, J.; Gao, Y. Flexible organic field-effect transistors on biodegradable cellulose paper with efficient reusable ion gel dielectrics. *RSC Adv.* 2015, 5, 14567-14574.

16. Chou, H.-H.; Nguyen, A.; Chortos, A.; To, J. W. F.; Lu, C.; Mei, J.; Kurosawa, T.; Bae, W.-G.; Tok, J. B. H.; Bao, Z. A chameleon-inspired stretchable electronic skin with interactive colour changing controlled by tactile sensing. *Nat. Commun.* 2015, 6.

17. Zang, Y.; Huang, D.; Di, C.-a.; Zhu, D. Device Engineered Organic Transistors for Flexible Sensing Applications. *Adv. Mater.* 2016, 25, 4549-4555.

18. Schwartz, G.; Tee, B. C. K.; Mei, J.; Appleton, A. L.; Kim, D. H.; Wang, H.; Bao, Z. Flexible polymer transistors with high pressure sensitivity for application in electronic skin and health monitoring. *Nat. Commun.* 2013, 4, 1859.

19. Someya, T.; Kato, Y.; Sekitani, T.; Iba, S.; Noguchi, Y.; Murase, Y.; Kawaguchi, H.; Sakurai, T. Conformable, flexible, large-area networks of pressure and thermal sensors with organic transistor active matrixes. *Proc. Natl. Acad. Sci. U.S.A.* 2005, 102, 12321-12325.

20. Yuan, Y.; Giri, G.; Ayzner, A. L.; Zoombelt, A. P.; Mannsfeld, S. C. B.; Chen, J.; Nordlund, D.; Toney, M. F.; Huang, J.; Bao, Z. Ultra-high mobility transparent organic thin film transistors grown by an off-centre spin-coating method. *Nat. Commun.* 2014, 5.

21. Tseng, H.-R.; Phan, H.; Luo, C.; Wang, M.; Perez, L. A.; Patel, S. N.; Ying, L.; Kramer, E. J.; Nguyen, T.-Q.; Bazan, G. C.; Heeger, A. J. High-Mobility Field-Effect Transistors Fabricated with Macroscopic Aligned Semiconducting Polymers. *Adv. Mater.* 2014, 26, 2993-2998.

22. Li, W.; Varlamov, S.; Dore, J.; Green, M. Defect annealing in ultra-thin polycrystalline silicon films on glass: Rapid thermal versus laser processing. *Mater. Lett.* 2013, 107, 1-4.

23. Tojo, Y.; Miura, A.; Ishikawa, Y.; Yamashita, I.; Uraoka, Y. Polycrystalline silicon thin-film transistor utilizing self-assembled monolayer for crystallization. *Thin Solid Films* 2013, 540, 266-270.

24. Kim, S.; Konar, A.; Hwang, W.-S.; Lee, J. H.; Lee, J.; Yang, J.; Jung, C.; Kim, H.; Yoo, J.-B.; Choi, J.-Y.; Jin, Y. W.; Lee, S. Y.; Jena, D.; Choi, W.; Kim, K. High-mobility and low-power thin-film transistors based on multilayer MoS2 crystals. *Nat. Commun.* 2012, 3, 1011.

25. Thomas, S. R.; Pattanasattayavong, P.; Anthopoulos, T. D. Solution-processable metal oxide semiconductors for thin-film transistor applications. *Chem. Soc. Rev.* 2013, 42, 6910-6923.

26. Kim, M.; Jeong, J. H.; Lee, H. J.; Ahn, T. K.; Shin, H. S.; Park, J.-S.; Jeong, J. K.; Mo, Y.-G.; Kim, H. D. High mobility bottom gate InGaZnO thin film transistors with SiOx etch stopper. *Appl. Phys. Lett.* 2007, 90, 212114.

27. Aikawa, S.; Nabatame, T.; Tsukagoshi, K. Effects of dopants in InOx-based amorphous oxide semiconductors for thin-film transistor applications. *Appl. Phys. Lett.* 2013, 103, 172105.

28. Dai, M.-K.; Lian, J.-T.; Lin, T.-Y.; Chen, Y.-F. High-performance transparent and flexible inorganic thin film transistors: a facile integration of graphene nanosheets and amorphous InGaZnO. *J. Mater. Chem. C* 2013, 1, 5064-5071.

29. Yang, H.; Shin, T. J.; Yang, L.; Cho, K.; Ryu, C. Y.; Bao, Z. Effect of Mesoscale Crystalline Structure on the Field-Effect Mobility of Regioregular Poly(3-hexyl thiophene) in Thin-Film Transistors. *Adv. Funct. Mater.* 2005, 15, 671-676.

30. Lim, J. A.; Liu, F.; Ferdous, S.; Muthukumar, M.; Briseno, A. L. Polymer semiconductor crystals. *Mater. Today* 2010, 13, 14-24.

31. O'Connor, B. T.; Reid, O. G.; Zhang, X.; Kline, R. J.; Richter, L. J.; Gundlach, D. J.; DeLongchamp, D. M.; Toney, M. F.; Kopidakis, N.; Rumbles, G. Morphological Origin of Charge Transport Anisotropy in Aligned Polythiophene Thin Films. *Adv. Funct. Mater.* 2014, 24, 3422-3431.

32. Zhang, X.; Jie, J.; Deng, W.; Shang, Q.; Wang, J.; Wang, H.; Chen, X.; Zhang, X. Alignment and Patterning of Ordered Small-Molecule Organic Semiconductor Micro-/Nanocrystals for Device Applications. *Adv. Mater.* 2016, 28, 2475–2503.

33. Jimison, L. H.; Toney, M. F.; McCulloch, I.; Heeney, M.; Salleo, A. Charge-Transport Anisotropy Due to Grain Boundaries in Directionally Crystallized Thin Films of Regioregular Poly(3-hexylthiophene). *Adv. Mater.* 2009, 21, 1568-1572.

34. Kelley, T. W.; Frisbie, C. D. Gate Voltage Dependent Resistance of a Single Organic Semiconductor Grain Boundary. *J. Phys. Chem. B* 2001, 105, 4538-4540.

35. Chang, M.; Choi, D.; Fu, B.; Reichmanis, E. Solvent Based Hydrogen Bonding: Impact on Poly(3-hexylthiophene) Nanoscale Morphology and Charge Transport Characteristics. *Acs Nano* 2013, 7, 5402-5413.

36. Hu, H.; Zhao, K.; Fernandes, N.; Boufflet, P.; Bannock, J. H.; Yu, L.; de Mello, J. C.; Stingelin, N.; Heeney, M.; Giannelis, E. P.; Amassian, A. Entanglements in marginal solutions: a means of tuning pre-aggregation of conjugated polymers with positive implications for charge transport. *J. Mater. Chem. C* 2015, 3, 7394-7404.

37. Bao, Z.; Dodabalapur, A.; Lovinger, A. J. Soluble and processable regioregular poly(3-hexylthiophene) for thin film field-effect transistor applications with high mobility. *Appl. Phys. Lett.* 1996, 69, 4108.

38. Choi, D.; Chang, M.; Reichmanis, E. Controlled Assembly of Poly(3-hexylthiophene): Managing the Disorder to Order Transition on the Nano- through Meso-Scales. *Adv. Funct. Mater.* 2014, 25, 920-927.

39. Lee, W.-Y.; Giri, G.; Diao, Y.; Tassone, C. J.; Matthews, J. R.; Sorensen, M. L.; Mannsfeld, S. C. B.; Chen, W.-C.; Fong, H. H.; Tok, J. B. H.; Toney, M. F.; He, M.; Bao, Z. Effect of Non-Chlorinated Mixed Solvents on Charge Transport and Morphology of Solution-Processed Polymer Field-Effect Transistors. *Adv. Funct. Mater.* 2014, 24, 3524-3534.

40. Park, Y. D.; Lee, H. S.; Choi, Y. J.; Kwak, D.; Cho, J. H.; Lee, S.; Cho, K. Solubility-Induced Ordered Polythiophene Precursors for High-Performance Organic Thin-Film Transistors. *Adv. Funct. Mater.* 2009, 19, 1200-1206.

41. Cho, I.; Park, S. K.; Kang, B.; Chung, J. W.; Kim, J. H.; Cho, K.; Park, S. Y. Design, Synthesis, and Versatile Processing of Indolo[3,2-b]indole-Based π-Conjugated Molecules for High-Performance Organic Field-Effect Transistors. *Adv. Funct. Mater.* 2016, 26, 2966-2973.

42. Padma, N.; Maheshwari, P.; Bhattacharya, D.; Tokas, R. B.; Sen, S.; Honda, Y.; Basu, S.; Pujari, P. K.; Rao, T. V. C. Investigations on Substrate Temperature-Induced Growth Modes of Organic Semiconductors at Dielectric/semiconductor Interface and Their Correlation with Threshold Voltage Stability in Organic Field-Effect Transistors. *ACS Appl. Mater. Interfaces* 2016, 8, 3376-3385.

43. Sarcletti, M.; Schmaltz, T.; Halik, M. The mutual influence of surface energy and substrate temperature on the saturation mobility in organic semiconductors. *Org. Electron.* 2014, 15, 3082-3086.

44. Oh, J. Y.; Lee, T. I.; Myoung, J.-M.; Jeong, U.; Baik, H. K. Coating on a Cold Substrate Largely Enhances Power Conversion Efficiency of the Bulk Heterojunction Solar Cell. *Macromol. Rapid Commun.* 2011, 32, 1066-1071.

45. Abdou, M. S. A.; Orfino, F. P.; Xie, Z. W.; Deen, M. J.; Holdcroft, S. Reversible charge transfer complexes between molecular oxygen and poly(3-alkylthiophene)s. *Adv. Mater.* 1994, 6, 838-841.

46. Cook, S.; Furube, A.; Katoh, R. Matter of minutes degradation of poly(3-hexylthiophene) under illumination in air. *J. Mater. Chem.* 2012, 22, 4282-4289.

47. Lu, G.; Blakesley, J.; Himmelberger, S.; Pingel, P.; Frisch, J.; Lieberwirth, I.; Salzmann, I.; Oehzelt, M.; Di Pietro, R.; Salleo, A.; Koch, N.; Neher, D. Moderate doping leads to high performance of semiconductor/insulator polymer blend transistors. *Nat. Commun.* 2013, 4, 1588.

48. Hoshino, S.; Yoshida, M.; Uemura, S.; Kodzasa, T.; Takada, N.; Kamata, T.; Yase, K. Influence of moisture on device characteristics of polythiophene-based field-effect transistors. *J. Appl. Phys.* 2004, 95, 5088-5093.

49. Sekitani, T.; Someya, T. Stretchable, Large-area Organic Electronics. *Adv. Mater.* 2010, 22, 2228-2246.

50. Lee, S.; Reuveny, A.; Reeder, J.; Lee, S.; Jin, H.; Liu, Q.; Yokota, T.; Sekitani, T.; Isoyama, T.; Abe, Y.; Suo, Z.; Someya, T. A transparent bending-insensitive pressure sensor. *Nat. Nanotechnol.* 2016, 11, 472-478.

51. Masatoshi, K.; Yasuhiko, A. Pentacene-based organic field-effect transistors. *J. Phys. Condens. Matter* 2008, 20, 184011.

52. Lin, Y. Y.; Gundlach, D. J.; Nelson, S. F.; Jackson, T. N. Stacked pentacene layer organic thin-film transistors with improved characteristics. *IEEE Electron Device Lett.* 1997, 18, 606-608.

53. Tatsuo, H.; Jun, T. Organic field-effect transistors using single crystals. *Sci. Tech. Adv. Mater.* 2009, 10, 024314.

54. Reese, C.; Bao, Z. Organic single-crystal field-effect transistors. *Mater. Today* 2007, 10, 20-27.

55. Takimiya, K.; Ebata, H.; Sakamoto, K.; Izawa, T.; Otsubo, T.; Kunugi, Y. 2,7-Diphenyl[1]benzothieno[3,2-b]benzothiophene, A New Organic Semiconductor for Air-Stable Organic Field-Effect Transistors with Mobilities up to 2.0 cm2 V-1 s-1. *J. Am. Chem. Soc.* 2006, 128, 12604-12605.

56. Yamamoto, T.; Takimiya, K. Facile Synthesis of Highly π-Extended Heteroarenes, Dinaphtho[2,3-b:2‘,3‘-f]chalcogenopheno[3,2-b]chalcogenophenes, and Their Application to Field-Effect Transistors. *J. Am. Chem. Soc.* 2007, 129, 2224-2225.

57. Anthony, J. E.; Eaton, D. L.; Parkin, S. R. A Road Map to Stable, Soluble, Easily Crystallized Pentacene Derivatives. *Org. Lett.* 2001, 4, 15-18.

58. Sheraw, C. D.; Jackson, T. N.; Eaton, D. L.; Anthony, J. E. Functionalized Pentacene Active Layer Organic Thin-Film Transistors. *Adv. Mater.* 2003, 15, 2009-2011.

59. Nakayama, K.; Hirose, Y.; Soeda, J.; Yoshizumi, M.; Uemura, T.; Uno, M.; Li, W.; Kang, M. J.; Yamagishi, M.; Okada, Y.; Miyazaki, E.; Nakazawa, Y.; Nakao, A.;

Takimiya, K.; Takeya, J. Patternable Solution-Crystallized Organic Transistors with High Charge Carrier Mobility. *Adv. Mater.* 2011, 23, 1626-1629.

60. Kim, J.-S.; Kim, J.-H.; Lee, W.; Yu, H.; Kim, H. J.; Song, I.; Shin, M.; Oh, J. H.; Jeong, U.; Kim, T.-S.; Kim, B. J. Tuning Mechanical and Optoelectrical Properties of Poly(3-hexylthiophene) through Systematic Regioregularity Control. *Macromolecules* 2015, 48, 4339-4346.

61. O'Connor, B.; Chan, E. P.; Chan, C.; Conrad, B. R.; Richter, L. J.; Kline, R. J.; Heeney, M.; McCulloch, I.; Soles, C. L.; DeLongchamp, D. M. Correlations between Mechanical and Electrical Properties of Polythiophenes. *Acs Nano* 2010, 4, 7538-7544.

62. Savagatrup, S.; Makaram, A. S.; Burke, D. J.; Lipomi, D. J. Mechanical Properties of Conjugated Polymers and Polymer-Fullerene Composites as a Function of Molecular Structure. *Adv. Funct. Mater.* 2014, 24, 1169-1181.

63. Bruner, C.; Dauskardt, R. Role of Molecular Weight on the Mechanical Device Properties of Organic Polymer Solar Cells. *Macromolecules* 2014, 47, 1117-1121.

64. Said, E. Electrolyte-Semiconductor Combinations for Organic Electronic Devices. *http://swepub.kb.se/bib/swepub:oai:DiVA.org:liu-15775?tab2=abs&language=en* 2009, Linköping : Linköping University Electronic Press.

65. Wan, M. Conducting Polymers with Micro or Nanometer Strucutre. *Springer* 2008.

66. Rehahn, M. Elektrisch leitfähige Kunststoffe: Der Weg zu einer neuen Materialklasse. *Chem. unserer Zeit* 2003, 37, 18-30.

67. Bao, Z.; Locklin, J. Organic Field-Effect Transistors. *CRC Press* 2007.

68. Brédas, J. L.; Calbert, J. P.; da Silva Filho, D. A.; Cornil, J. Organic semiconductors: A theoretical characterization of the basic parameters governing charge transport. *Proc. Natl. Acad. Sci. U.S.A.* 2002, 99, 5804-5809.

69. Marcus, R. A. Electron transfer reactions in chemistry. Theory and experiment. *Rev. Mod. Phys.* 1993, 65, 599-610.

70. Coropceanu, V.; Cornil, J.; da Silva Filho, D. A.; Olivier, Y.; Silbey, R.; Brédas, J.-L. Charge Transport in Organic Semiconductors. *Chem. Rev.* 2007, 107, 926-952.

71. Brédas, J.-L.; Beljonne, D.; Coropceanu, V.; Cornil, J. Charge-Transfer and Energy-Transfer Processes in π-Conjugated Oligomers and Polymers: A Molecular Picture. *Chem. Rev.* 2004, 104, 4971-5004.

72. Feng, X.; Marcon, V.; Pisula, W.; Hansen, M. R.; Kirkpatrick, J.; Grozema, F.; Andrienko, D.; Kremer, K.; Mullen, K. Towards high charge-carrier mobilities by

rational design of the shape and periphery of discotics. *Nat. Mater.* 2009, 8, 421-426.

73. Atahan-Evrenk, Ş.; Aspuru-Guzik, A. Prediction and Calculation of Crystal Structures. *Springer* 2014.

74. Sirringhaus, H.; Brown, P. J.; Friend, R. H.; Nielsen, M. M.; Bechgaard, K.; Langeveld-Voss, B. M. W.; Spiering, A. J. H.; Janssen, R. A. J.; Meijer, E. W.; Herwig, P.; de Leeuw, D. M. Two-dimensional charge transport in self-organized, high-mobility conjugated polymers. *Nature* 1999, 401, 685-688.

75. Skrypnychuk, V.; Wetzelaer, G.-J. A. H.; Gordiichuk, P. I.; Mannsfeld, S. C. B.; Herrmann, A.; Toney, M. F.; Barbero, D. R. Ultrahigh Mobility in an Organic Semiconductor by Vertical Chain Alignment. *Adv. Mater.* 2016, 28, 2359–2366.

76. Reese, C.; Bao, Z. High-Resolution Measurement of the Anisotropy of Charge Transport in Single Crystals. *Adv. Mater.* 2007, 19, 4535-4538.

77. Braga, D.; Horowitz, G. High-Performance Organic Field-Effect Transistors. *Adv. Mater.* 2009, 21, 1473-1486.

78. Kline, R. J.; McGehee, M. D. Morphology and Charge Transport in Conjugated Polymers. *J. Macromol. Sci. Polymer Rev.* 2006, 46, 27-45.

79. Newman, C. R.; Frisbie, C. D.; da Silva, D. A.; Bredas, J. L.; Ewbank, P. C.; Mann, K. R. Introduction to organic thin film transistors and design of n-channel organic semiconductors. *Chem. Mater.* 2004, 16, 4436-4451.

80. Klauk, H. Organic thin-film transistors. *Chem. Soc. Rev.* 2010, 39, 2643-2666.

81. Singh, T. B.; Meghdadi, F.; Günes, S.; Marjanovic, N.; Horowitz, G.; Lang, P.; Bauer, S.; Sariciftci, N. S. High-Performance Ambipolar Pentacene Organic Field-Effect Transistors on Poly(vinyl alcohol) Organic Gate Dielectric. *Adv. Mater.* 2005, 17, 2315-2320.

82. Zaumseil, J.; Sirringhaus, H. Electron and Ambipolar Transport in Organic Field-Effect Transistors. *Chem. Rev.* 2007, 107, 1296-1323.

83. Xu, X.; Xiao, T.; Gu, X.; Yang, X.; Kershaw, S. V.; Zhao, N.; Xu, J.; Miao, Q. Solution-Processed Ambipolar Organic Thin-Film Transistors by Blending p- and n-Type Semiconductors: Solid Solution versus Microphase Separation. *ACS Appl. Mater. Interfaces* 2015.

84. Babel, A.; Jenekhe, S. A. Alkyl chain length dependence of the field-effect carrier mobility in regioregular poly(3-alkylthiophene)s. *Synth. Met.* 2005, 148, 169-173.

85. Dag, S.; Wang, L.-W. Packing Structure of Poly(3-hexylthiophene) Crystal: Ab Initio and Molecular Dynamics Studies. *J. Phys. Chem. B* 2010, 114, 5997-6000.

86. Merlo, J. A.; Frisbie, C. D. Field Effect Transport and Trapping in Regioregular Polythiophene Nanofibers. *J. Phys. Chem. B* 2004, 108, 19169-19179.

87. Turner, S. T.; Pingel, P.; Steyrleuthner, R.; Crossland, E. J. W.; Ludwigs, S.; Neher, D. Quantitative Analysis of Bulk Heterojunction Films Using Linear Absorption Spectroscopy and Solar Cell Performance. *Adv. Funct. Mater.* 2011, 21, 4640-4652.

88. Heffner, G. W.; Pearson, D. S. Molecular characterization of poly(3-hexylthiophene). *Macromolecules* 1991, 24, 6295-6299.

89. Kline, R. J.; McGehee, M. D.; Kadnikova, E. N.; Liu, J.; Fréchet, J. M. J. Controlling the Field-Effect Mobility of Regioregular Polythiophene by Changing the Molecular Weight. *Adv. Mater.* 2003, 15, 1519-1522.

90. Kline, R. J.; McGehee, M. D.; Kadnikova, E. N.; Liu, J.; Fréchet, J. M. J.; Toney, M. F. Dependence of Regioregular Poly(3-hexylthiophene) Film Morphology and Field-Effect Mobility on Molecular Weight. *Macromolecules* 2005, 38, 3312-3319.

91. Himmelberger, S.; Vandewal, K.; Fei, Z.; Heeney, M.; Salleo, A. Role of Molecular Weight Distribution on Charge Transport in Semiconducting Polymers. *Macromolecules* 2014, 47, 7151-7157.

92. Zen, A.; Pflaum, J.; Hirschmann, S.; Zhuang, W.; Jaiser, F.; Asawapirom, U.; Rabe, J. P.; Scherf, U.; Neher, D. Effect of Molecular Weight and Annealing of Poly(3-hexylthiophene)s on the Performance of Organic Field-Effect Transistors. *Adv. Funct. Mater.* 2004, 14, 757-764.

93. Aiyar, A. R.; Hong, J.-I.; Reichmanis, E. Regioregularity and Intrachain Ordering: Impact on the Nanostructure and Charge Transport in Two-Dimensional Assemblies of Poly(3-hexylthiophene). *Chem. Mater.* 2012, 24, 2845-2853.

94. Willot, P.; Steverlynck, J.; Moerman, D.; Leclere, P.; Lazzaroni, R.; Koeckelberghs, G. Poly(3-alkylthiophene) with tuneable regioregularity: synthesis and self-assembling properties. *Polym. Chem.* 2013, 4, 2662-2671.

95. Snyder, C. R.; Henry, J. S.; DeLongchamp, D. M. Effect of Regioregularity on the Semicrystalline Structure of Poly(3-hexylthiophene). *Macromolecules* 2011, 44, 7088-7091.

96. Woo, C. H.; Thompson, B. C.; Kim, B. J.; Toney, M. F.; Fréchet, J. M. J. The Influence of Poly(3-hexylthiophene) Regioregularity on Fullerene-Composite Solar Cell Performance. *J. Am. Chem. Soc.* 2008, 130, 16324-16329.

97. Shyam S. Pandey; Wataru Takashima; Shuichi Nagamatsu; Takeshi Endo; Masahiro Rikukawa; Keiichi Kaneto. Regioregularity vs Regiorandomness: Effect on Photocarrier Transport in Poly(3-hexylthiophene). *Jpn. J. Appl. Phys.* 2000, 39, L94.

98. Lan, Y.-K.; Huang, C.-I. Charge Mobility and Transport Behavior in the Ordered and Disordered States of the Regioregular Poly(3-hexylthiophene). *J. Phys. Chem. B* 2009, 113, 14555-14564.

99. Kim, Y.; Cook, S.; Tuladhar, S. M.; Choulis, S. A.; Nelson, J.; Durrant, J. R.; Bradley, D. D. C.; Giles, M.; McCulloch, I.; Ha, C.-S.; Ree, M. A strong regioregularity effect in self-organizing conjugated polymer films and high-efficiency polythiophene:fullerene solar cells. *Nat. Mater.* 2006, 5, 197-203.

100. Zade, S. S.; Bendikov, M. Twisting of Conjugated Oligomers and Polymers: Case Study of Oligo- and Polythiophene. *Chem. Eur. J.* 2007, 13, 3688-3700.

101. Brédas, J. L.; Street, G. B.; Thémans, B.; André, J. M. Organic polymers based on aromatic rings (polyparaphenylene, polypyrrole, polythiophene): Evolution of the electronic properties as a function of the torsion angle between adjacent rings. *J. Chem. Phys.* 1985, 83, 1323-1329.

102. Mauer, R.; Kastler, M.; Laquai, F. The Impact of Polymer Regioregularity on Charge Transport and Efficiency of P3HT:PCBM Photovoltaic Devices. *Adv. Funct. Mater.* 2010, 20, 2085-2092.

103. Chang, J.-F.; Sun, B.; Breiby, D. W.; Nielsen, M. M.; Sölling, T. I.; Giles, M.; McCulloch, I.; Sirringhaus, H. Enhanced Mobility of Poly(3-hexylthiophene) Transistors by Spin-Coating from High-Boiling-Point Solvents. *Chem. Mater.* 2004, 16, 4772-4776.

104. Horii, Y.; Ikawa, M.; Sakaguchi, K.; Chikamatsu, M.; Yoshida, Y.; Azumi, R.; Mogi, H.; Kitagawa, M.; Konishi, H.; Yase, K. Investigation of self-assembled monolayer treatment on SiO2 gate insulator of poly(3-hexylthiophene) thin-film transistors. *Thin Solid Films* 2009, 518, 642-646.

105. Kanai, K.; Miyazaki, T.; Suzuki, H.; Inaba, M.; Ouchi, Y.; Seki, K. Effect of annealing on the electronic structure of poly(3-hexylthiophene) thin film. *Phys. Chem. Chem. Phys.* 2010, 12, 273-282.

106. Di, C.-a.; Lu, K.; Zhang, L.; Liu, Y.; Guo, Y.; Sun, X.; Wen, Y.; Yu, G.; Zhu, D. Solvent-Assisted Re-annealing of Polymer Films for Solution-Processable Organic Field-Effect Transistors. *Advanced Materials* 2010, 22, 1273-1277.

107. Aiyar, A. R.; Hong, J. I.; Nambiar, R.; Collard, D. M.; Reichmanis, E. Tunable Crystallinity in Regioregular Poly(3-Hexylthiophene) Thin Films and Its Impact on Field Effect Mobility. *Adv. Funct. Mater.* 2011, 21, 2652-2659.

108. Kim, B.-G.; Kim, M.-S.; Kim, J. Ultrasonic-Assisted Nanodimensional Self-Assembly of Poly-3-hexylthiophene for Organic Photovoltaic Cells. *Acs Nano* 2010, 4, 2160-2166.

109. Qiu, L.; Lim, J. A.; Wang, X.; Lee, W. H.; Hwang, M.; Cho, K. Versatile Use of Vertical-Phase-Separation-Induced Bilayer Structures in Organic Thin-Film Transistors. *Adv. Mater.* 2008, 20, 1141-1145.

110. Qiu, L.; Lee, W. H.; Wang, X.; Kim, J. S.; Lim, J. A.; Kwak, D.; Lee, S.; Cho, K. Organic Thin-film Transistors Based on Polythiophene Nanowires Embedded in Insulating Polymer. *Adv. Mater.* 2009, 21, 1349-1353.

111. Kleinhenz, N.; Rosu, C.; Chatterjee, S.; Chang, M.; Nayani, K.; Xue, Z.; Kim, E.; Middlebrooks, J.; Russo, P. S.; Park, J. O.; Srinivasarao, M.; Reichmanis, E. Liquid Crystalline Poly(3-hexylthiophene) Solutions Revisited: Role of Time-Dependent Self-Assembly. *Chem. Mater.* 2015.

112. Chang, M.; Lee, J.; Kleinhenz, N.; Fu, B.; Reichmanis, E. Photoinduced Anisotropic Supramolecular Assembly and Enhanced Charge Transport of Poly(3-hexylthiophene) Thin Films. *Adv. Funct. Mater.* 2014, 24, 4457-4465.

113. Søndergaard, R.; Hösel, M.; Angmo, D.; Larsen-Olsen, T. T.; Krebs, F. C. Roll-to-roll fabrication of polymer solar cells. *Mater. Today* 2012, 15, 36-49.

114. Cantatore, E.; Geuns, T. C. T.; Gelinck, G. H.; van Veenendaal, E.; Gruijthuijsen, A. F. A.; Schrijnemakers, L.; Drews, S.; de Leeuw, D. M. A 13.56-MHz RFID System Based on Organic Transponders. *IEEE J. Solid-State Circuits* 2007, 42, 84-92.

115. Ji, D.; Jiang, L.; Cai, X.; Dong, H.; Meng, Q.; Tian, G.; Wu, D.; Li, J.; Hu, W. Large scale, flexible organic transistor arrays and circuits based on polyimide materials. *Org. Electron.* 2013, 14, 2528-2533.

116. Hammock, M. L.; Knopfmacher, O.; Ng, T. N.; Tok, J. B. H.; Bao, Z. Electronic Readout Enzyme-Linked Immunosorbent Assay with Organic Field-Effect Transistors as a Preeclampsia Prognostic. *Adv. Mater.* 2014, 26, 6138-6144.

117. Wie, J. J.; Nguyen, N. A.; Cwalina, C. D.; Liu, J.; Martin, D. C.; Mackay, M. E. Shear-Induced Solution Crystallization of Poly(3-hexylthiophene) (P3HT). *Macromolecules* 2014, 47, 3343-3349.

118. Aiyar, A. R.; Hong, J. I.; Izumi, J.; Choi, D.; Kleinhenz, N.; Reichmanis, E. Ultrasound-Induced Ordering in Poly(3-hexylthiophene): Role of Molecular and Process Parameters on Morphology and Charge Transport. *ACS Appl. Mater. Interfaces* 2013, 5, 2368-77.

119. Zhang, L.; Colella, N. S.; Liu, F.; Trahan, S.; Baral, J. K.; Winter, H. H.; Mannsfeld, S. C. B.; Briseno, A. L. Synthesis, Electronic Structure, Molecular Packing/Morphology Evolution, and Carrier Mobilities of Pure Oligo-/Poly(alkylthiophenes). *J. Am. Chem. Soc.* 2013, 135, 844-854.

120. Smith, J.; Hamilton, R.; McCulloch, I.; Stingelin-Stutzmann, N.; Heeney, M.; Bradley, D. D. C.; Anthopoulos, T. D. Solution-processed organic transistors based on semiconducting blends. *J. Mater. Chem.* 2010, 20, 2562-2574.

121. Russell, D. M.; Newsome, C. J.; Li, S. P.; Kugler, T.; Ishida, M.; Shimoda, T. Blends of semiconductor polymer and small molecular crystals for improved-performance thin-film transistors. *Appl. Phys. Lett.* 2005, 87, 222109.

122. Orgiu, E.; Masillamani, A. M.; Vogel, J.-O.; Treossi, E.; Kiersnowski, A.; Kastler, M.; Pisula, W.; Dotz, F.; Palermo, V.; Samori, P. Enhanced mobility in P3HT-based OTFTs upon blending with a phenylene-thiophene-thiophene-phenylene small molecule. *Chem. Commun.* 2012, 48, 1562-1564.

123. Mansouri, S.; Mir, L. E.; Al-Ghamdi, A. A.; Al-Hartomy, O. A.; Said, S. A. F. A.; Yakuphanoglu, F. Characterization and modeling of TIPS-pentacene-poly(3-hexyl) thiophene blend organic thin film transistor. *Synth. Met.* 2013, 185–186, 153-158.

124. El Gemayel, M.; Narita, A.; Dossel, L. F.; Sundaram, R. S.; Kiersnowski, A.; Pisula, W.; Hansen, M. R.; Ferrari, A. C.; Orgiu, E.; Feng, X.; Mullen, K.; Samori, P. Graphene nanoribbon blends with P3HT for organic electronics. *Nanoscale* 2014, 6, 6301-6314.

125. Zhang, L.; Liu, F.; Diao, Y.; Marsh, H. S.; Colella, N. S.; Jayaraman, A.; Russell, T. P.; Mannsfeld, S. C. B.; Briseno, A. L. The Good Host: Formation of Discrete 1-D Fullerene "Channels" in Well-Ordered poly(2,5-bis(3-alkylthiophen-2-yl)thieno[3,2-b]thiophene) Oligomers. *J. Am. Chem. Soc.* 2014, 136, 18120–18130.

126. Wu, P.-T.; Xin, H.; Kim, F. S.; Ren, G.; Jenekhe, S. A. Regioregular Poly(3-pentylthiophene): Synthesis, Self-Assembly of Nanowires, High-Mobility Field-Effect Transistors, and Efficient Photovoltaic Cells. *Macromolecules* 2009, 42, 8817-8826.

127. Berson, S.; De Bettignies, R.; Bailly, S.; Guillerez, S. Poly(3-hexylthiophene) Fibers for Photovoltaic Applications. *Adv. Funct. Mater.* 2007, 17, 1377-1384.

128. Rughooputh, S. D. D. V.; Hotta, S.; Heeger, A. J.; Wudl, F. Chromism of soluble polythienylenes. *J. Polym. Sci. Part B Polym. Phys.* 1987, 25, 1071-1078.

129. Abdelsamie, M.; Zhao, K.; Niazi, M. R.; Chou, K. W.; Amassian, A. In situ UV-visible absorption during spin-coating of organic semiconductors: a new probe for organic electronics and photovoltaics. *J. Mater. Chem. C* 2014, 2, 3373-3381.

130. Brown, P.; Thomas, D.; Köhler, A.; Wilson, J.; Kim, J.-S.; Ramsdale, C.; Sirringhaus, H.; Friend, R. Effect of interchain interactions on the absorption and emission of poly(3-hexylthiophene). *Phys. Rev. B* 2003, 67, 064203.

131. Clark, J.; Silva, C.; Friend, R. H.; Spano, F. C. Role of Intermolecular Coupling in the Photophysics of Disordered Organic Semiconductors: Aggregate Emission in Regioregular Polythiophene. *Phys. Rev. Lett.* 2007, 98, 206406.

132. Spano, F. C. Modeling disorder in polymer aggregates: The optical spectroscopy of regioregular poly(3-hexylthiophene) thin films. *J. Chem. Phys.* 2005, 122, 234701.

133. Clark, J.; Chang, J.-F.; Spano, F. C.; Friend, R. H.; Silva, C. Determining exciton bandwidth and film microstructure in polythiophene films using linear absorption spectroscopy. *Appl. Phys. Lett.* 2009, 94, 163306.

134. Aryal, M.; Trivedi, K.; Hu, W. Nano-Confinement Induced Chain Alignment in Ordered P3HT Nanostructures Defined by Nanoimprint Lithography. *Acs Nano* 2009, 3, 3085-3090.

135. Prosa, T. J.; Winokur, M. J.; Moulton, J.; Smith, P.; Heeger, A. J. X-ray structural studies of poly(3-alkylthiophenes): an example of an inverse comb. *Macromolecules* 1992, 25, 4364-4372.

136. Jeong, S.; Kwon, Y.; Choi, B.-D.; Ade, H.; Han, Y. S. Improved efficiency of bulk heterojunction poly(3-hexylthiophene):[6,6]-phenyl-C61-butyric acid methyl ester photovoltaic devices using discotic liquid crystal additives. *Appl. Phys. Lett.* 2010, 96, 183305.

137. Holzwarth, U.; Gibson, N. The Scherrer equation versus the 'Debye-Scherrer equation'. *Nat. Nanotechnol.* 2011, 6, 534-534.

138. Ma, L.; Lee, W. H.; Park, Y. D.; Kim, J. S.; Lee, H. S.; Cho, K. High performance polythiophene thin-film transistors doped with very small amounts of an electron acceptor. *Appl. Phys. Lett.* 2008, 92, 063310.

139. Horowitz, G.; Delannoy, P. An analytical model for organic-based thin-film transistors. *J. Appl. Phys.* 1991, 70, 469-475.

140. Ong, B. S.; Wu, Y. L.; Liu, P.; Gardner, S. High-performance semiconducting polythiophenes for organic thin-film transistors. *J. Am. Chem. Soc.* 2004, 126, 3378-3379.

141. Manceau, M.; Rivaton, A.; Gardette, J.-L.; Guillerez, S.; Lemaître, N. The mechanism of photo- and thermooxidation of poly(3-hexylthiophene) (P3HT) reconsidered. *Polym. Degrad. Stab.* 2009, 94, 898-907.

142. Kehrer, L. A.; Winter, S.; Fischer, R.; Melzer, C.; von Seggern, H. Temporal and thermal properties of optically induced instabilities in P3HT field-effect transistors. *Synth. Met.* 2012, 161, 2558-2561.

143. Wang, S.; Tang, J.-C.; Zhao, L.-H.; Png, R.-Q.; Wong, L.-Y.; Chia, P.-J.; Chan, H. S. O.; Ho, P. K.-H.; Chua, L.-L. Solvent effects and multiple aggregate states in

high-mobility organic field-effect transistors based on poly(bithiophene-alt-thienothiophene). *Appl. Phys. Lett.* 2008, 93, 162103.

144. Wang, A.; Kymissis, I.; Bulovic, V.; Akinwande, A. I. Engineering density of semiconductor-dielectric interface states to modulate threshold voltage in OFETs. *IEEE Trans. Electron Devices* 2006, 53, 9-13.

145. Wang, G.; Swensen, J.; Moses, D.; Heeger, A. J. Increased mobility from regioregular poly(3-hexylthiophene) field-effect transistors. *J. Appl. Phys.* 2003, 93, 6137-6141.

146. Horowitz, G. Origin of the "ohmic" current in organic field-effect transistors. *Adv. Mater.* 1996, 8, 177-179.

147. Osikowicz, W.; de Jong, M. P.; Salaneck, W. R. Formation of the Interfacial Dipole at Organic-Organic Interfaces: C60/Polymer Interfaces. *Adv. Mater.* 2007, 19, 4213-4217.

148. Xu, Z.; Chen, L.-M.; Chen, M.-H.; Li, G.; Yang, Y. Energy level alignment of poly(3-hexylthiophene): [6,6]-phenyl C61 butyric acid methyl ester bulk heterojunction. *Appl. Phys. Lett.* 2009, 95, 013301.

149. Chu, P.-H.; Zhang, L.; Colella, N. S.; Fu, B.; Park, J. O.; Srinivasarao, M.; Briseño, A. L.; Reichmanis, E. Enhanced Mobility and Effective Control of Threshold Voltage in P3HT-Based Field-Effect Transistors via Inclusion of Oligothiophenes. *ACS Appl. Mater. Interfaces* 2015, 7, 6652-6660.

150. Brinkmann, M.; Rannou, P. Effect of Molecular Weight on the Structure and Morphology of Oriented Thin Films of Regioregular Poly(3-hexylthiophene) Grown by Directional Epitaxial Solidification. *Adv. Funct. Mater.* 2007, 17, 101-108.

151. Podzorov, V. Conjugated polymers: Long and winding polymeric roads. *Nat. Mater.* 2013, 12, 947-948.

152. Rivnay, J.; Mannsfeld, S. C.; Miller, C. E.; Salleo, A.; Toney, M. F. Quantitative determination of organic semiconductor microstructure from the molecular to device scale. *Chem. Rev.* 2012, 112, 5488-519.

153. Zhang, C.; Chen, P.; Hu, W. Organic Light-Emitting Transistors: Materials, Device Configurations, and Operations. *Small* 2016, 12, 1252–1294.

154. Li, H.; Tee, B. C. K.; Cha, J. J.; Cui, Y.; Chung, J. W.; Lee, S. Y.; Bao, Z. High-Mobility Field-Effect Transistors from Large-Area Solution-Grown Aligned C60 Single Crystals. *J. Am. Chem. Soc.* 2012, 134, 2760-2765.

155. Tseng, H.-R.; Ying, L.; Hsu, B. B. Y.; Perez, L. A.; Takacs, C. J.; Bazan, G. C.; Heeger, A. J. High Mobility Field Effect Transistors Based on Macroscopically Oriented Regioregular Copolymers. *Nano Lett.* 2012, 12, 6353-6357.

156. Wittmann, J. C.; Smith, P. Highly oriented thin films of poly(tetrafluoroethylene) as a substrate for oriented growth of materials. *Nature* 1991, 352, 414-417.

157. Brinkmann, M.; Chandezon, F.; Pansu, R. B.; Julien-Rabant, C. Epitaxial Growth of Highly Oriented Fibers of Semiconducting Polymers with a Shish-Kebab-Like Superstructure. *Adv. Funct. Mater.* 2009, 19, 2759-2766.

158. Yang, Y.; Mielczarek, K.; Aryal, M.; Zakhidov, A.; Hu, W. Effects of nanostructure geometry on nanoimprinted polymer photovoltaics. *Nanoscale* 2014, 6, 7576-7584.

159. Chen, J.-Y.; Wu, H.-C.; Chiu, Y.-C.; Lin, C.-J.; Tung, S.-H.; Chen, W.-C. Electrospun Poly(3-hexylthiophene) Nanofibers with Highly Extended and Oriented Chains Through Secondary Electric Field for High-Performance Field-Effect Transistors. *Adv. Electron. Mater.* 2015, 1, 1400028.

160. O'Connor, B.; Kline, R. J.; Conrad, B. R.; Richter, L. J.; Gundlach, D.; Toney, M. F.; DeLongchamp, D. M. Anisotropic Structure and Charge Transport in Highly Strain-Aligned Regioregular Poly(3-hexylthiophene). *Adv. Funct. Mater.* 2011, 21, 3697-3705.

161. Gustafsson, G.; Inganäs, O.; Stafström, S. Optical anisotropy of neutral and doped poly(3-octylthiophene). *Solid State Commun.* 1990, 76, 203-208.

162. Heil, H.; Finnberg, T.; von Malm, N.; Schmechel, R.; von Seggern, H. The influence of mechanical rubbing on the field-effect mobility in polyhexylthiophene. *J. Appl. Phys.* 2003, 93, 1636-1641.

163. Hartmann, L.; Tremel, K.; Uttiya, S.; Crossland, E.; Ludwigs, S.; Kayunkid, N.; Vergnat, C.; Brinkmann, M. 2D Versus 3D Crystalline Order in Thin Films of Regioregular Poly(3-hexylthiophene) Oriented by Mechanical Rubbing and Epitaxy. *Adv. Funct. Mater.* 2011, 21, 4047-4057.

164. Biniek, L.; Pouget, S.; Djurado, D.; Gonthier, E.; Tremel, K.; Kayunkid, N.; Zaborova, E.; Crespo-Monteiro, N.; Boyron, O.; Leclerc, N.; Ludwigs, S.; Brinkmann, M. High-Temperature Rubbing: A Versatile Method to Align π-Conjugated Polymers without Alignment Substrate. *Macromolecules* 2014, 47, 3871-3879.

165. Hamidi-Sakr, A.; Biniek, L.; Fall, S.; Brinkmann, M. Precise Control of Lamellar Thickness in Highly Oriented Regioregular Poly(3-Hexylthiophene) Thin Films Prepared by High-Temperature Rubbing: Correlations with Optical Properties and Charge Transport. *Adv. Funct. Mater.* 2016, 26, 408-420.

166. Diao, Y.; Shaw, L.; Bao, Z.; Mannsfeld, S. C. B. Morphology control strategies for solution-processed organic semiconductor thin films. *Energy Environ. Sci.* 2014, 7, 2145-2159.

167. Park, S.; Giri, G.; Shaw, L.; Pitner, G.; Ha, J.; Koo, J. H.; Gu, X.; Park, J.; Lee, T. H.; Nam, J. H.; Hong, Y.; Bao, Z. Large-area formation of self-aligned crystalline domains of organic semiconductors on transistor channels using CONNECT. *Proc. Natl. Acad. Sci. U. S. A.* 2015, 112, 5561-5566.

168. Diao, Y.; Tee, B. C. K.; Giri, G.; Xu, J.; Kim, D. H.; Becerril, H. A.; Stoltenberg, R. M.; Lee, T. H.; Xue, G.; Mannsfeld, S. C. B.; Bao, Z. Solution coating of large-area organic semiconductor thin films with aligned single-crystalline domains. *Nat. Mater.* 2013, 12, 665-671.

169. Giri, G.; Park, S.; Vosgueritchian, M.; Shulaker, M. M.; Bao, Z. High-Mobility, Aligned Crystalline Domains of TIPS-Pentacene with Metastable Polymorphs Through Lateral Confinement of Crystal Growth. *Adv. Mater.* 2014, 26, 487-493.

170. Diao, Y.; Zhou, Y.; Kurosawa, T.; Shaw, L.; Wang, C.; Park, S.; Guo, Y.; Reinspach, J. A.; Gu, K.; Gu, X.; Tee, B. C. K.; Pang, C.; Yan, H.; Zhao, D.; Toney, M. F.; Mannsfeld, S. C. B.; Bao, Z. Flow-enhanced solution printing of all-polymer solar cells. *Nat. Commun.* 2015, 6, 1-10.

171. Deng, W.; Zhang, X.; Huang, L.; Xu, X.; Wang, L.; Wang, J.; Shang, Q.; Lee, S.-T.; Jie, J. Aligned Single-Crystalline Perovskite Microwire Arrays for High-Performance Flexible Image Sensors with Long-Term Stability. *Adv. Mater.* 2016, 28, 2201–2208.

172. Ford, M. J.; Wang, M.; Patel, S. N.; Phan, H.; Segalman, R. A.; Nguyen, T.-Q.; Bazan, G. C. High Mobility Organic Field-Effect Transistors from Majority Insulator Blends. *Chem. Mater.* 2016, 28, 1256–1260.

173. Niazi, M. R.; Li, R.; Qiang Li, E.; Kirmani, A. R.; Abdelsamie, M.; Wang, Q.; Pan, W.; Payne, M. M.; Anthony, J. E.; Smilgies, D.-M.; Thoroddsen, S. T.; Giannelis, E. P.; Amassian, A. Solution-printed organic semiconductor blends exhibiting transport properties on par with single crystals. *Nat. Commun.* 2015, 6, 1-10.

174. Soeda, J.; Uemura, T.; Okamoto, T.; Mitsui, C.; Yamagishi, M.; Takeya, J. Inch-Size Solution-Processed Single-Crystalline Films of High-Mobility Organic Semiconductors. *Appl. Phys. Express* 2013, 6, 076503.

175. Giri, G.; Verploegen, E.; Mannsfeld, S. C. B.; Atahan-Evrenk, S.; Kim, D. H.; Lee, S. Y.; Becerril, H. A.; Aspuru-Guzik, A.; Toney, M. F.; Bao, Z. Tuning charge transport in solution-sheared organic semiconductors using lattice strain. *Nature* 2011, 480, 504-508.

176. DeLongchamp, D. M.; Kline, R. J.; Jung, Y.; Germack, D. S.; Lin, E. K.; Moad, A. J.; Richter, L. J.; Toney, M. F.; Heeney, M.; McCulloch, I. Controlling the

Orientation of Terraced Nanoscale “Ribbons” of a Poly(thiophene) Semiconductor. *Acs Nano* 2009, 3, 780-787.

177. Kui, Z.; Hadayat Ullah, K.; Ruipeng, L.; Yisong, S.; Aram, A. Entanglement of Conjugated Polymer Chains Influences Molecular Self-Assembly and Carrier Transport. *Adv. Funct. Mater.* 2013, 23, 6024–6035.

178. Chang, M.; Lee, J.; Chu, P.-H.; Choi, D.; Park, B.; Reichmanis, E. Anisotropic Assembly of Conjugated Polymer Nanocrystallites for Enhanced Charge Transport. *ACS Appl. Mater. Interfaces* 2014, 6, 21541-21549.

179. Shaw, L.; Hayoz, P.; Diao, Y.; Reinspach, J. A.; To, J. W. F.; Toney, M. F.; Weitz, R. T.; Bao, Z. Direct Uniaxial Alignment of a Donor–Acceptor Semiconducting Polymer Using Single-Step Solution Shearing. *ACS Appl. Mater. Interfaces* 2016, 8, 9285-9296.

180. Le Berre, M.; Chen, Y.; Baigl, D. From Convective Assembly to Landau−Levich Deposition of Multilayered Phospholipid Films of Controlled Thickness. *Langmuir* 2009, 25, 2554-2557.

181. Kurik, M. V. Urbach rule. *Phys. Status Solidi A* 1971, 8, 9-45.

182. Pingel, P.; Zen, A.; Abellón, R. D.; Grozema, F. C.; Siebbeles, L. D. A.; Neher, D. Temperature-Resolved Local and Macroscopic Charge Carrier Transport in Thin P3HT Layers. *Adv. Funct. Mater.* 2010, 20, 2286-2295.

183. Dierckx, W.; Oosterbaan, W. D.; Bolsée, J.-C.; Cardinaletti, I.; Maes, W.; Boyen, H.-G.; D’Haen, J.; Nesladek, M.; Manca, J. Organic phototransistors using poly(3-hexylthiophene) nanofibres. *Nanotechnology* 2015, 26, 065201.

184. Persson, N. E.; McBride, M. A.; Grover, M. A.; Reichmanis, E. Automated Analysis of Orientational Order in Images of Fibrillar Materials. *Chem. Mater.* 2017, 29, 3-14.

185. Jordens, S.; Isa, L.; Usov, I.; Mezzenga, R. Non-equilibrium nature of two-dimensional isotropic and nematic coexistence in amyloid fibrils at liquid interfaces. *Nat. Commun.* 2013, 4, 1917.

186. Murphy, J. N.; Harris, K. D.; Buriak, J. M. Automated Defect and Correlation Length Analysis of Block Copolymer Thin Film Nanopatterns. *PLoS One* 2015, 10, e0133088.

187. Bäcklund, T. G.; Sandberg, H. G. O.; Österbacka, R.; Stubb, H.; Torkkeli, M.; Serimaa, R. A Novel Method to Orient Semiconducting Polymer Films. *Adv. Funct. Mater.* 2005, 15, 1095-1099.

188. Lu, G.; Chen, J.; Xu, W.; Li, S.; Yang, X. Aligned Polythiophene and its Blend Film by Direct-Writing for Anisotropic Charge Transport. *Adv. Funct. Mater.* 2014, 24, 4959–4968.

189. Scott, J. I.; Xue, X.; Wang, M.; Kline, R. J.; Hoffman, B. C.; Dougherty, D.; Zhou, C.; Bazan, G.; O'Connor, B. T. Significantly Increasing the Ductility of High Performance Polymer Semiconductors through Polymer Blending. *ACS Appl. Mater. Interfaces* 2016, 8, 14037–14045.

190. Xue, X.; Chandler, G.; Zhang, X.; Kline, R. J.; Fei, Z.; Heeney, M.; Diemer, P. J.; Jurchescu, O. D.; O'Connor, B. T. Oriented Liquid Crystalline Polymer Semiconductor Films with Large Ordered Domains. *ACS Appl. Mater. Interfaces* 2015, 7, 26726-26734.

191. Liu, J.; Haynes, D.; Balliet, C.; Zhang, R.; Kowalewski, T.; McCullough, R. D. Self Encapsulated Poly(3-hexylthiophene)-poly(fluorinated alkyl methacrylate) Rod-Coil Block Copolymers with High Field Effect Mobilities on Bare SiO2. *Adv. Funct. Mater.* 2012, 22, 1024-1032.

192. Perez, L. A.; Zalar, P.; Ying, L.; Schmidt, K.; Toney, M. F.; Nguyen, T.-Q.; Bazan, G. C.; Kramer, E. J. Effect of Backbone Regioregularity on the Structure and Orientation of a Donor–Acceptor Semiconducting Copolymer. *Macromolecules* 2014, 47, 1403-1410.

193. Newbloom, G. M.; Kim, F. S.; Jenekhe, S. A.; Pozzo, D. C. Mesoscale Morphology and Charge Transport in Colloidal Networks of Poly(3-hexylthiophene). *Macromolecules* 2011, 44, 3801-3809.

194. Keum, J. K.; Xiao, K.; Ivanov, I. N.; Hong, K.; Browning, J. F.; Smith, G. S.; Shao, M.; Littrell, K. C.; Rondinone, A. J.; Andrew Payzant, E.; Chen, J.; Hensley, D. K. Solvent quality-induced nucleation and growth of parallelepiped nanorods in dilute poly(3-hexylthiophene) (P3HT) solution and the impact on the crystalline morphology of solution-cast thin film. *Crystengcomm* 2013, 15, 1114-1124.

195. Kleinhenz, N.; Persson, N.; Xue, Z.; Chu, P. H.; Wang, G.; Yuan, Z.; McBride, M. A.; Choi, D.; Grover, M. A.; Reichmanis, E. Ordering of Poly(3-hexylthiophene) in Solutions and Films: Effects of Fiber Length and Grain Boundaries on Anisotropy and Mobility. *Chem. Mater.* 2016, 28, 3905-3913.

196. Chu, P.-H.; Wang, G.; Fu, B.; Choi, D.; Park, J. O.; Srinivasarao, M.; Reichmanis, E. Synergistic Effect of Regioregular and Regiorandom Poly(3-hexylthiophene) Blends for High Performance Flexible Organic Field Effect Transistors. *Adv. Electron. Mater.* 2016, 2, 1500384.

197. Wang, G.; Persson, N.; Chu, P.-H.; Kleinhenz, N.; Fu, B.; Chang, M.; Deb, N.; Mao, Y.; Wang, H.; Grover, M. A.; Reichmanis, E. Microfluidic Crystal Engineering of π-Conjugated Polymers. *Acs Nano* 2015, 9, 8220-8230.

198. Crossland, E. J. W.; Tremel, K.; Fischer, F.; Rahimi, K.; Reiter, G.; Steiner, U.; Ludwigs, S. Anisotropic Charge Transport in Spherulitic Poly(3-hexylthiophene) Films. *Adv. Mater.* 2012, 24, 839-844.

199. Chu, P.-H.; Kleinhenz, N.; Persson, N.; McBride, M.; Hernandez, J. L.; Fu, B.; Zhang, G.; Reichmanis, E. Toward Precision Control of Nanofiber Orientation in Conjugated Polymer Thin Films: Impact on Charge Transport. *Chem Mater* 2016, 28, 9099-9109.

200. Xu, J.; Wang, S.; Wang, G.-J. N.; Zhu, C.; Luo, S.; Jin, L.; Gu, X.; Chen, S.; Feig, V. R.; To, J. W. F.; Rondeau-Gagné, S.; Park, J.; Schroeder, B. C.; Lu, C.; Oh, J. Y.; Wang, Y.; Kim, Y.-H.; Yan, H.; Sinclair, R.; Zhou, D.; Xue, G.; Murmann, B.; Linder, C.; Cai, W.; Tok, J. B.-H.; Chung, J. W.; Bao, Z. Highly stretchable polymer semiconductor films through the nanoconfinement effect. *Science* 2017, 355, 59-64.

201. Savagatrup, S.; Printz, A. D.; O'Connor, T. F.; Zaretski, A. V.; Rodriquez, D.; Sawyer, E. J.; Rajan, K. M.; Acosta, R. I.; Root, S. E.; Lipomi, D. J. Mechanical degradation and stability of organic solar cells: molecular and microstructural determinants. *Energy Environ. Sci.* 2015, 8, 55-80.

202. Reddy, C. M.; Padmanabhan, K. A.; Desiraju, G. R. Structure−Property Correlations in Bending and Brittle Organic Crystals. *Cryst. Growth Des.* 2006, 6, 2720-2731.

203. Awartani, O.; Lemanski, B. I.; Ro, H. W.; Richter, L. J.; DeLongchamp, D. M.; O'Connor, B. T. Correlating Stiffness, Ductility, and Morphology of Polymer:Fullerene Films for Solar Cell Applications. *Adv. Energy Mater.* 2013, 3, 399-406.

204. Wang, Y.; Chen, Z.; Chen, J.; Qu, Y.; Yang, X. Miscibility, Crystallization, and Morphology of the Double-Crystalline Blends of Insulating Polyethylene and Semiconducting Poly(3-Butylthiophene). *J. Macromol. Sci., Part B: Phys.* 2013, 52, 1388-1404.

205. Lu, G.; Tang, H.; Qu, Y.; Li, L.; Yang, X. Enhanced Electrical Conductivity of Highly Crystalline Polythiophene/Insulating-Polymer Composite. *Macromolecules* 2007, 40, 6579-6584.

206. Goffri, S.; Muller, C.; Stingelin-Stutzmann, N.; Breiby, D. W.; Radano, C. P.; Andreasen, J. W.; Thompson, R.; Janssen, R. A. J.; Nielsen, M. M.; Smith, P.; Sirringhaus, H. Multicomponent semiconducting polymer systems with low crystallization-induced percolation threshold. *Nat. Mater.* 2006, 5, 950-956.

207. Arias, A. C.; Endicott, F.; Street, R. A. Surface-Induced Self-Encapsulation of Polymer Thin-Film Transistors. *Adv. Mater.* 2006, 18, 2900-2904.

208. Lee, S.; Jeon, H.; Jang, M.; Baek, K.-Y.; Yang, H. Tunable Solubility Parameter of Poly(3-hexyl thiophene) with Hydrophobic Side-Chains to Achieve Rubbery Conjugated Films. *ACS Appl. Mater. Interfaces* 2015, 7, 1290-1297.

209. Shin, M.; Oh, J. Y.; Byun, K.-E.; Lee, Y.-J.; Kim, B.; Baik, H.-K.; Park, J.-J.; Jeong, U. Polythiophene Nanofibril Bundles Surface-Embedded in Elastomer: A Route to a Highly Stretchable Active Channel Layer. *Advanced Materials* 2015, 27, 1255-1261.

210. Kergoat, L.; Battaglini, N.; Miozzo, L.; Piro, B.; Pham, M.-C.; Yassar, A.; Horowitz, G. Use of poly(3-hexylthiophene)/poly(methyl methacrylate) (P3HT/PMMA) blends to improve the performance of water-gated organic field-effect transistors. *Org. Electron.* 2011, 12, 1253-1257.

211. Noh, Y.-Y.; Sirringhaus, H. Ultra-thin polymer gate dielectrics for top-gate polymer field-effect transistors. *Org. Electron.* 2009, 10, 174-180.

212. Hwang, D. K.; Fuentes-Hernandez, C.; Kim, J.; Potscavage, W. J.; Kim, S.-J.; Kippelen, B. Top-Gate Organic Field-Effect Transistors with High Environmental and Operational Stability. *Adv. Mater.* 2011, 23, 1293-1298.

213. Roberts, M. E.; Queraltó, N.; Mannsfeld, S. C. B.; Reinecke, B. N.; Knoll, W.; Bao, Z. Cross-Linked Polymer Gate Dielectric Films for Low-Voltage Organic Transistors. *Chem. Mater.* 2009, 21, 2292-2299.

214. Oh, J. Y.; Shin, M.; Lee, T. I.; Jang, W. S.; Min, Y.; Myoung, J.-M.; Baik, H. K.; Jeong, U. Self-Seeded Growth of Poly(3-hexylthiophene) (P3HT) Nanofibrils by a Cycle of Cooling and Heating in Solutions. *Macromolecules* 2012, 45, 7504-7513.

215. Oh, J. Y.; Shin, M.; Lee, T. I.; Jang, W. S.; Lee, Y.-J.; Kim, C. S.; Kang, J.-W.; Myoung, J.-M.; Baik, H. K.; Jeong, U. Highly Bendable Large-Area Printed Bulk Heterojunction Film Prepared by the Self-Seeded Growth of Poly(3-hexylthiophene) Nanofibrils. *Macromolecules* 2013, 46, 3534-3543.

216. Park, Y. D.; Cho, J. H.; Kim, D. H.; Jang, Y.; Lee, H. S.; Ihm, K.; Kang, T.-H.; Cho, K. Energy-Level Alignment at Interfaces Between Gold and Poly(3-hexylthiophene) Films with Two Different Molecular Structures. *Electrochem. Solid-State Lett.* 2006, 9, G317-G319.

217. Kwon, S.; Yu, K.; Kweon, K.; Kim, G.; Kim, J.; Kim, H.; Jo, Y.-R.; Kim, B.-J.; Kim, J.; Lee, S. H.; Lee, K. Template-mediated nano-crystallite networks in semiconducting polymers. *Nat. Commun.* 2014, 5.

218. Niedzialek, D.; Lemaur, V.; Dudenko, D.; Shu, J.; Hansen, M. R.; Andreasen, J. W.; Pisula, W.; Müllen, K.; Cornil, J.; Beljonne, D. Probing the Relation Between Charge Transport and Supramolecular Organization Down to Ångström Resolution in a Benzothiadiazole-Cyclopentadithiophene Copolymer. *Adv. Mater.* 2013, 25, 1939-1947.

219. Noriega, R.; Rivnay, J.; Vandewal, K.; Koch, F. P. V.; Stingelin, N.; Smith, P.; Toney, M. F.; Salleo, A. A general relationship between disorder, aggregation and charge transport in conjugated polymers. *Nat. Mater.* 2013, 12, 1038-1044.

220. Lafrance, C. P.; Pezolet, M.; Prud'homme, R. E. Study of the distribution of molecular orientation in highly oriented polyethylene by x-ray diffraction. *Macromolecules* 1991, 24, 4948-4956.

221. Dondero, W. E.; Gorga, R. E. Morphological and mechanical properties of carbon nanotube/polymer composites via melt compounding. *J. Polym. Sci., Part B: Polym. Phys.* 2006, 44, 864-878.

222. Turnbull, D. Kinetics of Heterogeneous Nucleation. *J. Chem. Phys.* 1950, 18, 198-203.

223. Lee, S. S.; Muralidharan, S.; Woll, A. R.; Loth, M. A.; Li, Z.; Anthony, J. E.; Haataja, M.; Loo, Y.-L. Understanding Heterogeneous Nucleation in Binary, Solution-Processed, Organic Semiconductor Thin Films. *Chem. Mater.* 2012, 24, 2920-2928.

224. Joshi, S.; Grigorian, S.; Pietsch, U.; Pingel, P.; Zen, A.; Neher, D.; Scherf, U. Thickness Dependence of the Crystalline Structure and Hole Mobility in Thin Films of Low Molecular Weight Poly(3-hexylthiophene). *Macromolecules* 2008, 41, 6800-6808.

225. Himmelberger, S.; Dacuña, J.; Rivnay, J.; Jimison, L. H.; McCarthy-Ward, T.; Heeney, M.; McCulloch, I.; Toney, M. F.; Salleo, A. Effects of Confinement on Microstructure and Charge Transport in High Performance Semicrystalline Polymer Semiconductors. *Adv. Funct. Mater.* 2013, 23, 2091-2098.

226. Joshi, S.; Grigorian, S.; Pietsch, U. X-ray structural and crystallinity studies of low and high molecular weight poly(3-hexylthiophene). *Phys. Status Solidi A* 2008, 205, 488-496.

227. Hwang, D. K.; Fuentes-Hernandez, C.; Kim, J. B.; Potscavage Jr, W. J.; Kippelen, B. Flexible and stable solution-processed organic field-effect transistors. *Org. Electron.* 2011, 12, 1108-1113.

228. Zhang, F.; Funahashi, M.; Tamaoki, N. Flexible field-effect transistors from a liquid crystalline semiconductor by solution processes. *Org. Electron.* 2010, 11, 363-368.

229. Ahmad, J.; Bazaka, K.; Anderson, L. J.; White, R. D.; Jacob, M. V. Materials and methods for encapsulation of OPV: A review. *Renewable Sustainable Energy Rev.* 2013, 27, 104-117.

230. Schlothauer, J.; Jungwirth, S.; Köhl, M.; Röder, B. Degradation of the encapsulant polymer in outdoor weathered photovoltaic modules: Spatially resolved inspection

of EVA ageing by fluorescence and correlation to electroluminescence. *Sol. Energ. Mater. Sol. Cells* 2012, 102, 75-85.

231. Yang, Y.-Q.; Duan, Y.; Chen, P.; Sun, F.-B.; Duan, Y.-H.; Wang, X.; Yang, D. Realization of Thin Film Encapsulation by Atomic Layer Deposition of Al2O3 at Low Temperature. *J. Phys. Chem. C* 2013, 117, 20308-20312.

232. Wang, X.; Lee, W. H.; Zhang, G.; Wang, X.; Kang, B.; Lu, H.; Qiu, L.; Cho, K. Self-stratified semiconductor/dielectric polymer blends: vertical phase separation for facile fabrication of organic transistors. *J. Mater. Chem. C* 2013, 1, 3989-3998.

233. Song, E.; Kang, B.; Choi, H. H.; Sin, D. H.; Lee, H.; Lee, W. H.; Cho, K. Stretchable and Transparent Organic Semiconducting Thin Film with Conjugated Polymer Nanowires Embedded in an Elastomeric Matrix. *Advanced Electronic Materials* 2016, 2, 1500250.